

Electronic Thesis and Dissertation Repository

---

7-10-2018 11:30 AM

## From Large-scale Molecular Clouds to Filaments and Cores : Unveiling the Role of the Magnetic Fields in Star Formation

Sayantana Auddy, *The University of Western Ontario*

Supervisor: Basu, Shantanu, *The University of Western Ontario*

A thesis submitted in partial fulfillment of the requirements for the Doctor of Philosophy degree  
in Physics

© Sayantan Auddy 2018

Follow this and additional works at: <https://ir.lib.uwo.ca/etd>



Part of the [Numerical Analysis and Scientific Computing Commons](#), and the [Stars, Interstellar Medium and the Galaxy Commons](#)

---

### Recommended Citation

Auddy, Sayantan, "From Large-scale Molecular Clouds to Filaments and Cores : Unveiling the Role of the Magnetic Fields in Star Formation" (2018). *Electronic Thesis and Dissertation Repository*. 5639.  
<https://ir.lib.uwo.ca/etd/5639>

This Dissertation/Thesis is brought to you for free and open access by Scholarship@Western. It has been accepted for inclusion in Electronic Thesis and Dissertation Repository by an authorized administrator of Scholarship@Western. For more information, please contact [wlsadmin@uwo.ca](mailto:wlsadmin@uwo.ca).

# Abstract

I present a comprehensive study of the role of strong magnetic fields in characterizing the structure of molecular clouds. We run three-dimensional turbulent non-ideal magnetohydrodynamic simulations (with ambipolar diffusion) to see the effect of magnetic fields on the evolution of the column density probability distribution function (PDF). Our results indicate a systematic dependence of the column density PDF of molecular clouds on magnetic field strength and turbulence, with observationally distinguishable outcomes between supercritical (gravity dominated) and subcritical (magnetic field dominated) initial conditions. We find that most cases develop a direct power-law PDF, and only the subcritical clouds with turbulence are able to maintain a lognormal body of the PDF but with a power-law tail at high values. I also present a scenario for the formation of oscillatory quasi-equilibrium magnetic ribbons in turbulent subcritical molecular clouds. The synthetic observed relation between apparent width in projection versus observed column density is relatively flat, similar to observations of molecular cloud filaments, and unlike the simple expectation based on a Jeans length argument. Additionally, I develop a core field structure (CFS) method which requires spatially resolved observations of the nonthermal velocity dispersion from the Green Bank Ammonia survey (GAS) of the L1688 region of the Ophiuchus molecular cloud along with the column density map to determine magnetic field strength profile across dense cores. By applying the CFS method we find that for most cores in Ophiuchus the mass-to-flux ratio is decreasing radially outward.

**Keywords:** ISM: clouds - magnetic fields - magnetohydrodynamics (MHD) - stars: formation - turbulence

# Co-Authorship Statement

The three papers that constitute this Thesis were co-authored with various collaborators.

For the projects in Chapter 2 and 3, I am the principal author. I wrote both the papers with inputs from my collaborators. The projects were initiated on ideas originating with Shantanu Basu, who is a co-author. The numerical magnetohydrodynamics MHD code used for both the projects was developed by Takahiro Kudoh, who is a co-author. My task was modifying the numerical code, running simulations, and analyzing the resulting data.

For the final paper in Chapter 4, the idea and the model was proposed by Philip Myers. My task was implementing the model and analyzing the data. I wrote the paper with help from my co-authors. Jorma Harju provided the codes for the  $\text{NH}_3$  line analysis and the column density profiles. Rachel K. Friesen and Jaime E. Pineda, who are the principal investigators of Green Bank Ammonia Survey provided the  $\text{NH}_3$  line data for the project. Shantanu Basu and Philip Myers helped in the interpretation of the results.

*Dedicated to my father Tridip Auddy*

*Arise, awake, and stop not till the goal is reached.*

***Swami Vivekananda***

# Acknowledgements

I would like to take this opportunity to acknowledge all the people who supported me during my time at the University of Western Ontario. Without you all, the completion of this dissertation would not be possible.

First, I want to thank my supervisor Shantanu Basu, who has been my adviser and teacher at every step during the course of my graduate study. My interest in research on star formation is greatly motivated by his deep physical and astronomical insight. I am grateful to you for your support and for helping me in making career and life choices.

To Philip Myers for his advice and scientific ideas. I thank him for giving me the opportunity to work and collaborate with him at CfA, Harvard. To S. R. Valluri for supporting me in various academic matters and for collaborating with me in multiple projects. His valuable teaching has guided me every step of the way.

To the members of my scientific advisory committee, Peter Brown and Stan Metchev for their scientific inputs and also for recommending me to do a predoctoral project at Harvard.

To my friends and colleagues at Western for all the fun and happy hours that we spent together. Sina, Quan-Zhi, Venkat, Deepakshi, Ramit, and Arpan thank you all for the memories we made in the last five years.

To my family, for their continuous love and encouragement. I do not have words to express how grateful I am to my father for his sacrifices and support. All this was possible because of him regularly motivating me whenever I needed it, and for all his love.

To my loving wife Mayuri for being my constant support throughout, even from 11,000 km across the ocean. I could not have done this without you.

# Contents

<b>Certificate of Examination</b>	<b>i</b>
<b>Co-Authorship Statement</b>	<b>ii</b>
<b>Acknowledgements</b>	<b>iii</b>
<b>List of Figures</b>	<b>x</b>
<b>List of Tables</b>	<b>xii</b>
<b>1 Introduction</b>	<b>1</b>
1.1 Preliminaries and overview . . . . .	1
1.2 From clouds to filaments and cores . . . . .	2
1.2.1 “Standard” or strong magnetic field model . . . . .	4
1.2.2 “Turbulent” or weak magnetic field model . . . . .	6
1.2.3 “Turbulent-enhanced ambipolar diffusion” . . . . .	6
1.3 From core to star . . . . .	7
1.4 Evidence of magnetic field . . . . .	7
1.4.1 Direct measurement of magnetic fields . . . . .	8
1.4.2 Indirect measure of magnetic fields . . . . .	10
Column density PDFs . . . . .	11
Filaments or Ribbon . . . . .	12
Transition to velocity coherence . . . . .	12
Density scaling of the magnetic Field . . . . .	13

1.5	Tracing the molecular clouds . . . . .	16
1.5.1	Column density . . . . .	18
1.5.2	Filaments . . . . .	19
1.5.3	Dense cores . . . . .	20
1.6	Chapter preview . . . . .	21
<b>Bibliography</b>		<b>30</b>
<b>2</b>	<b>The Effect of Magnetic Fields on the Column Density PDF</b>	<b>31</b>
2.1	Theory and Numerical Model . . . . .	34
2.1.1	Setup for numerical simulation . . . . .	35
2.1.2	Numerical Parameters . . . . .	37
2.2	Results . . . . .	38
2.2.1	General properties of the supercritical cloud . . . . .	38
	The Column Density PDFs for supercritical clouds . . . . .	40
2.2.2	General properties of the subcritical cloud . . . . .	43
	The column density PDFs for subcritical clouds . . . . .	45
	Effect of Initial Velocity Amplitude . . . . .	49
2.2.3	Comparison of PDFs . . . . .	51
2.3	Discussion . . . . .	51
2.4	Conclusion . . . . .	54
<b>Bibliography</b>		<b>59</b>
<b>3</b>	<b>A Magnetic Ribbon Model for Star-Forming Filaments</b>	<b>60</b>
3.1	Semi-Analytic Model . . . . .	62
3.1.1	Background . . . . .	62
3.1.2	Ribbon Width . . . . .	63
3.1.3	Initial Compression Scale . . . . .	65



Estimate from column density map . . . . .	66
Estimate from star formation timescale . . . . .	66
3.2 Results . . . . .	67
3.2.1 Observed Width . . . . .	67
3.2.2 Observed Column Density . . . . .	68
Case 1 ( $0^\circ \leq \theta \leq \theta_{\text{crit}}$ ) . . . . .	69
Case 2 ( $\theta = \theta_{\text{crit}}$ ) . . . . .	69
Case 3 ( $\theta_{\text{crit}} \leq \theta \leq 90^\circ$ ) . . . . .	70
Case 4 ( $\phi \neq 0^\circ$ ) . . . . .	71
3.2.3 Observed Correlation . . . . .	71
3.3 Conclusion . . . . .	73
<b>Bibliography</b>	<b>76</b>
<b>4 Magnetic Field Structure of Dense Cores using Spectroscopic Methods</b>	<b>77</b>
4.1 Introduction . . . . .	77
4.2 Observations . . . . .	80
4.2.1 Velocity Dispersion . . . . .	80
4.2.2 Column Density and Density Model . . . . .	82
4.3 Model . . . . .	85
4.3.1 Core Field Structure . . . . .	86
4.3.2 Core Properties . . . . .	88
4.3.3 The mass-to-flux ratio . . . . .	92
4.4 Discussion . . . . .	97
4.5 Conclusions . . . . .	99
<b>Bibliography</b>	<b>104</b>
<b>5 Summary</b>	<b>105</b>

<b>Bibliography</b>	<b>109</b>
<b>A Analytic Model of the PDF</b>	<b>110</b>
A.1 Disk Geometry . . . . .	111
<b>B Modified Alfvénic theory</b>	<b>114</b>
B.1 Dispersion relation . . . . .	114
<b>Curriculum Vitae</b>	<b>118</b>

# List of Figures

1.1	The time variation of the density distribution of a collapsing core . . . . .	8
1.2	A schematic diagram of collapsing cloud in the presence of magnetic fields . . .	15
2.1	Logarithmic column density contours for the model B3 . . . . .	39
2.2	Logarithmic column density contours for the model B8 . . . . .	40
2.3	The column density PDF of model B3 . . . . .	41
2.4	The column density PDF of model B8 . . . . .	42
2.5	Logarithmic column density contours for the model V4 . . . . .	44
2.6	Logarithmic column density contours for the model V1 . . . . .	45
2.7	Logarithmic column density contours for the model K1 . . . . .	46
2.8	The time evolution of the column density PDF of the model V4 . . . . .	47
2.9	The column density PDF of model V4 . . . . .	48
2.10	The column density PDF of model K1 . . . . .	49
2.11	The column density PDF of model V1 . . . . .	50
2.12	The column density PDFs of simulated models . . . . .	52
3.1	The formation of a magnetic ribbon . . . . .	65
3.2	Different orientations of the magnetic ribbon . . . . .	70
3.3	Apparent ribbon width $L_{\text{obs}}$ versus observed column density $N_{\text{obs}}$ . . . . .	72
4.1	Velocity dispersion profiles of the H-MM1 . . . . .	81
4.2	Velocity dispersion profiles of some selected cores in Ophiuchus . . . . .	82
4.3	Sub-millimeter intensities and density profiles . . . . .	83

4.4 The plane-of-sky magnetic field profile of H-MM1 . . . . . 87

4.5 The plane-of-sky magnetic field profile of six different cores . . . . . 88

4.6 The magnetic field fluctuation . . . . . 90

4.7 The magnetic field fluctuation  $\delta B$  across the six cores . . . . . 91

4.8 The different energy estimates of H-MM1 . . . . . 92

4.9 The normalized mass-to-flux ratio of H-MM1 . . . . . 94

4.10 The normalized mass-to-flux ratio of six different cores . . . . . 95

4.11 An illustration of the magnetic flux contours in H-MM1 . . . . . 96

# List of Tables

2.1	$\beta_0$ is the initial ratio of thermal to magnetic pressure . . . . .	37
2.2	Fit parameters for the MLP distribution to the column density PDF . . . . .	51
4.1	The Plummer fit parameters are $n_0, r_0$ . . . . .	84

# Chapter 1

## Introduction

### 1.1 Preliminaries and overview

The process of star formation is of fundamental significance as it acts as a link between galaxy evolution, planet formation, and astrobiology (Chyba & Hand, 2005; Gillon, 2014; Lingam & Loeb, 2018; Krumholz et al., 2018). Thus the question “how stars are formed?” is of primary importance in the contemporary astrophysics community. Many leading scientists have addressed this key astrophysical problem from various perspectives (Mouschovias & Spitzer (1976); Larson (1981); Shu et al. (1987); Mac Low & Klessen (2004), also see recent reviews by Basu (2017); Basu & Auddy (2017)). In spite of significant progress, complete theoretical and observational understanding of their formation remains elusive. The theory of star formation is not definite owing to the complexities of the physical processes involved. The dynamics of the star-forming molecular clouds in the interstellar medium are complicated by the phenomena like magnetic fields, supersonic turbulence (Mouschovias & Spitzer, 1976; Shu, 1977; McKee & Ostriker, 2007; Lazarian & Hoang, 2007) and stellar feedback, via winds and supernova (Hayward & Hopkins, 2017). In the simplest terms, stars are formed when low-density molecular clouds fragment into locally collapsing objects when the force due to gravity exceeds all other opposing forces. The fragmentation of molecular clouds is a complex

phenomenon driven by the interplay of gravity, magnetic fields, and turbulence (Basu, 2017).

In this thesis, we investigate the processes likely responsible for the formation of stars in molecular clouds. We provide a comprehensive study of the fragmentation of large-scale molecular clouds into filaments and cores, which eventually collapse under gravity to form stars. We use theoretical models, magnetohydrodynamic (MHD) simulations, and observational data to bridge some of the existing gaps in our current understanding of the role of the magnetic field in star formation. We find indirect signatures of imprints of the magnetic fields on the observable structures like column density probability distribution function (PDF), filaments, and dense cores. Finally, we quantify its role in formation and evolution of interstellar clouds and in controlling the rate of star formation.

## 1.2 From clouds to filaments and cores

Molecular clouds are the centers for current day star formation. They are cold,  $T \sim 10$  K, and massive objects with mass few  $\times 10^9 M_\odot$  ( $M_\odot = 1.99 \times 10^{33}$  g is a single solar mass). Molecular clouds can fragment into locally collapsing objects when they become gravitationally unstable i.e., when the gravitational force overwhelms the local support mechanism (also known as Jeans-unstable (Jeans, 1929)). If gravity alone was relevant the overall expected Galactic star formation rate (SFR) would be  $\sim 500 M_\odot \text{ yr}^{-1}$  i.e., the total mass of the molecular clouds ( $\sim 2 \times 10^9 M_\odot$ ) divided by their free-fall time ( $4 \times 10^6$  yr for a typical particle number density of  $100 \text{ H}_2$  molecules per  $\text{cm}^{-3}$ ). Such an uninhibited gravitational collapse in a free-fall time of  $t_{\text{ff}} \propto 1/\sqrt{G\rho}$  (Jeans, 1902) would cause the Galaxy to be depleted of gas long ago. On the contrary, the observed SFR in the Milky Way is only  $\sim 1 - 3 M_\odot \text{ yr}^{-1}$  (McKee & Williams, 1997; Robitaille & Whitney, 2010; Chomiuk & Povich, 2011). We also observe large amounts of gas in the interstellar medium, particularly the dense gas of molecular clouds called the Giant Molecular Clouds (GMCs), each containing typically  $\approx 10^6 M_\odot$ . Furthermore, it has been well established that star formation is an inefficient process with only a few percent of

the total gas actually forming stars (Myers et al., 1986; Evans et al., 2009; Lada et al., 2010). This naturally raises the question: what additional forces can counter gravity? Observationally the increased spectral line widths, which are broader than their thermal counterpart (see review by Zuckerman & Palmer (1974)), indicate that there must be some support besides the thermal pressure.

Historically, it was established that the magnetic force could provide that additional non-thermal support that can prevent fragmentation and rapid star formation (Mestel & Spitzer, 1956; Mestel, 1965). Observational results do indicate that magnetic fields are omnipresent through our Galaxy and are mostly oriented along the Galactic spiral arms (see, e.g., Han & Zhang (2007)). The presence of the magnetic field in the interstellar medium (ISM) can be attributed to the tiny drift in velocity between electrons ( $v_e$ ) and positively charged ions ( $v_i$ ). For example, a magnetic field of  $B \approx 3 \mu\text{G}$  can be maintained by an very small differential velocity drift  $|v_i - v_e| = cB/(n_e e 4\pi L) \sim 10^{-3} \text{cm s}^{-1}$ , where  $n_e \sim 10^{-2} \text{cm}^{-3}$  is the number density,  $L \sim 10^{19} \text{cm}$  is the cloud size,  $e$  and  $c$  are the electron charge and speed of light respectively. Thus naturally magnetic field will have a substantial impact on the dynamics of the molecular cloud particularly in the process of star formation.

It is intuitive to model ISM and star forming molecular clouds, which consist of charged fluids in presence of magnetic fields, using MHD processes to explain complex astrophysical phenomenon. The MHD model is based on the ‘fluid approximation’ approach, where the ISM cloud is treated as a continuum medium. The collisional mean free path  $l \sim (n\sigma)^{-1}$  in interstellar space for neutral atoms and molecules, of typical density  $n \sim 10^{-4}$  and elastic scattering cross section  $\sigma \sim 10^{-15} \text{cm}^2$ , equals  $\sim 10^{11} \text{cm}$ . Although, this represent a large distance, molecular clouds span much greater, typically  $L = 10 \text{pc}$  ( $10^{19} \text{cm}$ ) or  $0.1 \text{pc}$  ( $10^{17} \text{cm}$ ) in cores. Thus such diffuse gas clouds (where  $l \ll L$ ) can effectively be treated as fluids. Furthermore, we can impose the MHD approximations that modify the equations of Maxwell’s theory of electrodynamics to a more tractable form (see section 2.1.1 for details). For slow time variations relevant for astrophysical fluids, we drop the displacement current term in Maxwell’s equation



as it corresponds to a high-frequency phenomenon. Thus the local electric currents (due to the small drift velocity between the ions and electrons) effectively constitute the only source for the magnetic fields. However, for astrophysically realistic circumstances we neglect any spatial separation between ions and electrons and consider a single-component MHD fluid. The fluid is treated as neutral with the assumption that collisions occur frequently enough to mechanically couple the three constituent of the gas (namely ions, electrons and neutrals). However, in Chapter 2 we consider the additional non-ideal MHD effect of a relative drift between neutrals and charged particles (known as ambipolar diffusion in the astrophysical community).

The theory of star formation has developed on the foundation laid by the MHD theories and fluid dynamics. Over the past few decades researchers have considered various modifications to the MHD models (including non-ideal effects and turbulence) to better interpret and understand observational results. In the subsequent section, we discuss the three major classes of contemporary star formation theories that differ on the role of magnetic fields and turbulence (also see the review by Crutcher (2012)).

### 1.2.1 “Standard” or strong magnetic field model

The “standard” paradigm is the strong field theory, where magnetic fields and ambipolar diffusion (neutral-ion slip) govern the star formation process. The ratio of mass to magnetic flux ( $M/\Phi$ ) gives the relative strength of gravity and the magnetic field in a molecular cloud. Mestel & Spitzer (1956); Mouschovias & Spitzer (1976); Strittmatter (1966); Tomisaka et al. (1988) showed that there exist a critical mass-to-flux ratio  $(M/\Phi)_{\text{crit}}$ , such that for  $M/\Phi < (M/\Phi)_{\text{crit}}$  the cloud is subcritical and cannot collapse as long as flux freezing prevails. However, supercritical clouds with  $M/\Phi > (M/\Phi)_{\text{crit}}$  are unstable and prone to collapse. In the standard picture clouds are initially subcritical (as observed by Heiles & Troland (2005)) with mass-to-flux ratio  $M/\Phi < (M/\Phi)_{\text{crit}} = (2\pi G^{1/2})^{-1}$  (Nakano & Nakamura, 1978). They form a layer that is flattened along the direction of the background magnetic field and are stable against fragmentation. The magnetic pressure is sufficiently strong to halt the gravitational collapse.

The magnetic force is only felt by the ionized gas and dust. However, for sufficiently high ionization fraction, the neutrals and the charged species collide frequently enough that the field lines are dragged along with the neutrals. The neutrals feel the influence of the magnetic field through collisions, even though the Lorentz force does not affect them directly. Eventually, the neutrals slip past the ions (which are comoving with the magnetic field) and contract gravitationally on an ambipolar diffusion time scale (Langer, 1978; Ciolek & Basu, 2006; Mouschovias et al., 2011). This phenomenon is called gravitationally-driven ambipolar diffusion (Mouschovias, 1978; Lizano & Shu, 1989).

The typical observed ionization fraction in molecular clouds (primarily cosmic ray ionization) is as low as  $10^{-7} (n_n/10^4 \text{ cm}^{-3})^{-1/2}$  (Elmegreen, 1979), where  $n_n$  is the neutral number density. Such low ionization still provides enough coupling between the charged species and the neutrals. This is because of the high-polarizability of the neutrals, particularly  $\text{H}_2$  molecules. The effective collision cross section is much larger,  $\approx 10^2$  times the geometric cross-section (Osterbrock, 1961). In case the coupling is relatively weak, the neutrals are only moderately impeded by collisions with ions. They gradually diffuse through the field lines and make the core supercritical as the mass increases. The supercritical core then collapses almost on a free-fall timescale to form a star. This phenomenon is well studied in two dimensional simulations of ambipolar-diffusion-driven fragmentation of infinitesimally thin sheet threaded by an initially perpendicular magnetic field (Indebetouw & Zweibel, 2000; Basu & Ciolek, 2004; Basu et al., 2009b). However, one of the criticisms of the strong field model is the core formation time which is typically few dynamical time  $t_{\text{dyn}} (\approx 10 \text{ Myr})$ . This is much longer than the ages of pre-main-sequence stars within clouds ( $\approx 1-3 \text{ Myr}$ ) (Hartmann, 2001). Recently, alternative theories have emerged that include turbulence as an initial condition. In section 1.2.3 we discuss turbulence accelerated ambipolar diffusion that essentially speeds up the core formation time.

### 1.2.2 “Turbulent” or weak magnetic field model

The other model is that molecular clouds are short-lived and star formation is regulated by supersonic random motions (Elmegreen, 2000; Palla & Stahler, 2002; Hartmann, 2001; Padoan & Nordlund, 2002; Federrath & Klessen, 2012). Such large-scale turbulent motions are ubiquitous in the ISM as reviewed by Elmegreen & Scalo (2004). Supersonic turbulence decays in  $\lesssim 1 t_{\text{dyn}}$  (Mac Low et al., 1998). The proponents of the turbulence-regulated star formation theory (for example Hartmann (2001)) believe that molecular clouds are formed at the intersection of turbulent supersonic flow. In this picture the role of turbulence is dual. The turbulent compressions induce local fragmentation producing cores and filaments which eventually form stars. But on a large-scale, it provides global support where the turbulent energy stabilizes the cloud. Commonly predicted drivers of the turbulent energy input are large-scale flows in the ISM (Hartmann, 2001), supernovae (Klessen et al., 2005), and stellar feedback (Hayward & Hopkins, 2017). One of the major criticisms of this turbulence driven star formation theory is the constant need to drive turbulent motions into the system (e.g., simulations by Padoan & Nordlund (2002); Mac Low & Klessen (2004), and more recent ones by Federrath & Klessen (2012); Federrath (2016) and reference therein). Such continuous input of kinetic energy is often unphysical.

### 1.2.3 “Turbulent-enhanced ambipolar diffusion”

An alternative scenario is the “*turbulence-enhanced ambipolar diffusion*” model where the turbulent initial compressions cause the ambipolar diffusion to proceed at an increased rate. Li & Nakamura (2004) and Nakamura & Li (2005) adopted the thin-disk approximation and found that initial supersonic motions can cause rapid local ambipolar diffusion in a subcritical cloud. The core formation time is significantly accelerated as confirmed by Basu et al. (2009a). Detailed three-dimensional simulations by Kudoh & Basu (2008); Nakamura & Li (2008); Kudoh & Basu (2011) show that molecular clouds fragment due to the combined effect of turbulence, gravity, and magnetic fields. However, gravity is still the primary driver for the fragmentation

process. Fragmentation can ensue either through direct gravitational instability on the dynamical timescale for clouds with a supercritical mass-to-flux ratio or due to gravitationally-driven ambipolar diffusion if the cloud is subcritical. The MHD simulations show that a large-scale turbulent flow sweeps up the interstellar medium and compresses the gas into filaments and shocks. The magnetic field mainly provides a global support against the collapse until gravitationally driven ambipolar diffusion leads to a runaway collapse of the densest regions of the cloud.

### 1.3 From core to star

Once the supercritical cores are formed they are prone to collapse under its gravity. The framework for the current theory of the formation of stars due to dynamic collapse of a core under its self-gravity was motivated by the early work of Hayashi & Nakano (1965) and review by Hayashi (1966). Larson (1969) showed that star undergoes a nonhomologous contraction towards a centrally condensed configuration. This runaway collapse results in the formation of a hydrostatic protostellar core. The modern standard picture of isolated star formation was initiated by Shu and collaborators (Shu, 1977; Shu et al., 1987). Typically, collapse is self-similar with an initial singular isothermal sphere with a density  $\rho \sim 1/r^2$ . As the free fall time  $t_{\text{ff}} \propto 1/\sqrt{G\rho}$ , the innermost densest part collapses faster while the outer envelope is still nearly at rest (see Figure 1.1). Once a central point mass (the star) is formed, further infall is initiated from “inside-out” by an expansion wave that propagates outward at the sound speed. The central object accretes at a constant rate given as  $\dot{M} \sim c_s^3/G$  ( $c_s$  is the isothermal sound speed of the core).

### 1.4 Evidence of magnetic field

In order to confirm or rule out the applicability of any of the above theories for the early phases of star formation, it is imperative to test the theories against direct and indirect observations.

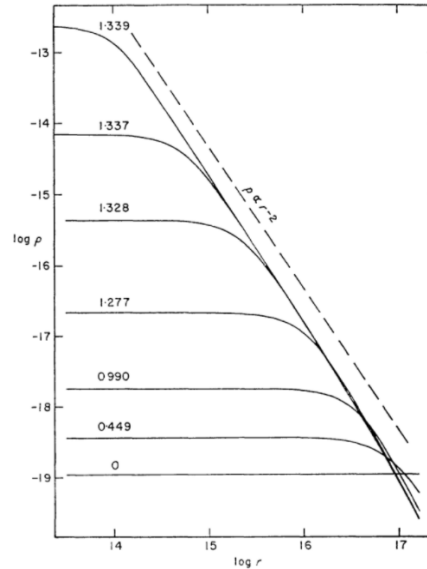


Figure 1.1: The time variation of the density distribution of a collapsing core using numerical simulation (Larson, 1969). The central density peak gradually grows during the initial isothermal phase of collapse. The density distribution approaches  $\rho \propto r^{-2}$  outside the central flat region. Each curve is labeled with time in the units of  $10^{13}$ s.

What role the magnetic field plays in regulating star formation has been debated for decades. In spite of substantial progress both theoretically and observationally, the debate still persists whether magnetic support (Mouschovias, 1991) or turbulent motions (Padoan & Nordlund, 1999) dominate, or if both processes are crucial in regulating star formation in molecular clouds (Nakamura & Li, 2008). The best way to converge to a unique answer to this long-standing controversy is to observe magnetic fields or their indirect tracers and compare with theoretical predictions. In this thesis, we primarily focus on identifying structural evidences that are natural imprints of a (strong) magnetic field. In the following subsection, we discuss some of the observational challenges in directly measuring the magnetic field. We then introduce some alternative and indirect ways to gauge the influence of magnetic fields in the formation of stars.

### 1.4.1 Direct measurement of magnetic fields

The progress in measuring field strength is rather slow due to the various limitations of the existing observational techniques (Crutcher, 2012). The Zeeman effect is the only direct way

of measuring the line-of-sight component of the field strength (Crutcher et al., 2010). It is the splitting of a spectral line into several components in the presence of a static magnetic field. However, the Zeeman detection is often difficult as the spectral-line width  $\Delta\nu$  is much broader than the Zeeman splitting  $\Delta\nu_Z$ . Zeeman observations are only suited for the line-of-sight component  $B_{\text{LOS}}$  of  $B$ . The Zeeman effect gives a lower limit to the total magnetic field strength as it measures only one component of the magnetic vector  $B$ . Additionally Zeeman detections are extremely rare and challenging owing to the limitations in observational sensitivity and resolution (Heiles & Troland, 2005; Crutcher et al., 2010). The recent compilation of magnetic field strengths using the Zeeman effect was done by Crutcher et al. (2010). Four additional surveys (Crutcher, 1999; Heiles & Troland, 2004; Falgarone et al., 2008; Troland & Crutcher, 2008) were used for the volume density information. Crutcher et al. (2010) used Bayesian statistical techniques to fit a model to the magnetic field strengths of the observed clouds. However, there are considerable debates regarding their conclusion that magnetic cores undergo isotropic collapse. We discuss the possible inconsistencies in detail in Section 1.4.2.

Sensitive observations of dust polarization often provide a good characterization of the plane-of-sky magnetic field. The dust grains tends to align with their shorter axis parallel to the magnetic field (Andersson et al., 2015). Thus the emitted or absorbed light is in general perpendicular to the magnetic field due to various alignment mechanisms (for example radiative torque (Draine & Weingartner, 1996, 1997; Cho & Lazarian, 2005; Lazarian & Hoang, 2007)). Polarization observations from dust thermal emission or extinction of background starlight from the dust provide unique ways to probe the magnetic field morphology in the ISM, including collapsing cores in molecular clouds. Several high resolution hourglass patterns (which are consistent with gravitational contraction with at least approximate flux-freezing) are observed in dense cores (e.g., NGC1333 (Girart et al., 2006); L1157-mm (Stephens et al., 2013); G240.31+0.06 (Qiu et al., 2014); FeSt 1-457 (Kandori et al., 2017); and B335 (Maury et al., 2018)). Dust polarization measurements in infrared and submillimeter can also be used to estimate the mean magnetic field strength in the plane of the sky using the Chandrasekhar-

Fermi (CF) (Davis & Greenstein, 1951; Chandrasekhar & Fermi, 1953; Kandori et al., 2017) method. This method works on the assumption that the non-thermal motions are Alfvénic with equipartition between the magnetic and the turbulent energy. The turbulent motion perturbs the magnetic field which shows up as an irregular scatter in the polarization position angles with respect to the mean background field orientation. However, the CF estimates are often restricted due to limitations in the resolution and the number of independent observed polarization vectors. Furthermore, dust polarization can be weak in the centers of dense cores where the dust grains are well shielded from the radiative torques necessary to move the grains into alignment with the magnetic field (e.g., see Lazarian & Hoang (2007)). Other methods of field strength estimation like Faraday rotation (Wolleben & Reich, 2004) are quite rare in star-forming molecular clouds due to low fractional ionization.

### **1.4.2 Indirect measure of magnetic fields**

It is evident that direct detection of the magnetic field using the above techniques is difficult and highly uncertain. There are discernible differences of opinion on the role of the magnetic field in the astrophysical community largely due to lack of observational constraints. It is generally established that magnetic fields tend to preserve their order globally from the inter-cloud medium ( $\sim 100$  parsec) to cloud cores (sub-parsec) (see the review by Li et al. (2014) and references therein). Some theories suggest that magnetic fields lose their orientation at the scales of molecular clouds (Dobbs, 2008) due to turbulence and cloud rotation. On the other hand, it is possible that gas is channeled along the field lines (e.g., Shetty & Ostriker (2006)) as they fragment. The presence of ambient magnetic fields can directly influence the structural properties and the fragmentation process of molecular clouds. Thus it is imperative that we look for alternative methods that can serve as indirect detection of the magnetic field in molecular clouds. We introduce structural evidence that can essentially link the theoretical and simulation prediction of the role of magnetic fields, turbulence, and gravity to the observed structure in star-forming molecular clouds.

### Column density PDFs

The column density probability distribution function (PDF) is an interesting and widely studied structural property of molecular clouds. It can connect the ambient magnetic field strength to the structural properties of the molecular clouds. In recent years, there has been developing interest among both theorists and observers to study column density PDFs. It is considerably easy to measure column density of molecular clouds from, e.g., dust extinction and/or emission observations (Kainulainen et al., 2009; Alves et al., 2014) or simulations (Collins et al., 2012; Federrath & Klessen, 2013) (also see Section 1.5.1 for details). Early theoretical works including numerical simulations (Vázquez-Semadeni, 1994; Passot & Vázquez-Semadeni, 1998) showed that PDFs are lognormal for turbulent non-self-gravitating purely hydrodynamic isothermal gas. However, the inclusion of self-gravity (Ballesteros-Paredes et al., 2011; Ward et al., 2014) showed growing evidence of power-law at high density. Observations (Kainulainen et al., 2009; Pokhrel et al., 2016) also showed that the column density PDFs are lognormal with an additional power-law at the high column density. Alternatively, (Lombardi et al., 2015; Alves et al., 2017) showed that PDFs are best represented as a power-law profile with a larger dynamic range and a peak set by the cloud boundary. Thus the key question is whether clouds with a strong magnetic field show any distinguishable features in the column density PDFs in comparison to clouds with weak magnetic fields. Some theories (for example by Federrath & Klessen (2013)) claim that although the magnetic field provides additional support against turbulent compression, it does not affect the power-law slope of the PDFs. Furthermore, it is also debatable if the width of the lognormal PDF is set by supersonic turbulence (Collins et al., 2012) alone or if the magnetic field strength is also responsible (Molina et al., 2012). In Auddy et al. (2018) (chapter 2 of this thesis), we have presented a systematic study (also see the review by Basu & Auddy (2017)) of the evolution of the column density PDF for different initial conditions. We do see that a strong magnetic field can substantially influence the column density PDF with a distinguishable difference in its power-law slope.



## **Filaments or Ribbon**

Star formation simulations of a strongly magnetic medium with turbulent initial conditions (Nakamura & Li, 2005; Basu et al., 2009a; Kudoh & Basu, 2011) show that molecular clouds fragment into ribbon-like structures in a layer that is flattened along the field direction. These triaxial objects are called “Magnetic Ribbons” and are studied theoretically by Tomisaka (2014) and Hanawa & Tomisaka (2015). The ribbon geometry is consistent with the observation of magnetic fields aligned perpendicular to the filaments (Palmeirim et al., 2013; Planck Collaboration et al., 2016). Another popular idea is that filaments are essentially isothermal cylinders (André et al., 2010), which are either in equilibrium or unstable to collapse depending on their mass per unit length. They could be formed as a result of compression due to shocks primarily due to stellar feedback, supernovae, or turbulence (e.g., Hartmann (2001); Arzoumanian et al. (2011)). This model implies dynamically weak magnetic fields that are embedded along the long axis of the cylinder. Thus an interesting implication is that the global structure of the magnetic field is connected with the morphology of the cloud (filaments or ribbon), particularly if the strength of the ambient magnetic field is regulating the initial condensation of the gas. Specifically, the measured relation between the apparent width and the observed column density could indicate if magnetic ribbons are a more natural configuration. Recent observations (Arzoumanian et al., 2011) using the Herschel Space Observatory indicate that the relationship between the filament width and column density is nearly flat, unlike the expectation based on a Jeans length argument. In Auddy et al. (2016) (Chapter 3 of this thesis), we present a quasi-equilibrium ribbon model that is consistent with a strong magnetic field with supersonic turbulence model.

## **Transition to velocity coherence**

Recent observations imply a transition from a non-thermal line width in low-density molecular clouds to a nearly thermal line width within dense cores. This is termed as a transition to velocity coherence (Goodman et al., 1998; Pineda et al., 2010). An important question is

whether a transition from magnetic support of low-density regions to gravitational collapse of dense regions is physically related to the transition to coherence. Observations using the  $\text{NH}_3$  emission maps from the Green Bank Ammonia Survey (GAS) has revealed gas kinematics information with unprecedented sensitivity. In Chapter 4 of this thesis, we introduce a new method of estimating the amplitude of magnetic field fluctuations using the recent detailed maps from the GAS of the nonthermal line width profiles across a core. One of the outcomes of the model is the measure of the mass-to-flux ratio profile across the dense cores in Ophiuchus. This can potentially serve as a test of gravitationally-driven ambipolar diffusion theory, where ambipolar diffusion leads to the formation of supercritical cores within a subcritical envelope.

### **Density scaling of the magnetic Field**

For contracting interstellar clouds and fragments (particularly cores), the relation between magnetic-field strength ( $B$ ) and gas density ( $\rho$ ) is of primary importance. It is central in observationally quantifying the dynamical importance of magnetic fields in the evolution of molecular clouds and star formation. Due to a high electrical conductivity of the interstellar gas (Mestel & Spitzer, 1956) the magnetic field is frozen in the matter and can prevent fragmentation and spherical collapse. There are two testable predictions for the  $B - \rho$  relation for a gravitating magnetic cloud. Mestel (1965) argued that for a magnetic cloud collapsing spherically and isotropically, the scaling between the field strength  $B$  and the density is  $B \propto \rho^{2/3}$ . This is true for quasi-spherical collapse where both the mass  $M$  and the flux  $\Phi$  is conserved i.e.,  $M \propto \rho R^3 = \text{const}$ ,  $\Phi_B \propto BR^2 = \text{const}$ . However, a more self-consistent theory of non-homologous contraction and equilibria of a self-gravitating isothermal interstellar cloud bounded within a hot and tenuous medium was given by Mouschovias (1976a,b). He argued that the plasma  $\beta = 8\pi\rho c_s^2/B^2$ , i.e., the ratio of gas to magnetic pressure, remains constant during contraction. Thus for an isothermal contraction this yields  $B \propto \rho^{1/2}$ . Naturally, the cloud flattens due to self-gravity along the field lines and settles into a vertical hydrostatic equilibrium to form a disk. The extent of flattening depends on the strength of the magnetic field,

gravitational force, and intercloud pressure. Furthermore, for such a nonhomologous collapse it is straightforward to show that conservation of mass  $M \propto \Sigma R^2 = \text{const}$  (where self gravity imposes  $\Sigma \propto \rho^{1/2}$ ) and flux  $\Phi$  yield  $B \propto \rho^{1/2}$ . Numerical simulations (Fiedler & Mouschovias, 1992, 1993; Ciolek & Mouschovias, 1994) of cores forming due to gravitationally-driven ambipolar diffusion predict  $\kappa \leq 1/2$ . Such simulations invoke a dynamically important magnetic field that leads to flattening along the magnetic field direction, and subsequent evolution primarily perpendicular to the field.

Crutcher (1999) compiled magnetic field strengths and number density of a large sample of clouds. He found the best fit value for  $\kappa$  to be 0.47, in rough agreement with the theoretical prediction. Recent observations of massive star-forming regions NGC 6334 by Li et al. (2015a) estimate  $\kappa = 0.41$ . However, Crutcher et al. (2010) revised the  $B$  and  $\rho$  relation for a larger sample of both low-density H1 and high-density molecular clouds. They used a Bayesian statistical analysis to analyze the observed probability density function (PDF) and the line-of-sight component of the magnetic field from Zeeman surveys of H1, OH, and CN spectral lines. Figure 1 in Crutcher et al. (2010) shows the Zeeman measurements of the line-of-sight component of  $B$  and their  $1\sigma$  uncertainty plotted against the n(H1) and molecular clouds n(H<sub>2</sub>). The plot consists of a flat part at low-density, a power-law scaling  $B \propto \rho^{2/3}$  at high density, and a joining point density  $\rho_0$ . According to the Crutcher's interpretation, the flat region represents the initial accumulation of the gas along field lines resulting in an increase in density while  $B$  remains unchanged, i.e.,  $B \propto \rho^0$ . Furthermore, the gas becomes self-gravitating at  $\rho_0$ , leading to a more isotropic spherical contraction with the scaling of the flux frozen field as  $B \propto \rho^{2/3}$ . The magnetic field is therefore considered too weak to affect the morphology of the collapse.

Li et al. (2015b) performed two three-dimensional turbulent ideal MHD simulations to confirm the  $B - \rho$  scaling relation from the Crutcher observation. Both the simulations with weak and strong magnetic field were driven with Mach 10 turbulence. Their results indicate that values of  $\kappa$  are  $0.70 \pm 0.06$  and  $0.57 \pm 0.05$  for the strong and weak field models, respectively. The authors suggest that the simulated results agree with the observed value of  $\kappa$  within the errors.

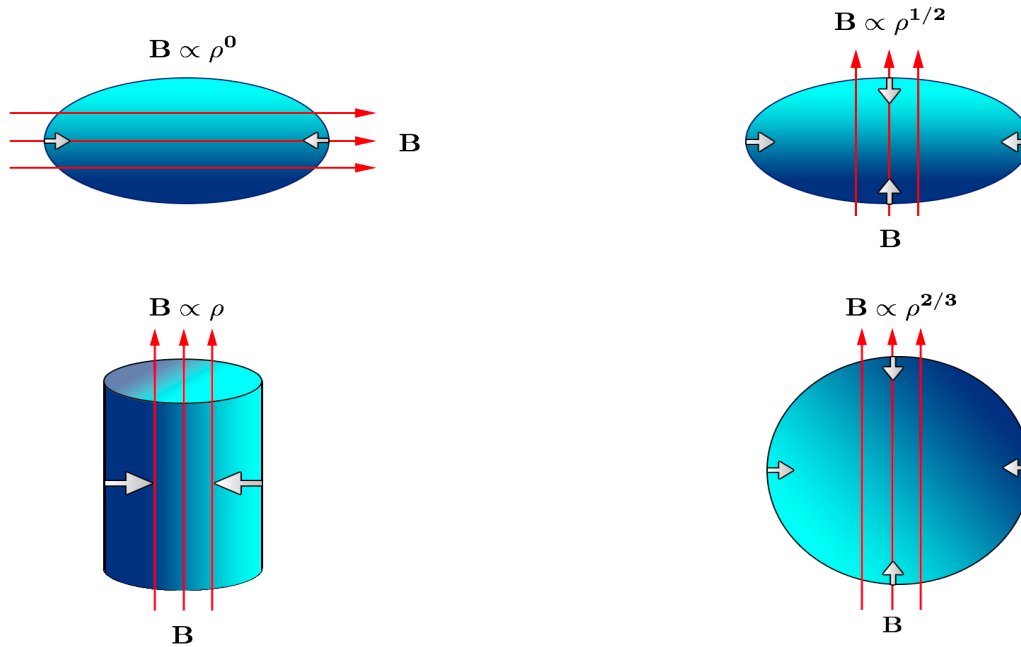


Figure 1.2: A schematic diagram (similar to Figure 1 in Tritsis et al. (2015)) representing different geometries of a collapsing cloud in the presence of magnetic fields. The red arrow represents the direction of the magnetic field and the white arrows the direction of contraction.

However, it is counter-intuitive that power-law index  $\kappa$  is significantly lower for the weak field model. The more expected result is that for the weak magnetic field the density dependence must be closer to  $\kappa = 2/3$  as predicted by the weak field spherical collapse theory (Mestel, 1965, 1966). The morphology of their simulation (see Figure 10 in Li et al. (2015b)) results show that the density structures are very distorted and nothing like spheres. The emergence of the values of  $\kappa$  in both the simulations may be entirely due to a time (ensemble) average of epochs of turbulent compression. In situations where the magnetic field is weak compared to the turbulent driving (like in the above simulation) the gas can be compressed both laterally ( $x - y$ ) and along the field lines ( $z$ ). For the latter  $\kappa = 0$ , as the change in  $B$  is independent of  $\rho$ . For lateral compression,  $\kappa = 1$  due to flux freezing. The three possibilities yield  $\kappa = 0$ , or 1,1 for an average value of  $2/3$ . An illustration showing of all the possible geometries for core collapse are shown in Figure 1.2.

Ideal MHD simulations by Collins et al. (2011, 2012) of star-forming cores with weak mean field in a turbulent environment resulted in a scaling relation  $B \propto \rho^{0.4-0.5}$ . Subsequent

simulations using AREPO code ((Mocz et al., 2017)) with highly turbulent and magnetized initial conditions showed that core collapse can be either  $B \propto \rho^{2/3}$  for the turbulence scenario and  $B \propto \rho^{1/2}$  in the case of moderately strong large-scale magnetic fields.

Alternately, Trites et al. (2015) emphasized the fact that  $B \propto \rho^{2/3}$  can only be realized under isotropic contraction and is unique for a spherical core. On reanalysis of the same data (as in Crutcher et al. (2010)) they claimed that there is no evidence of preferentially spherical collapse. Furthermore, they claimed that the combined treatment of low (H1) and high density (molecular) data (by Crutcher et al. (2010)) with a joining condition drastically influenced the value of  $\kappa$ . They strongly asserted that  $B \propto \rho^{1/2}$  is the preferred scaling implied by the observational data and consistent with the prediction of the theoretical model.

## 1.5 Tracing the molecular clouds

Hydrogen is the most abundant species and also the primary constituent of the interstellar medium. Most hydrogen is in its atomic gas (HI) phase at low to intermediate temperature and densities ( $n_{\text{H}} < 10^2 \text{ cm}^{-3}$ ). However, within molecular clouds all hydrogen is mostly in its molecular form,  $\text{H}_2$ . Their excitation temperature for rotational emission is also much greater than the local cloud temperature. Thus they are extremely difficult to detect due to the low temperatures ( $\sim 10 \text{ K}$ ) that characterize such molecular clouds. Instead, less abundant traces but with much lower excitation lines, in particularly emission lines from CO molecules are often used to investigate the structure and the dynamics of the dense gas in molecular clouds. Thermal dust emission is also employed as discussed below.

Dust constitutes a very tiny fraction of the total mass of the ISM, with an approximate dust to gas ratio of 0.01 (Goldsmith et al., 1997). However, dust plays an extremely pivotal role as their emission (thermal continuum radiation) provides an effective cooling mechanism. They absorb photons emitted by young stars embedded in the cloud and re-radiate them at longer wavelengths. Dust continuum emission in submillimeter wavelengths, from cold dust along

the line of sight, can be used to determine the column density and the mass of the enclosed materials. Dust thermal radiation peaks at a submillimeter wavelength  $\lambda \sim 100 - 300\mu\text{m}$  and radiates as a modified black body. Although the dust continuum emission observations help to probe the detailed density structure of the molecular clouds and their embedded dense cores, there is no kinematic information from these data.

The observations of molecular line emission are an excellent probe to study the physical conditions as well as the kinematics within the molecular clouds. CO is the second most abundant species ( $10^{-4}$  fraction of molecular hydrogen) and is often used as a proxy for  $\text{H}_2$  to trace large-scale distribution of gas and velocities. These molecules can also be observed in different forms:  $^{12}\text{C}^{16}\text{O}$ ,  $^{13}\text{C}^{16}\text{O}$ , and  $^{12}\text{C}^{18}\text{O}$ , which have different optical depths. The isotopes of C or O in CO means that the emission is less likely to be absorbed along the line-of-sight by the other identical molecules since the isotopes bearing molecules are relatively few in number. The millimeter CO rotational emission line  $J = 1 \rightarrow 0$  has a critical density of  $n_{\text{crit}} = 3 \times 10^3$  particles  $\text{cm}^{-3}$ . Thus at densities below and near the critical density CO is a good tracer for the large-scale features of molecular clouds. However, for regions with higher column density CO ceases to be a reliable estimator as it freezes out on grain surfaces (Tafalla et al., 2002; Christie et al., 2012). Thus, denser regions ( $n \gtrsim 10^5 \text{cm}^{-3}$ ) are often largely depleted of carbon molecules, which forbids the use of their rotational lines as effective tracers. However, the choice of the molecular line depends on the specific part of the cloud that is being studied. For tracing the dense gas in the star-forming regions, nitrogen based species, such as  $\text{NH}_3$  and  $\text{N}_2\text{H}^+$ , are much preferred. These molecules are excited at the high densities ( $n \gtrsim 10^4 \text{cm}^{-3}$ ) and low temperature ( $T \lesssim 20 \text{K}$ ) that characterizes dense molecular cores. I discuss some of the general techniques to observe structural properties, particularly the column density PDF and velocity structure of dense cores, in molecular clouds using the above tracers.

### 1.5.1 Column density

The column density, which is one of the most important observed quantities, is typically defined as the number of particles along the line of sight divided by the projected area. There are various techniques of measuring column density in molecular clouds (for a review and historical application of these techniques see Pineda et al. (2008); Goodman et al. (2009)). The commonly used methods to map the column density in molecular clouds are: dust extinction mapping in near-infrared (Lada et al., 1994; Lada et al., 1999), emission map in far-infrared (Schlegel et al., 1998) and integrated intensity map of molecular-line emissions, particularly using  $^{12}\text{CO}$  or  $^{13}\text{CO}$  (Padoan et al., 1999). In case of dust extinction mapping the column density is calculated from the visual extinction of the starlight by the intervening dust (for example see Lombardi & Alves (2001)). For an assumed dust-to-gas ratio (typically 1%) the extinction is empirically related to column density as:  $A_v = (N_{\text{H}} + 2N_{\text{H}_2})/2 \times 10^{21}$ , where  $A_v$  is the extinction in magnitude,  $N_{\text{H}}$  and  $N_{\text{H}_2}$  are the column densities of the atomic and molecular hydrogen, respectively.

The other frequently used method is to measure column density from the far-infrared (thermal) dust emission flux. For a measured flux density  $S_\nu$  and solid angle  $\Omega$  the column density is given as  $N_{\text{H}_2} = S_\nu / (\kappa_\nu \mu m_{\text{H}} \Omega B_\nu(T_{\text{d}}))$ , where  $B_\nu(T_{\text{d}})$  is the blackbody emission from dust at temperature  $T_{\text{d}}$ ,  $\kappa_\nu \propto \nu^\beta$  is the dust opacity,  $m_{\text{H}}$  and  $\mu$  are the mass of hydrogen atom and mean molecular weight per hydrogen molecule respectively (Schnee et al., 2005)). The dust temperature is calculated using the measurements of two separate far-infrared wavelengths to fit an assumed emissivity law (for details see Schnee et al. (2005, 2008)).

Column density can also be measured by integrating over the line profile of relatively abundant molecules like  $^{12}\text{CO}$  or rarer but optically thin CO isotopologues like  $^{13}\text{CO}$ . These molecules undergo collisional excitation with the dominant  $\text{H}_2$ , followed by radiative de-excitation. The conversion between the molecular hydrogen column density  $N_{\text{H}_2}$  and the  $^{12}\text{CO}(1-0)$  integrated intensity  $W(^{12}\text{CO})$  is obtained using the so called  $X$ -factor,  $X = N_{\text{H}_2}/W(^{12}\text{CO})$  (Pineda et al., 2008).

Column density PDFs are of particular interest in understanding the influence of magnetic fields, turbulence, and gravity in star formation and are studied by both observers (e.g., Kainulainen et al. (2009); Lombardi et al. (2015)) and theorists (e.g., Vazquez-Semadeni (1994); Federrath et al. (2008)).

## 1.5.2 Filaments

Filamentary structures are observed in the nearby star-forming molecular clouds with the Herschel Space Observatory (Pilbratt et al., 2010) equipped with two cameras SPIRE (Griffin et al., 2010) and PACS (Poglitsch et al., 2010). The Herschel images (Men'shchikov et al., 2010; Arzoumanian et al., 2011) reveal an intricate network of elongated structures that are ubiquitous to star-forming regions. While the existence of filamentary structures is well established (Schneider & Elmegreen, 1979; Myers, 2009), the recent Herschel observations using submillimeter wavelength (70–500  $\mu\text{m}$ ) continuum maps of dust emission have revealed them with extraordinary resolution. Such networks are possibly the imprint of turbulent initial conditions (André et al., 2010; André, 2017). Given their omnipresence and the high degree of uniformity in their properties (Arzoumanian et al., 2011) they are likely to play a significant role in fragmentation and the formation process of dense cloud cores (André et al., 2010; Molinari et al., 2010). The dust temperature ( $T_d$ ) and the column density ( $\Sigma$ ) maps from the Herschel data are constructed using the weighted spectral energy distribution (SED) from the 5 observed SPIRE/PACS wavelengths. For an assumed dust temperature, the two free parameters  $T_d$  and  $\Sigma$  are derived from the fit of the SED by the grey-body function  $I_\nu = B_\nu(T_d)(1 - e^{-\tau_\nu})$  (for details refer to section 3 from Könyves et al. (2010)). Here  $I_\nu$  is the observed surface brightness and  $\tau_\nu = \kappa_\nu \Sigma$  is the dust optical depth at frequency  $\nu$ . The dust opacity per unit mass is approximated as a power-law,  $\kappa_\nu = 0.1 \times (\nu/1000\text{GHz})^2 \text{cm}^2/\text{g}$ , as advocated by Hildebrand (1983). For identifying the filaments the column density maps are decomposed into curvelets and wavelets (Starck et al., 2003). The high contrasting curvelet components are the filaments obtained after subtraction of the denser cores (the wavelet component). The DisPerSE algorithm (Sousbie, 2011) is used



to identify the filament ridges and characterize their structural properties.

### 1.5.3 Dense cores

Ammonia observations are the ideal tracer of the hierarchical fragmentation of star-forming regions. As they are typically immune to depletion they serve as a powerful probe of the kinematics of star-forming filaments and cores.  $\text{NH}_3$  is a symmetric top molecule with N at the top and the three H atoms at the base of the pyramid. The rotation inversion transition of  $\text{NH}_3$  acts as a useful probe to study cold dense interstellar clouds (particularly molecular cloud cores). The angular quantum numbers  $J$  and  $K$  describe the rotational states of  $\text{NH}_3$ . The rotational states  $(J, K)$  split into inversion doublets (characterized by  $\Delta J = 0$ ,  $\Delta K = 0$ ), due to the tunneling of the N atom through the plane of the three H atoms. The inversion spectra are further split into hyperfine structure due to the electric dipole and magnetic quadrupole moments. It is possible to derive (for details see Ho & Townes (1983)) the line opacity and the excitation temperature by fitting the frequency and the line strength of the  $(J, K)$  hyperfine structure. Over the past few decades  $\text{NH}_3$  observations (Jijina et al., 1999; Rosolowsky et al., 2008) are used to identify cores with various properties ranging from cold and quiescent (Goodman et al., 1998), in near-critical equilibrium (Benson & Myers, 1983), and with significant velocity gradients (Goodman et al., 1993). Recent sensitive and high resolution maps show a sharp spatial transition between the thermal and nonthermal line widths in dense cores (Pineda et al., 2010; Seo et al., 2015). The recent Green Bank Ammonia Survey (GAS) provides extensive  $\text{NH}_3$  emission maps of target regions B18 in Taurus, NGC 1333 in Perseus, L1688 in Ophiuchus, and Orion A (North) in the Gould Belt clouds. In Chapter 4 of this thesis we present a systematic study of the gas kinematics and magnetic field of the dense cores in the L1688 region of the Ophiuchus molecular clouds using the  $\text{NH}_3$   $(J, K) = (1, 1)$  and  $(2, 2)$  inversion lines from the GAS survey.

## 1.6 Chapter preview

In Chapter 2 (published in MNRAS, Auddy et al. (2018)) we explore the effect of magnetic fields on turbulent or quiescent molecular clouds in shaping their column density PDF. Our results provide a unified model for column density PDFs that accounts for peaked power-laws with different indices in one limit and lognormal plus power-law PDFs in another limit. For clouds with a supercritical mass-to-flux ratio (weak magnetic field), the column density PDF is a power-law with a peak associated with the background column density. The power-law index converges to an approximate value of  $\simeq -2$  when binned logarithmically, regardless of whether the initial condition is turbulent. For subcritical clouds (strong magnetic field) we found that the power-law is much steeper with index  $\simeq -4$  for linear perturbations (indicating a shallower core density profile and reduced star formation). However, for a turbulent initial conditions in subcritical clouds, the PDF is lognormal with a transition at high density to a power-law with index  $\simeq -2$ . Thus, in our model we explore a large dynamic range of magnetic field strength and find a clear indication that strong magnetic support plays a crucial role in regulating star formation. Additionally, the link between the structural properties (column density PDFs) and the ambient magnetic field strength (or mass-to-flux ratio) will serve as an indirect way to measure the magnetic field.

Chapter 3 is published in the *Astrophysical Journal*, Auddy et al. (2016). Herschel observations (Arzoumanian et al., 2011) revealed that the relationship between filament width and column density is relatively flat, unlike the simple expectation that width is inversely proportional to column density, based on a Jeans length analysis. We argued that the turbulent flow leads to compression in which the filament is like a ribbon whose width is set by the standoff between ram pressure and the magnetic pressure. We show that the ribbon width is independent of the local density, unlike the Jeans length. It depends only on the turbulent compression scale  $L_0$ , turbulent flow speed  $v_{t0}$  and ambient Alfvén speed  $v_A$  (see equation (8) in chapter 2). The vertical height is essentially the Jeans length set by the balance between internal pressure

and gravity. Eventually, gravitationally driven ambipolar diffusion leads to runaway collapse of the densest regions in the ribbon, where the mass-to-flux ratio has become supercritical. We use our model to calculate a synthetic observed relation between apparent width in projection versus observed column density. The relationship is relatively flat, in rough agreement with the observations.

Chapter 4 is submitted to the *Astrophysical Journal*, Auddy et al. (2018). Characterization and precise detection of magnetic fields in the interstellar medium is crucial in understanding the influence of magnetic fields in star formation. We have developed a “core field structure”(CFS) method, which is a new technique to determine magnetic field strength across dense cores using gas kinematics. The CFS method requires spatially resolved observations of the nonthermal velocity dispersion ( $\sigma_{NT}$ ) from the GAS of the L1688 region of Ophiuchus (Friesen et al., 2017) along with the column density map. The  $H_2$  column density ( $N(H_2)$ ) maps are derived from SCUBA-2 850 micron dust continuum map (Pattle et al., 2015) assuming a standard dust-to-gas mass ratio. The CFS method relies on the assumption that the non-thermal velocity dispersions are due to Alfvénic fluctuations. The main result is that the cores in L1688 Ophiuchus are mostly supercritical in the interior with a gradual transition towards a subcritical diffuse surrounding.

## Bibliography

Alves, J., Lombardi, M., & Lada, C. J. 2014, *A&A*, 565, A18

—. 2017, *A&A*, 606, L2

Andersson, B.-G., Lazarian, A., & Vaillancourt, J. E. 2015, *ARA&A*, 53, 501

André, P. 2017, *Comptes Rendus Geoscience*, 349, 187

André, P., Men'shchikov, A., Bontemps, S., et al. 2010, *A&A*, 518, L102

Arzoumanian, D., André, P., Didelon, P., et al. 2011, *A&A*, 529, L6

Auddy, S., Basu, S., & Kudoh, T. 2016, *ApJ*, 831, 46

—. 2018, *MNRAS*, 474, 400

Ballesteros-Paredes, J., Vázquez-Semadeni, E., Gazol, A., et al. 2011, *MNRAS*, 416, 1436

Basu, S. 2017, *ArXiv e-prints*, arXiv:1703.01542

Basu, S., & Auddy, S. 2017, *Mem. Soc. Astron. Italiana*, 88, 524

Basu, S., & Ciolek, G. E. 2004, *ApJ*, 607, L39

Basu, S., Ciolek, G. E., Dapp, W. B., & Wurster, J. 2009a, *New A*, 14, 483

Basu, S., Ciolek, G. E., & Wurster, J. 2009b, *New A*, 14, 221

Benson, P. J., & Myers, P. C. 1983, *ApJ*, 270, 589

Chandrasekhar, S., & Fermi, E. 1953, *ApJ*, 118, 113

Cho, J., & Lazarian, A. 2005, *ApJ*, 631, 361

Chomiuk, L., & Povich, M. S. 2011, *AJ*, 142, 197

Christie, H., Viti, S., Yates, J., et al. 2012, *MNRAS*, 422, 968

- Chyba, C. F., & Hand, K. P. 2005, *ARA&A*, 43, 31
- Ciolek, G. E., & Basu, S. 2006, *ApJ*, 652, 442
- Ciolek, G. E., & Mouschovias, T. C. 1994, *ApJ*, 425, 142
- Collins, D. C., Kritsuk, A. G., Padoan, P., et al. 2012, *ApJ*, 750, 13
- Collins, D. C., Padoan, P., Norman, M. L., & Xu, H. 2011, *ApJ*, 731, 59
- Crutcher, R. M. 1999, *ApJ*, 520, 706
- . 2012, *ARA&A*, 50, 29
- Crutcher, R. M., Wandelt, B., Heiles, C., Falgarone, E., & Troland, T. H. 2010, *ApJ*, 725, 466
- Davis, Jr., L., & Greenstein, J. L. 1951, *ApJ*, 114, 206
- Dobbs, C. L. 2008, *MNRAS*, 391, 844
- Draine, B. T., & Weingartner, J. C. 1996, *ApJ*, 470, 551
- . 1997, *ApJ*, 480, 633
- Elmegreen, B. G. 1979, *ApJ*, 232, 729
- . 2000, *ApJ*, 530, 277
- Elmegreen, B. G., & Scalo, J. 2004, *ARA&A*, 42, 211
- Evans, II, N. J., Dunham, M. M., Jørgensen, J. K., et al. 2009, *ApJS*, 181, 321
- Falgarone, E., Troland, T. H., Crutcher, R. M., & Paubert, G. 2008, *A&A*, 487, 247
- Federrath, C. 2016, *MNRAS*, 457, 375
- Federrath, C., & Klessen, R. S. 2012, *ApJ*, 761, 156
- . 2013, *ApJ*, 763, 51

- Federrath, C., Klessen, R. S., & Schmidt, W. 2008, *ApJ*, 688, L79
- Fiedler, R. A., & Mouschovias, T. C. 1992, *ApJ*, 391, 199
- . 1993, *ApJ*, 415, 680
- Friesen, R. K., Pineda, J. E., co-PIs, et al. 2017, *ApJ*, 843, 63
- Gillon, M. 2014, *Acta Astronautica*, 94, 629
- Girart, J. M., Rao, R., & Marrone, D. P. 2006, *Science*, 313, 812
- Goldsmith, P. F., Bergin, E. A., & Lis, D. C. 1997, *ApJ*, 491, 615
- Goodman, A. A., Barranco, J. A., Wilner, D. J., & Heyer, M. H. 1998, *ApJ*, 504, 223
- Goodman, A. A., Benson, P. J., Fuller, G. A., & Myers, P. C. 1993, *ApJ*, 406, 528
- Goodman, A. A., Pineda, J. E., & Schnee, S. L. 2009, *ApJ*, 692, 91
- Griffin, M. J., Abergel, A., Abreu, A., et al. 2010, *A&A*, 518, L3
- Han, J. L., & Zhang, J. S. 2007, *A&A*, 464, 609
- Hanawa, T., & Tomisaka, K. 2015, *ApJ*, 801, 11
- Hartmann, L. 2001, *AJ*, 121, 1030
- Hayashi, C. 1966, *ARA&A*, 4, 171
- Hayashi, C., & Nakano, T. 1965, *Progress of Theoretical Physics*, 34, 754
- Hayward, C. C., & Hopkins, P. F. 2017, *MNRAS*, 465, 1682
- Heiles, C., & Troland, T. H. 2004, *ApJS*, 151, 271
- . 2005, *ApJ*, 624, 773
- Hildebrand, R. H. 1983, *QJRAS*, 24, 267

- Ho, P. T. P., & Townes, C. H. 1983, *ARA&A*, 21, 239
- Indebetouw, R., & Zweibel, E. G. 2000, *ApJ*, 532, 361
- Jeans, J. H. 1902, *Philosophical Transactions of the Royal Society of London Series A*, 199, 1
- . 1929, *The universe around us*
- Jijina, J., Myers, P. C., & Adams, F. C. 1999, *ApJS*, 125, 161
- Kainulainen, J., Beuther, H., Henning, T., & Plume, R. 2009, *A&A*, 508, L35
- Kandori, R., Tamura, M., Tomisaka, K., et al. 2017, *ApJ*, 848, 110
- Klessen, R. S., Ballesteros-Paredes, J., Vázquez-Semadeni, E., & Durán-Rojas, C. 2005, *ApJ*, 620, 786
- Könyves, V., André, P., Men'shchikov, A., et al. 2010, *A&A*, 518, L106
- Krumholz, M. R., Burkhardt, B., Forbes, J. C., & Crocker, R. M. 2018, *MNRAS*, 477, 2716
- Kudoh, T., & Basu, S. 2008, *ApJ*, 679, L97
- . 2011, *ApJ*, 728, 123
- Lada, C. J., Alves, J., & Lada, E. A. 1999, *ApJ*, 512, 250
- Lada, C. J., Lada, E. A., Clemens, D. P., & Bally, J. 1994, *ApJ*, 429, 694
- Lada, C. J., Lombardi, M., & Alves, J. F. 2010, *ApJ*, 724, 687
- Langer, W. D. 1978, *ApJ*, 225, 95
- Larson, R. B. 1969, *MNRAS*, 145, 271
- . 1981, *MNRAS*, 194, 809
- Lazarian, A., & Hoang, T. 2007, *MNRAS*, 378, 910

- Li, H.-B., Goodman, A., Sridharan, T. K., et al. 2014, *Protostars and Planets VI*, 101
- Li, H.-B., Yuen, K. H., Otto, F., et al. 2015a, *Nature*, 520, 518
- Li, P. S., McKee, C. F., & Klein, R. I. 2015b, *MNRAS*, 452, 2500
- Li, Z.-Y., & Nakamura, F. 2004, *ApJ*, 609, L83
- Lingam, M., & Loeb, A. 2018, *International Journal of Astrobiology*, 17, 116
- Lizano, S., & Shu, F. H. 1989, *ApJ*, 342, 834
- Lombardi, M., & Alves, J. 2001, *A&A*, 377, 1023
- Lombardi, M., Alves, J., & Lada, C. J. 2015, *A&A*, 576, L1
- Mac Low, M.-M., & Klessen, R. S. 2004, *Reviews of Modern Physics*, 76, 125
- Mac Low, M.-M., Klessen, R. S., Burkert, A., & Smith, M. D. 1998, *Physical Review Letters*, 80, 2754
- Maury, A. J., Girart, J. M., Zhang, Q., et al. 2018, *MNRAS*, 477, 2760
- McKee, C. F., & Ostriker, E. C. 2007, *ARA&A*, 45, 565
- McKee, C. F., & Williams, J. P. 1997, *ApJ*, 476, 144
- Men'shchikov, A., André, P., Didelon, P., et al. 2010, *A&A*, 518, L103
- Mestel, L. 1965, *QJRAS*, 6, 265
- . 1966, *MNRAS*, 133, 265
- Mestel, L., & Spitzer, Jr., L. 1956, *MNRAS*, 116, 503
- Mocz, P., Burkhardt, B., Hernquist, L., McKee, C. F., & Springel, V. 2017, *ApJ*, 838, 40
- Molina, F. Z., Glover, S. C. O., Federrath, C., & Klessen, R. S. 2012, *MNRAS*, 423, 2680



Molinari, S., Swinyard, B., Bally, J., et al. 2010, *A&A*, 518, L100

Mouschovias, T. C. 1976a, *ApJ*, 206, 753

—. 1976b, *ApJ*, 207, 141

Mouschovias, T. C. 1978, in *IAU Colloq. 52: Protostars and Planets*, ed. T. Gehrels & M. S. Matthews, 209–242

Mouschovias, T. C. 1991, in *NATO Advanced Science Institutes (ASI) Series C, Vol. 342*, NATO Advanced Science Institutes (ASI) Series C, ed. C. J. Lada & N. D. Kylafis, 61

Mouschovias, T. C., Ciolek, G. E., & Morton, S. A. 2011, *MNRAS*, 415, 1751

Mouschovias, T. C., & Spitzer, Jr., L. 1976, *ApJ*, 210, 326

Myers, P. C. 2009, *ApJ*, 700, 1609

Myers, P. C., Dame, T. M., Thaddeus, P., et al. 1986, *ApJ*, 301, 398

Nakamura, F., & Li, Z.-Y. 2005, *ApJ*, 631, 411

—. 2008, *ApJ*, 687, 354

Nakano, T., & Nakamura, T. 1978, *PASJ*, 30, 671

Osterbrock, D. E. 1961, *ApJ*, 134, 270

Padoan, P., Bally, J., Billawala, Y., Juvela, M., & Nordlund. 1999, *The Astrophysical Journal*, 525, 318

Padoan, P., & Nordlund, Å. 1999, *ApJ*, 526, 279

—. 2002, *ApJ*, 576, 870

Palla, F., & Stahler, S. W. 2002, *ApJ*, 581, 1194

- Palmeirim, P., André, P., Kirk, J., et al. 2013, *A&A*, 550, A38
- Passot, T., & Vázquez-Semadeni, E. 1998, *Phys. Rev. E*, 58, 4501
- Pattle, K., Ward-Thompson, D., Kirk, J. M., et al. 2015, *MNRAS*, 450, 1094
- Pilbratt, G. L., Riedinger, J. R., Passvogel, T., et al. 2010, *A&A*, 518, L1
- Pineda, J. E., Caselli, P., & Goodman, A. A. 2008, *ApJ*, 679, 481
- Pineda, J. E., Goodman, A. A., Arce, H. G., et al. 2010, *ApJ*, 712, L116
- Planck Collaboration, Ade, P. A. R., Aghanim, N., et al. 2016, *A&A*, 586, A138
- Poglitsch, A., Waelkens, C., Geis, N., et al. 2010, *A&A*, 518, L2
- Pokhrel, R., Gutermuth, R., Ali, B., et al. 2016, *MNRAS*, 461, 22
- Qiu, K., Zhang, Q., Menten, K. M., et al. 2014, *ApJ*, 794, L18
- Robitaille, T. P., & Whitney, B. A. 2010, *ApJ*, 710, L11
- Rosolowsky, E. W., Pineda, J. E., Foster, J. B., et al. 2008, *ApJS*, 175, 509
- Schlegel, D. J., Finkbeiner, D. P., & Davis, M. 1998, *ApJ*, 500, 525
- Schnee, S., Li, J., Goodman, A. A., & Sargent, A. I. 2008, *ApJ*, 684, 1228
- Schnee, S. L., Ridge, N. A., Goodman, A. A., & Li, J. G. 2005, *ApJ*, 634, 442
- Schneider, S., & Elmegreen, B. G. 1979, *ApJS*, 41, 87
- Seo, Y. M., Shirley, Y. L., Goldsmith, P., et al. 2015, *ApJ*, 805, 185
- Shetty, R., & Ostriker, E. C. 2006, *ApJ*, 647, 997
- Shu, F. H. 1977, *ApJ*, 214, 488
- Shu, F. H., Adams, F. C., & Lizano, S. 1987, *ARA&A*, 25, 23

Sousbie, T. 2011, MNRAS, 414, 350

Starck, J. L., Donoho, D. L., & Candès, E. J. 2003, A&A, 398, 785

Stephens, I. W., Looney, L. W., Kwon, W., et al. 2013, ApJ, 769, L15

Strittmatter, P. A. 1966, MNRAS, 132, 359

Tafalla, M., Myers, P. C., Caselli, P., Walmsley, C. M., & Comito, C. 2002, ApJ, 569, 815

Tomisaka, K. 2014, ApJ, 785, 24

Tomisaka, K., Ikeuchi, S., & Nakamura, T. 1988, ApJ, 335, 239

Tritsis, A., Panopoulou, G. V., Mouschovias, T. C., Tassis, K., & Pavlidou, V. 2015, MNRAS, 451, 4384

Troland, T. H., & Crutcher, R. M. 2008, ApJ, 680, 457

Vazquez-Semadeni, E. 1994, ApJ, 423, 681

Ward, R. L., Wadsley, J., & Sills, A. 2014, MNRAS, 445, 1575

Wolleben, M., & Reich, W. 2004, A&A, 427, 537

Zuckerman, B., & Palmer, P. 1974, ARA&A, 12, 279

## **Chapter 2**

# **The Effect of Magnetic Fields and Ambipolar Diffusion on the Column Density Probability Distribution Function in Molecular Clouds**

In recent years there has been a growing interest in the study of the column density probability distribution function (PDF) of molecular clouds. This function is significant in current theories of star formation as it is used to explain the initial mass function (Padoan & Nordlund, 2002; Hennebelle & Chabrier, 2008), star formation rates (Padoan & Nordlund, 2011; Hennebelle & Chabrier, 2011; Federrath & Klessen, 2012) and star formation efficiencies (Federrath & Klessen, 2013) of molecular clouds. The PDF is the normalized histogram of the column density obtained from the measurement within some area of the sky that contains a molecular cloud. One way to measure the column density of a molecular cloud is using dust extinction and the reddening of the light of background stars in the near IR (Alves et al., 2001; Kainulainen et al., 2009; Alves et al., 2014). Furthermore, mid-infrared (IR) absorption (Bacmann et al., 2000), millimetre continuum emission (Ward-Thompson et al., 1999) and flux measurements

in optically thin lines (Tafalla et al., 2002) are the other commonly used methods to measure column density.

Early numerical investigation (Vazquez-Semadeni, 1994; Padoan et al., 1997; Passot & Vázquez-Semadeni, 1998; Padoan & Nordlund, 1999) through non-self-gravitating purely hydrodynamic isothermal simulations showed that a lognormal density PDF is a preferred outcome of the development of hierarchical structures. The next generation of magnetohydrodynamic (MHD) simulations of the interstellar medium including self-gravity (Scalo et al., 1998; Federrath et al., 2008) found evidence of a growing power law at high densities. It was natural to interpret that the volume density PDF follows an underlying lognormal distribution, with a departure to a power law at higher density as it develops gravitationally collapsed objects.

Recent observations by Kainulainen et al. (2009) are broadly consistent with the idea that the column density PDF has an underlying lognormal shape with an additional power law at high column density. They identified that active star-forming clouds have an excess of high column densities, which manifests in the nonlognormal wings of the PDF. In contrast, quiescent clouds without active star formation are fit well by a lognormal distribution over the whole range of observed column density. A *Herschel-SPIRE* survey of the Mon R2 giant molecular cloud (Pokhrel et al., 2016) found that the gas column density PDF is lognormal, but with a power-law tail with best-fit index  $\alpha = 2.15$  above  $\sim 10^{21} \text{ cm}^{-2}$ . These observations are consistent with the evolutionary trend where turbulent motions play the main role in shaping the cloud in the early stages, but core formation is dominated by gravity and possibly magnetic fields. Several numerical studies (Tassis et al., 2010; Ballesteros-Paredes et al., 2011; Ward et al., 2014) have subsequently shown that a power-law tail develops over time and its strength grows as the rate of star formation activity increases.

A recent survey by Lombardi et al. (2015) reconfirms the results from Kainulainen et al. (2009) that at a high extinction the PDFs are best fit with a power law. They measure the column density in terms of the K-band extinction  $A_K$  from the dust emission maps of Herschel and Planck data, and show that for  $A_K \geq 0.2$  mag, the PDFs ( $dN/d \log A_K \propto A_K^{-\alpha}$ ) have power-

law indices with  $\alpha \approx 2$ , but clouds with lower star formation activity, i.e. Polaris and Pipe, have  $\alpha = 3.9$  and  $\alpha = 3.0$ , respectively. Könyves et al. (2015) also find a power-law PDF for the Aquila star-forming cloud using Herschel data, with index  $\alpha \approx 2$ . Alves et al. (2017) extend the idea that PDFs of molecular clouds are only a power law, with slope varying from  $\alpha \approx 4$  for diffuse clouds to  $\alpha \approx 2$  for clouds with active star formation. This is consistent with the fact that steeper slopes mean a lack of high density material and thereby less star formation. However, a physical explanation of a steeper slope in such clouds has been lacking.

A key question is whether clouds with a strong magnetic field exhibit distinct features of column density PDFs in comparison to clouds with a weak magnetic field. The lognormal feature is often interpreted as a direct imprint of supersonic turbulence, which is believed to dominate the evolution of observed clouds (Vazquez-Semadeni, 1994). However, the recent work by Tassis et al. (2010) points out that lognormal column density PDFs may be a more generic feature of molecular clouds and should not be interpreted as a result of supersonic turbulence alone. Observationally there is also the claim by Alves et al. (2017) that the lognormal peak may be an artifact arising due data incompleteness, and thereby not a result of supersonic turbulence. Tassis et al. (2010) also show that gravitationally-driven ambipolar diffusion plays a significant role in shaping the PDFs. Furthermore, a thermally bi-stable numerical simulation by Ballesteros-Paredes et al. (2011) reveals that global gravitational contraction enhances the initial density fluctuations and results in a wider lognormal PDF and a power-law tail at later times. It is likely then that the column density PDFs of molecular clouds arise from a variety of initial conditions and can represent different evolutionary stages. Here, we explore the process of molecular cloud fragmentation based on the interplay of turbulence, gravity, and magnetic fields. While large scale turbulence sweeps up the interstellar medium and compresses the gas into filaments and shocks, magnetic fields can provide a global support against the collapse until gravitationally-driven ambipolar diffusion leads to a runaway collapse of the densest regions of the cloud (e.g. Nakamura & Li, 2005; Kudoh & Basu, 2011). In this paper, we explore the effect of the magnetic field, gravity, and ambipolar diffusion in determining the column density

PDFs. Our study follows the previous ones by Kudoh & Basu (2008, 2011). We carry out a parameter study by running a number of simulations with different initial conditions. Our main objective is to see the effect of large-scale magnetic fields and nonlinear initial perturbations on the time evolution of the column density PDF. We further investigate the differences in steepness of the power-law index of the column density PDF and connect them to different initial conditions. Since direct magnetic field measurements using the Zeeman effect (Crutcher, 2012) are rarely successful, a key goal is to find a link between the structural properties of molecular clouds and the ambient magnetic field strength (or mass-to-flux ratio).

Our paper is organised in the following manner. The numerical model and some background theory is discussed in Section 2.1, and the results from the simulations are given in Section 2.2. We provide more discussion of the results in Section 2.3 and give a summary in Section 2.4.

## 2.1 Theory and Numerical Model

Magnetic fields and ambipolar diffusion play an important role in the star formation process. They can regulate the cloud collapse and fragmentation process, control angular momentum evolution through magnetic braking, and possibly moderate the mass reservoir for stars by limiting the mass accretion from the magnetic envelope. The relative strength of gravity and the magnetic field is measured by the mass-to-flux ratio  $M/\Phi$ . There exists a critical mass-to-flux ratio  $(M/\Phi)_{\text{crit}}$  (Mestel & Spitzer, 1956; Mouschovias & Spitzer, 1976; Strittmatter, 1966; Tomisaka et al., 1988). For  $M/\Phi > (M/\Phi)_{\text{crit}}$ , the cloud is supercritical and is prone to indefinite collapse. However, for  $M/\Phi < (M/\Phi)_{\text{crit}}$  the cloud is subcritical and cannot collapse as long as magnetic flux freezing applies. For example,  $M/\Phi < (M/\Phi)_{\text{crit}} = (2\pi G^{1/2})^{-1}$  is required for stability against fragmentation for an infinite uniform layer that is flattened along the direction of the background magnetic field (Nakano & Nakamura, 1978). However, in nonideal MHD, neutral-ion slip leads to gravitationally-driven fragmentation on the ambipolar-diffusion

timescale (Langer, 1978; Ciolek & Basu, 2006; Mouschovias et al., 2011). In this project we focus on the fragmentation and core formation in nonideal MHD clouds. Kudoh et al. (2007) performed a three-dimensional simulation of the fragmentation and core formation in the subcritical clouds with ambipolar diffusion and gravitational stratification along the magnetic fields. Kudoh & Basu (2008, 2011) did a further parameter study to demonstrate that core formation occurs faster as the strength of the initial flow speed in the cloud increases.

### 2.1.1 Setup for numerical simulation

The numerical model used in this paper is similar to previous ones (Kudoh et al., 2007; Kudoh & Basu, 2008, 2011). We solve the three-dimensional nonideal magnetohydrodynamic (MHD) equations including self-gravity and ambipolar diffusion:

$$\frac{\partial \rho}{\partial t} + \mathbf{v} \cdot \nabla \rho = -\rho \nabla \cdot \mathbf{v}, \quad (2.1)$$

$$\frac{\partial \mathbf{v}}{\partial t} + (\mathbf{v} \cdot \nabla) \mathbf{v} = -\frac{1}{\rho} \nabla p + \frac{1}{c\rho} \mathbf{j} \times \mathbf{B} - \nabla \psi, \quad (2.2)$$

$$\frac{\partial \mathbf{B}}{\partial t} = \nabla \times (\mathbf{v} \times \mathbf{B}) + \nabla \times \left[ \frac{\tau_{ni}}{c\rho} (\mathbf{j} \times \mathbf{B}) \times \mathbf{B} \right], \quad (2.3)$$

$$\mathbf{j} = \frac{c}{4\pi} \nabla \times \mathbf{B}, \quad (2.4)$$

$$\nabla^2 \psi = 4\pi G \rho, \quad (2.5)$$

$$p = c_s^2 \rho, \quad (2.6)$$

where  $\rho$  is the density of the neutral gas,  $p$  is the pressure,  $\mathbf{v}$  is the velocity,  $\mathbf{B}$  is the magnetic field,  $\mathbf{j}$  is the electric current density,  $\psi$  is the self-gravitational potential and  $c_s$  is the sound speed. Equations (2.1) and (2.2) are the mass continuity and the momentum equations, respectively. Equation (2.3) is the magnetic induction equation. The neutral-ion collision time in equation (2.3) is given by

$$\tau_{ni} = 1.4 \frac{m_i + m_n}{\rho_i \langle \sigma w \rangle_{in}} \quad (2.7)$$



(e.g. Basu & Mouschovias, 1994), where  $\rho_i$  is the ion density and  $\langle\sigma w\rangle_{in}$  is the average collision rate between the ions of mass  $m_i$  and neutrals of mass  $m_n$ .

Furthermore, it is assumed that the temperature of the gas makes a step-like transition from a cool molecular gas to a warm surrounding medium at a height of  $z_c = 2H_0$  (see Eq. [18] of Kudoh & Basu (2011)) and that in the subsequent evolution each Lagrangian fluid particle is in isothermal equilibrium (Kudoh & Basu, 2003, 2006) so that

$$\frac{dc_s}{dt} = \frac{\partial c_s}{\partial t} + \mathbf{v} \cdot \nabla c_s = 0. \quad (2.8)$$

This means that each parcel of the molecular cloud and the surrounding warm gas retain their initial temperature. As an initial condition we set up the simulation box with a preferred direction of the uniform magnetic field. The self-gravitating cloud is in hydrostatic equilibrium along the direction of the magnetic field and forms a sheet-like geometry. The one-dimensional hydrostatic equilibrium can be calculated using the following equations:

$$\frac{dp}{dz} = \rho g_z, \quad \frac{dg_z}{dz} = -4\pi G\rho, \quad p = c_s^2\rho, \quad (2.9)$$

subject to boundary conditions  $g_z(z=0) = 0$ ,  $\rho(z=0) = \rho_0$ ,  $p(z=0) = \rho_0 c_{s0}^2$ , where  $\rho_0$  and  $c_{s0}$  are the initial density and the sound speed at  $z=0$ . The initial magnetic field is assumed to be uniform along the  $z$ -direction:  $B_z = B_0$ ,  $B_x = B_y = 0$ , where  $B_0$  is a constant. The simulation of the equilibrium gas sheet is started with random velocity perturbations ( $v_x = v_a R_m(x, y)$ ,  $v_y = v_a R_m(x, y)$ ,  $v_z = 0$ ) at each grid point where  $R_m$  is a random number with a spectrum  $v_k^2 \propto k^n$  in Fourier space and  $n$  is either  $-4$  or  $0$ . These correspond to turbulence or white noise, respectively. The turbulence is not replenished, and therefore allowed to decay freely. We use periodic boundaries in the  $x$ - and  $y$ - directions and a mirror-symmetric boundary condition at  $z=0$ . The computational region is  $-4\pi H_0 < x, y < 4\pi H_0$  and  $0 < z < 4H_0$ . The number of grid points in each direction is  $(N_x, N_y, N_z) = (256, 256, 20)$ .

Table 2.1:  $\beta_0$  is the initial ratio of thermal to magnetic pressure at  $z = 0$ ,  $v_a$  is the amplitude of the initial velocity fluctuation,  $t_{\text{core}}$  is the time needed for core formation.

Model	$\beta_0$	Spectrum	$v_a/c_s$	$t_{\text{core}}/t_0$	Comments
V1	0.25	$k^{-4}$	0.1	87.6	
V4	0.25	$k^{-4}$	3.0	16.9	Fiducial model
K1	0.25	$k^0$	3.0	95.7	
B3	4.0	$k^{-4}$	3.0	1.13	Initially supercritical
B4	9.0	$k^{-4}$	3.0	1.06	Initially supercritical
B8	4.0	$k^{-4}$	0.1	7.36	Initially supercritical

## 2.1.2 Numerical Parameters

As units of length, velocity and density we choose  $H_0 = c_{s0}/\sqrt{2\pi G\rho_0}$ ,  $c_{s0}$  and  $\rho_0$ , respectively. This naturally gives the unit of time  $t_0 \equiv H_0/c_{s0}$ . The ratio of the initial gas to magnetic pressure at  $z = 0$  introduces one dimensionless parameter,

$$\beta_0 = \frac{8\pi\rho_0 c_{s0}^2}{B_0^2}. \quad (2.10)$$

The parameter  $\beta_0$  is related to the normalized mass-to-flux ratio  $\mu_S \equiv 2\pi G^{1/2}\Sigma_S/B_0$  for Spitzer's self-gravitating cloud (Spitzer, 1942), in which  $\Sigma_S = 2\rho_0 H_0$ . Therefore,

$$\beta_0 = \mu_S^2. \quad (2.11)$$

Dimensional values of all the quantities can be found by specifying appropriate values for  $\rho_0$  and  $c_{s0}$ . For example, if  $c_{s0} = 0.2 \text{ km s}^{-1}$  and  $n_0 \equiv \rho_0/m_n = 10^4 \text{ cm}^{-3}$  where  $m_n = 2.33 \times 1.67 \times 10^{-24} \text{ g}$ , we obtain  $H_0 \simeq 0.05 \text{ pc}$ ,  $t_0 \simeq 2.5 \times 10^5 \text{ yr}$  and  $B_0 \simeq 40 \mu\text{G}$  if  $\beta_0 = 0.25$ . The unit of column density is  $\Sigma_0 = \rho_0 H_0 \simeq 6 \times 10^{-3} \text{ g cm}^{-2}$ , which corresponds to a number column density  $N_0 \equiv \tilde{\Sigma}_0/m_n \simeq 1.5 \times 10^{21} \text{ cm}^{-2}$ . We define  $\tilde{\Sigma} = \Sigma/\Sigma_0$  as the normalized column density.

## 2.2 Results

Table 2.1 summaries the simulation results for all the models and for different parameters. In the table we have listed the values of  $\beta_0$ , the form of power spectrum,  $v_k$ , and the amplitude of the initial velocity fluctuation  $v_a$ . We have also listed the core formation time  $t_0$ , which is defined as the time when the maximum density of a core reaches  $100\rho_0$ . Depending on the value of the initial mass-to-flux ratio, we have classified the models as subcritical ( $\beta_0 < 1$ ) or supercritical ( $\beta_0 > 1$ ). Model V1 and V4 are subcritical clouds, in which we have changed the amplitude of the initial velocity fluctuation  $v_a$  but with the turbulent spectrum fixed at  $v_k^2 \propto k^{-4}$ . Model K1 is also subcritical and has an initial velocity fluctuation  $v_a = 3.0 c_{s0}$  but the power spectrum is white noise,  $v_k^2 \propto k^0$ . In the models B3 to B8, we have  $\beta_0 > 1$ , and the cloud is supercritical with initial velocity fluctuation in both supersonic ( $v_a = 3.0 c_{s0}$ ) and subsonic ( $v_a = 0.1 c_{s0}$ ) limits. We are particularly interested in the column density PDF of the subcritical clouds where the magnetic support prevents rapid gravitational collapse. Instead, the cloud oscillates and settles into a quasiequilibrium state of filamentary structure due to the interplay of turbulence, magnetic support and gravitationally driven ambipolar diffusion (see Auddy et al. (2016) for details). Interestingly, the subcritical clouds with linear perturbations tend to have a much steeper slope in their column density PDF ( $\alpha \simeq 4$ ) as discussed later in Section 2.2.2.

### 2.2.1 General properties of the supercritical cloud

Here we discuss models that are initially supercritical with  $\beta_0 > 1$ . We consider a velocity spectrum  $v_k^2 \propto k^{-4}$  with both linear and nonlinear initial velocity amplitude. Figure 2.1 shows the time snapshot of the logarithmic column density at the end of the simulation for model B3 ( $t = 1.13 t_0$ ). This model starts with an initially supercritical mass-to-flux ratio with  $\beta_0 = 4$ . The figure shows the column density in the  $x - y$  plane at the end of the simulation when the maximum density is  $100\rho_0$ . The column density is obtained by integrating the sheet along the

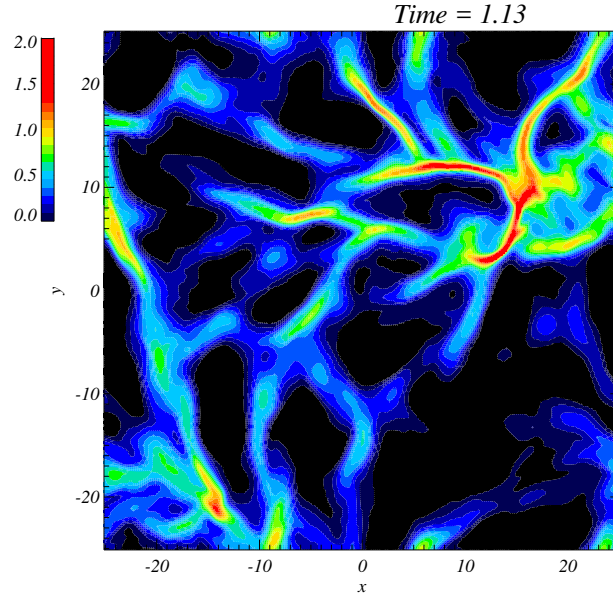


Figure 2.1: Logarithmic column density ( $\tilde{\Sigma} = \Sigma/\Sigma_0$ ) contours at  $t = 1.13 t_0$  for the model B3 with nonlinear velocity spectrum  $v_k^2 \propto k^{-4}$  of amplitude  $v_a = 3.0 c_{s0}$ . The model B3 is initially supercritical (i.e.  $\beta_0 = 4$ ). The  $x$  and  $y$  axes are in the units of  $H_0 \simeq 0.05$  pc. The maximum column density is located at  $(x, y) = (15.4 H_0, 8.3 H_0)$ . The unit of time is  $t_0 \simeq 2.5 \times 10^5$  yr. The panel shows the column density when viewed face on along the direction of the magnetic field ( $z$ -axis).

direction of the magnetic field ( $z$  axis). We assume that the cloud is viewed face on along the short axis whose width is typically set by the hydrostatic equilibrium along the magnetic field.

Figure 2.2 shows the time snapshot of the logarithmic column density for model B8 at  $t = 7.36 t_0$ . Model B8 corresponds to a linear perturbation with initial velocity amplitude  $v_a = 0.1 c_{s0}$ . All the other parameters are the same as model B3. The core formation time for model B3 ( $t = 1.13 t_0$ ) with nonlinear velocity perturbation is much less than for model B8 ( $t = 7.36 t_0$ ) with a linear perturbation. Furthermore, visual inspection of Figures 2.1 and 2.2 shows that the column density distribution for model B3 is much more filamentary than for model B8. The filaments in model B3 are distributed throughout the simulation region, with some of them having more condensed regions with higher column density. The maximum column density is located at  $(x, y) = (15.4 H_0, 8.3 H_0)$ . Model B8 evolves much more slowly until one of two dense regions go into a runaway collapse due to gravity. The maximum column density for model B8 is located at  $(x, y) = (14.8 H_0, 9.3 H_0)$ . The denser filamentary network in

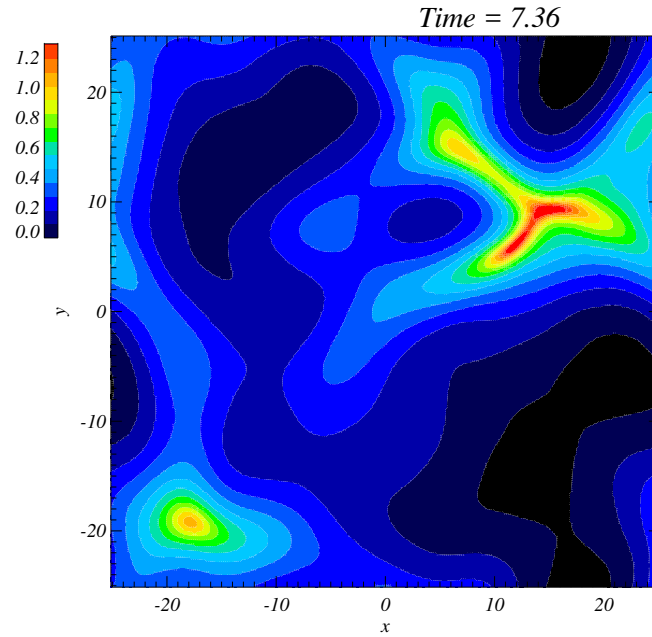


Figure 2.2: Logarithmic column density contours at  $t = 7.36 t_0$  for the model B8 with linear initial velocity amplitude  $v_a = 0.1 c_{s0}$ . All the other parameters are the same as model B3. The panel shows the column density when viewed face on along the direction of the magnetic field ( $z$ -axis).

model B3 can be attributed to the initial velocity amplitude that is 30 times greater than that in model B8. As the clouds are supercritical to begin with, the large-scale supersonic turbulence condenses the gas and gravity causes the dense regions to go into a runaway collapse. In model B4 we further decrease the strength of the magnetic field, keeping all the other parameters similar to model B3. The intrinsic nature of the column density remains the same only with a tiny difference in the core formation time as shown in Table 2.1. The presence of a weak magnetic field does not seem to have a strong impact compared to the decaying turbulence and gravity in the evolution of these supercritical clouds.

### The Column Density PDFs for supercritical clouds

Figures 2.3 and 2.4 show the column density PDFs along with the best-fit modified lognormal power law (MLP) and Pareto distributions (Clauset et al., 2009), for the two models B3 and

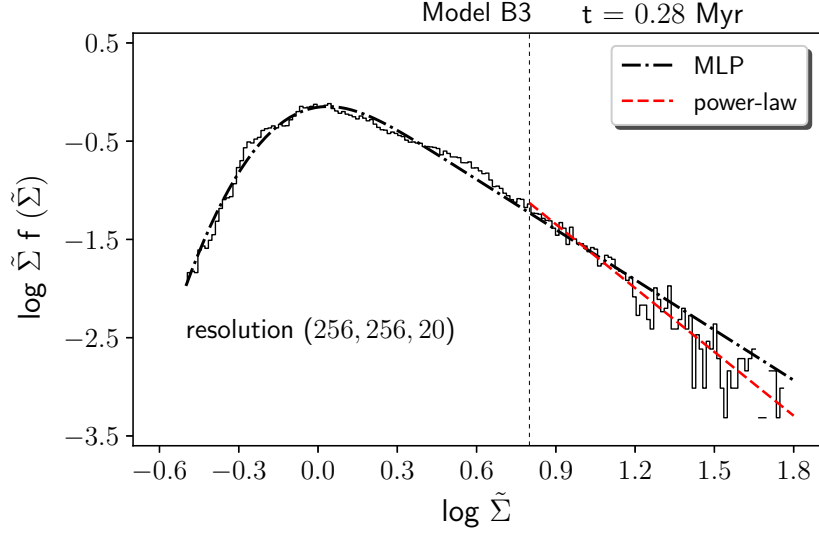


Figure 2.3: The column density PDF of model B3 at  $t = 0.28$  Myr. The dashed-dotted line is the best-fit MLP distribution with parameters  $\alpha = 1.7$ ,  $\mu_0 = -0.25$ , and  $\sigma_0 = 0.37$ . The vertical axis is  $\log \tilde{\Sigma} f(\tilde{\Sigma}) = \log(\Delta N' / \Delta \log \tilde{\Sigma})$ , where  $\Delta N' = \Delta N / (N_{\text{total}} \ln(10))$  and  $\Delta \log \tilde{\Sigma} = 0.01$ . The dashed red line is the best-fit power law to the tail of the column density PDF ( $\log \tilde{\Sigma} \geq 0.8$ ) with power-law index  $\alpha = 2.2$ . All fits are done using maximum likelihood estimation and are independent of binning.

B8, respectively. The MLP distribution is a three-parameter PDF given in closed form as

$$f(\Sigma) = \frac{\alpha}{2} \exp(\alpha \mu_0 + \alpha^2 \sigma_0^2 / 2) \Sigma^{-(1+\alpha)} \times \operatorname{erfc}\left(\frac{1}{\sqrt{2}} \left(\alpha \sigma_0 - \frac{\ln \Sigma - \mu_0}{\sigma_0}\right)\right), \quad \Sigma \in [0, \infty) \quad (2.12)$$

(Basu et al., 2015). Here  $\Sigma$  is the column density of the molecular cloud, and the three parameters describing the MLP distribution are  $\alpha$ ,  $\mu_0$  and  $\sigma_0$ . The power-law tail is represented by  $\alpha$ , while  $\mu_0$  and  $\sigma_0$  describe the body of the distribution (see Basu et al. (2015) for details). Here, we find the set of parameters for the MLP distribution that fits the normalized column density PDF. The relative similarity in the normalized column density PDFs for both the models is evident in the fit parameters. Figure 2.3 shows the normalized column density PDF of model B3 obtained at the end of the simulation at  $t = 1.13 t_0$ , i.e. 0.28 Myr. Here we plot  $\log(\Delta N' / \Delta \log \tilde{\Sigma}) \equiv \log \tilde{\Sigma} f(\tilde{\Sigma})$ , where  $\Delta N' = \Delta N / (N_{\text{total}} \ln(10))$  and  $\Delta \log \tilde{\Sigma} = 0.01$  with  $\log \tilde{\Sigma}$  in the horizontal axis. We fit the MLP distribution using the maximum likeli-

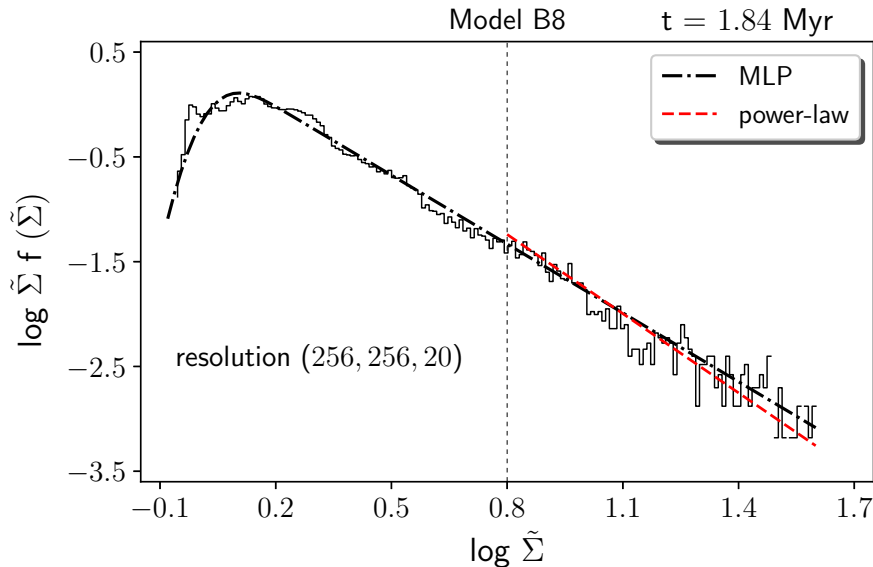


Figure 2.4: The column density PDF of model B8 at  $t = 1.84$  Myr. The dashed-dotted line is the best-fit MLP distribution with parameters  $\alpha = 2.2$ ,  $\mu_0 = 0.06$ , and  $\sigma_0 = 0.14$ . The dashed red line is the best-fit power law to the tail of the column density PDF ( $\log \tilde{\Sigma} \geq 0.8$ ) with power-law index  $\alpha = 2.5$ .

hood estimation (Johnson et al., 2002). The best-fit parameters are  $\alpha = 1.7$ ,  $\mu_0 = -0.25$ ,  $\sigma_0 = 0.37$ . For all the fitting routines we have used the *PYTHON* optimization module *scipy.optimize.differential.evolution* and *scipy.optimize.basinhopping* to find the global minimum of the function. Figure 2.4 shows the normalized column density PDF of model B8 obtained at the end of the simulation at  $t = 7.36 t_0$ , i.e. 1.84 Myr. Similarly, we fit the MLP to  $\tilde{\Sigma} f(\tilde{\Sigma})$  using the maximum likelihood estimation (MLE) method. We note that the MLE fits are independent of binning. The best-fit parameters are  $\alpha = 2.2$ ,  $\mu_0 = 0.06$ , and  $\sigma_0 = 0.14$ .

For both the models B3 and B8 we also fit the Pareto distribution ( $f(\Sigma) \propto \Sigma^{-(1+\alpha)}$ ) to the tail of the column density PDF, i.e. where  $\log \tilde{\Sigma} \geq 0.8$ . In Figures 2.3 and 2.4, the dashed red line represents the best-fit power law using MLE, yielding  $\alpha = 2.2$  and  $\alpha = 2.5$  for model B3 and B8, respectively. The power-law fits are slightly steeper than the MLP fits. This is because the MLP gives a global fit to the entire distribution, including the turnover at the lower column density values. Thus, depending on the turnover point the MLP fits adjust accordingly and give a global representation of the entire distribution. We performed several simulations with

same initial conditions but different (increased) spatial resolution, different random perturbation seeds, and different fitting routines, and found that the value of the measured power-law index  $\alpha$  has a variability of 10% – 20%. The slightly steeper slope for model B8 can be attributed to the smaller initial velocity perturbation. There are fewer regions with dense gas compared to model B3 as evident in Figures 2.1 and 2.2. The column density PDF for model B3 with nonlinear perturbations has a wider spread (indicated by  $\sigma_0$ ) compared to model B8 with linear perturbations. More importantly, for both these supercritical models, the power law establishes itself at a very early stage of evolution so there is no significant observable time with a lognormal PDF. The power law dominates almost the entire distribution since many regions go into direct collapse, i.e. there is a global fragmentation and gravitational collapse.

### 2.2.2 General properties of the subcritical cloud

We discuss the result of model V4 as a fiducial model, where the cloud has  $\beta_0 = 0.25$ , corresponding to a normalized mass-to-flux ratio of about 0.5. We initiate the simulation with an initial nonlinear turbulent velocity perturbation of amplitude  $v_a = 3.0 c_{s0}$ . Figure 2.5 shows the time snapshot of the logarithmic column density colour map of model V4. The snapshot is obtained at the end of the simulation, when the maximum density is  $100\rho_0$ . The figure shows the column density in the  $x$ – $y$  plane that is obtained by integrating the sheet along the direction of the magnetic field ( $z$ –axis).

Figure 2.6 shows the time snapshot of the logarithmic column density at the end of the simulation for model V1. The model V1 corresponds to linear perturbations with  $v_a = 0.1 c_{s0}$ . All the other parameters are same as the fiducial model V4. One of the main differences between model V4 and V1 is the core formation time. It is  $t = 16.9 t_0$  for model V4 but a much longer time  $t = 87.6 t_0$  for model V1 with its initial linear perturbation. By visual inspection of Figures 2.5 and 2.6, one can also see the morphological difference in the distribution of dense structures. The fiducial model is much more filamentary and has more evolved collapsing cores within the vicinity of the maximum column density located at  $(x, y) = (14.8 H_0, -9.5 H_0)$ .



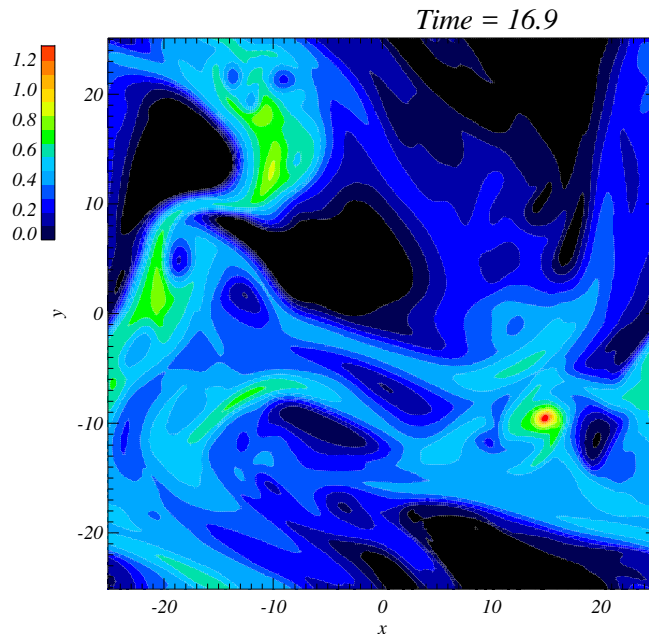


Figure 2.5: Logarithmic column density contours at  $t = 16.9 t_0$  for the model V4. The model V4 is the fiducial model, in which the turbulent spectrum is  $v_k^2 \propto k^{-4}$  with the initial velocity amplitude  $v_a = 3 c_{s,0}$ . This is a subcritical cloud with the initial mass-to-flux ratio of about 0.5 (i.e.  $\beta_0 = 0.25$ ). The unit of time is  $t_0 \simeq 2.5 \times 10^5$  yr. The figure shows the column density when viewed face on along the direction of the magnetic field ( $z$ -axis).

Although model V1 has evolved much longer than model V4, the weak velocity perturbation causes very little compression of the gas. Furthermore, the presence of strong magnetic support prevents the gas from collapsing due to self-gravity. The dense regions settle into an oscillatory equilibrium between magnetic and gravitational forces, with the neutrals gradually diffusing through the field lines due to ambipolar diffusion and forming denser regions.

Figure 2.7 shows a time snapshot of the column density of model K1 at the end of the simulation. Model K1 has a turbulent spectrum  $v_k^2 \propto k^0$  with all the other parameters same as the fiducial model. Although a flat spectrum is not consistent with observations, we use it to compare with the fiducial model. The white noise turbulence creates compressions in the initial stages that are more localized than in model V4 and they are not filamentary. Eventually, ambipolar diffusion leads to the formation of widely distributed cores. The core formation time ( $t = 95.7 t_0$ ) is much longer than in the fiducial model. Furthermore, the cores are mostly circular in shape with a lack of filamentary structures.

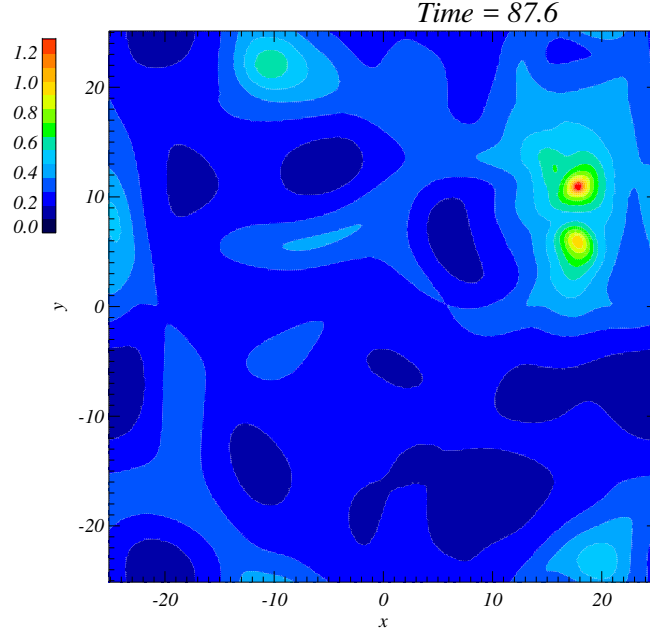


Figure 2.6: Logarithmic column density contours at  $t = 87.6 t_0$  for the model V1 corresponding to the initial velocity amplitude  $v_a = 0.1 c_{s0}$ . This is also a subcritical cloud (similar to ModelV4) with the initial mass-to-flux ratio of about 0.5 (i.e.  $\beta_0 = 0.25$ ) with the turbulent spectrum is  $v_k^2 \propto k^{-4}$ . The unit of time is  $t_0 \simeq 2.5 \times 10^5$  yr. The figure shows the column density when viewed face on along the direction of the magnetic field ( $z$ -axis).

### The column density PDFs for subcritical clouds

Figure 2.8 shows the time evolution of the column density PDF of the fiducial model V4. Here we plot  $\log(\Delta N' / \Delta \log \tilde{\Sigma}) \equiv \log \tilde{\Sigma} f(\tilde{\Sigma})$  and show the snapshots at different times of the column density starting from  $t = 10 t_0$ , (i.e.  $t = 2.50$  Myr) till the end of the simulation when the maximum density is  $100 \rho_0$ . The time corresponding to each snapshot is indicated on the top of each panel. In each panel, the PDF is overplotted with the best-fit lognormal distribution

$$f(\Sigma) = \frac{1}{\Sigma \sqrt{2\pi}\sigma} \exp\left(-\frac{(\ln \Sigma - \mu)^2}{2\sigma^2}\right) \quad (2.13)$$

(till the cutoff point  $\tilde{\Sigma} = 6.3$ ). We fit the lognormal distribution using MLE and the fit parameters  $\mu$  and  $\sigma$  of the successive epochs during the time evolution are shown in each panel.

The first panel on the top left of Figure 2.8 is a snapshot of the column density PDF at a very early stage of evolution. The PDF is predominantly lognormal with a broad spread

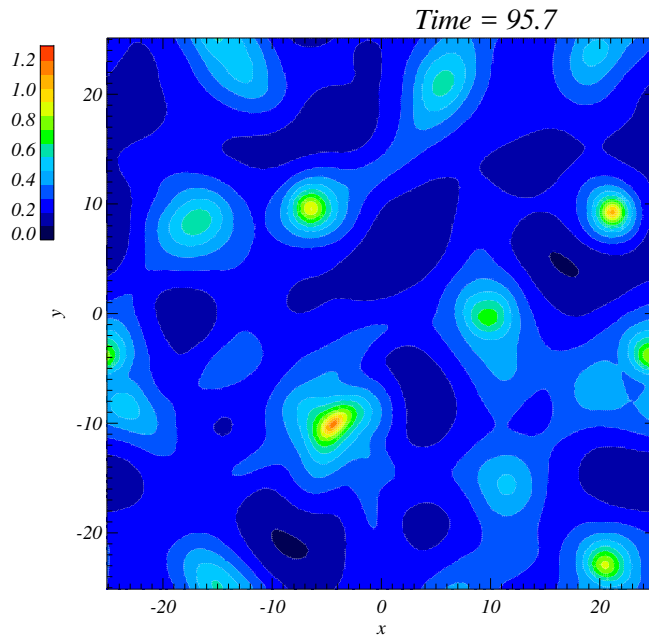


Figure 2.7: Logarithmic column density contours at  $t = 95.7 t_0$  for the model K1. The model K1 has a turbulent spectrum  $v_k^2 \propto k^0$ . All other initial conditions are same as the fiducial model V4. The initial velocity amplitude  $v_a = 3 c_{s0}$  and initial mass-to-flux ratio is about 0.5 (i.e.  $\beta_0 = 0.25$ ). The unit of time is  $t_0 \approx 2.5 \times 10^5$  yr. The figure shows the column density when viewed face on along the direction of the magnetic field ( $z$ -axis).

about its mean. A best-fit lognormal distribution (black dashed line) has the parameter values  $\mu = 0.60$  and  $\sigma = 0.35$ . The lognormal shape in the early stages can be attributed to the initial nonlinear perturbation (Vazquez-Semadeni, 1994) (discussion in the next section). As the cloud evolves further, it gets compressed due to the large-scale flow and develops some pockets of high column density. Then it rebounds and shows oscillation. Thus with each successive compression more regions with high column density develop. The maximum density is also strongly increased during each compression (see figure 14 in Kudoh & Basu (2011)) due to the supersonic flow. This feature is very pronounced in Figure 2.8 where we see the width of the column density PDF gradually widens over time (see also Ward et al. (2014); Tassis et al. (2010)), hence it is not just a fixed value solely depending on the initial strength of the nonlinear perturbation (supersonic turbulence)<sup>1</sup>. This is shown in the increase in the value of

<sup>1</sup>Although the width is growing as turbulence decays (decreasing Mach number), the final column density PDF (see section 2.2.2) is consistent with the trend found in hydrodynamic simulations with driven turbulence (e.g., Federrath & Klessen (2013)), where greater initial Mach number corresponds to a wider PDF.

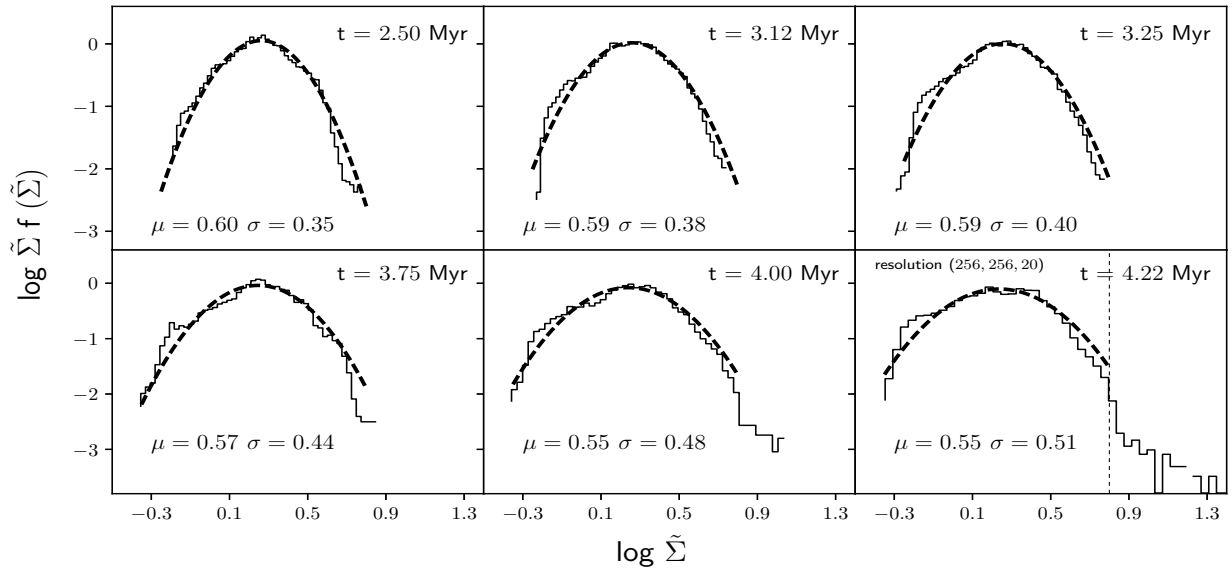


Figure 2.8: The time evolution of the column density PDF of the fiducial model V4 along with the best-fit lognormal distribution in the normalized form. The time corresponding to each snapshot is indicated on the top of each panel. The value of the fit parameters  $\mu$  and  $\sigma$  are also shown on the bottom left corner on individual panels. The dotted black line parallel to the  $y$ -axis at  $\log_{10} \tilde{\Sigma} = 0.8$  on the final subplot marks the power-law zone.

the lognormal fit parameter  $\sigma$ . After several oscillations, the local pockets of higher column density become supercritical and go into a runaway collapse. The column density PDF retains its lognormal shape for the most part of the evolution. However, at around  $t = 4.00$  Myr, it builds up regions of high column density. A distinct power-law tail gradually emerges, as seen in the bottom row of Figure 2.8.

To resolve the high density regions and highlight the power law at the final snapshot, we further perform a simulation with same initial conditions as model V4 but with twice the spatial resolution. Therefore  $(N_x, N_y, N_z) = (512, 512, 40)$ , and we follow the simulation till the maximum density is  $100\rho_0$ . As reported previously in Kudoh & Basu (2011), the core formation time becomes slightly shorter for the high-resolution cases. In the case of model V4 the core formation time is  $t = 14.2 t_0$ . It should be noted that the realization of the random perturbation to the initial velocity fluctuations are also not the same when adopting a different resolution (see Kudoh & Basu (2011) for details). Figure 2.9 shows the best-fit power law (red dashed

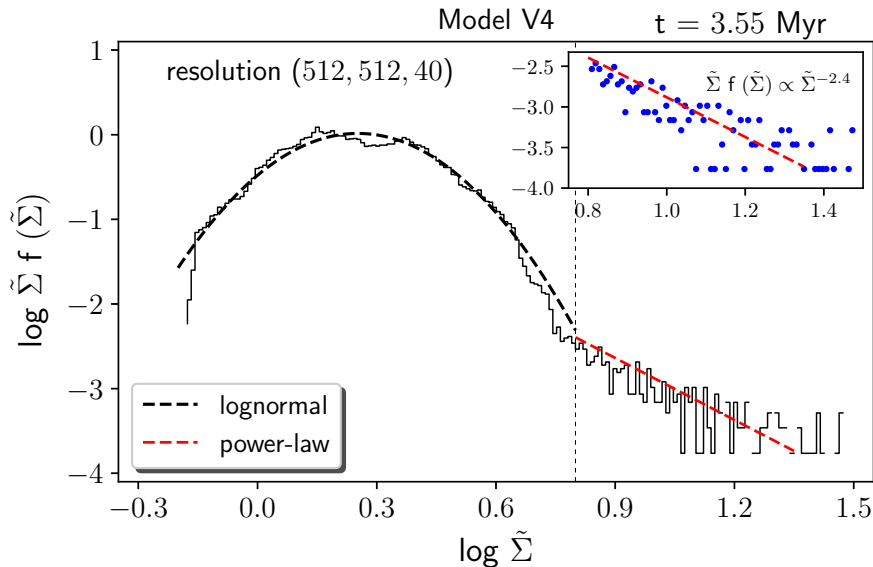


Figure 2.9: The column density PDF of model V4 at  $t = 3.55$  Myr with spatial resolution (512,512,40). The dashed black line is best-fit lognormal distribution using the maximum likelihood estimation and has parameters  $\mu_0 = 0.58$  and  $\sigma_0 = 0.39$ . The dashed red line represents the best-fit power law using maximum likelihood with power-law index  $\alpha = 2.4$ . The two regions are separated by a dotted black line at  $\log \tilde{\Sigma} = 0.8$ . The inset box on the top right corner is a zoomed in view of the power-law region along with the best-fit line.

line) along with the best-fit lognormal distribution (black dashed line) for the fiducial model V4 but for a higher spatial resolution (512, 512, 40). The zoomed-in inset box on the upper right corner in Figure 2.9 shows the power-law fit in the  $\log \tilde{\Sigma} f(\tilde{\Sigma})$  vs  $\log \tilde{\Sigma}$  plot, which has an index  $\alpha = 2.4$ . The gradual development of a power-law tail in the later stages of the evolution can be attributed to gravitationally-driven ambipolar diffusion occurring within the compressed filaments (see Kudoh & Basu (2014) for an analytic model). The neutrals drift past the field lines to form supercritical pockets within the filaments, on a somewhat shortened ambipolar diffusion time scale, and rapid collapse ensues in those regions.

Figure 2.10 shows the normalized column density PDF of model K1 along with the best-fit MLP distribution. The best-fit parameters are  $\alpha = 4.0$ ,  $\mu_0 = 0.37$ ,  $\sigma_0 = 0.09$ . This model has a flat spectrum  $v_k^2 \propto k^0$ , but is otherwise the same as the fiducial model V4. The white noise turbulence creates compressions in the initial stages that are more localized than in model V4 and they are not filamentary. Eventually, ambipolar diffusion leads to the formation of widely

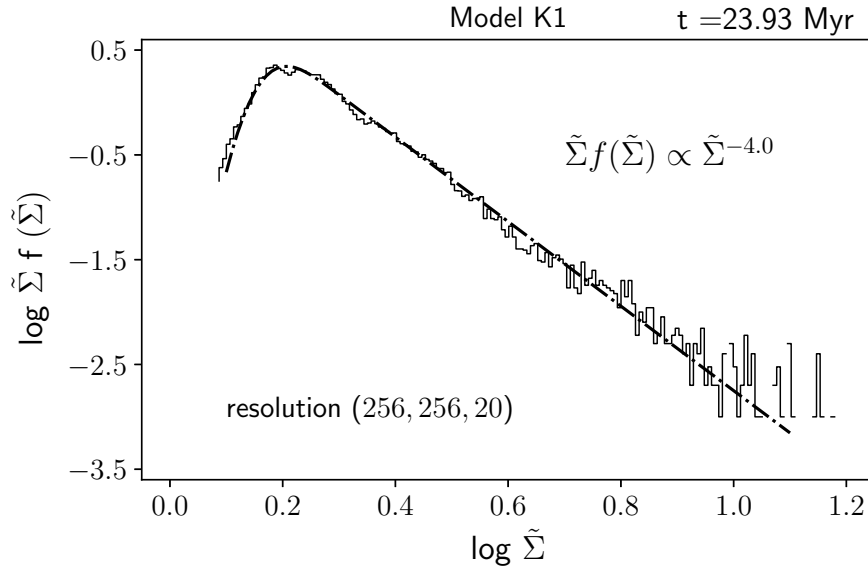


Figure 2.10: MLP fit to the column density PDF of model K1 at  $t = 23.93$  Myr. The best-fit parameter values are  $\alpha = 4.0$ ,  $\mu_0 = 0.37$ , and  $\sigma_0 = 0.09$ .

distributed cores. The formation process of the cores is ultimately more similar to that of model V1 (linear perturbations) discussed below, as there are no large scale density compressions that create a filamentary structure (see also Basu et al. (2009)). An ensemble of cores formed through ambipolar diffusion is expected to have a very steep column density PDF as explained in Section 2.3.

### Effect of Initial Velocity Amplitude

Model V1 has same initial conditions as our fiducial model V4 but with varying velocity perturbation amplitude  $v_a$ . The characteristics of the column density PDF of this model are studied using the best-fit MLP distribution. Figure 2.11 shows the normalized column density PDF of the model V1 obtained at the end of the simulation at  $t = 87.6 t_0$ , i.e. 21.90 Myr. We fit the MLP distribution to  $\tilde{\Sigma} f(\tilde{\Sigma})$  using MLE. The best-fit parameters are  $\alpha = 4.3$ ,  $\mu_0 = 0.40$ ,  $\sigma_0 = 0.06$ .

With the best-fit MLP distribution, it is relatively easy to quantify several important properties of the column density PDF for the subcritical cloud with different initial velocity fluctua-

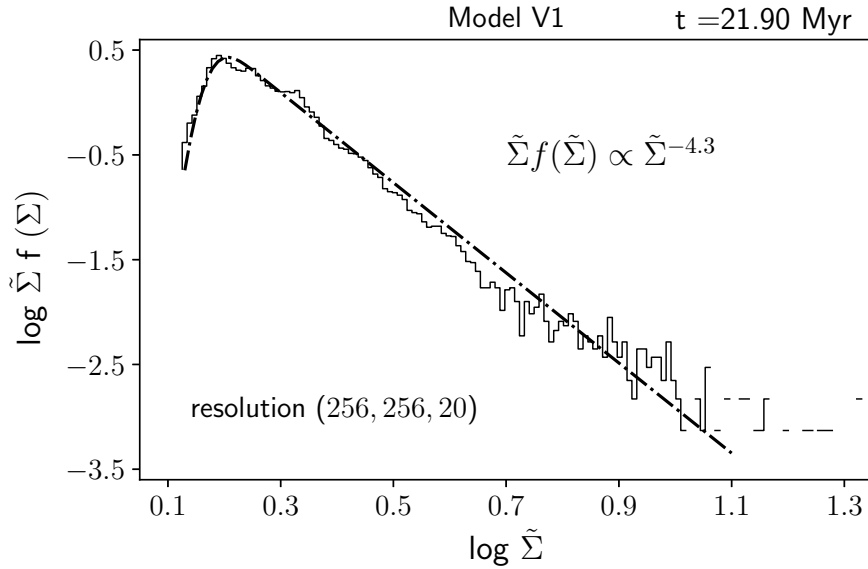


Figure 2.11: The column density PDF of model V1 at  $t = 21.90$  Myr. The dashed-dotted line is the best-fit MLP distribution with parameters  $\alpha = 4.3$ ,  $\mu_0 = 0.40$ , and  $\sigma_0 = 0.06$ .

tions. For both the models, the magnetic field provides the dominant support against collapse in the initial subcritical phase. The fiducial model V4 with nonlinear turbulence goes through an oscillatory filamentary phase, with magnetic pressure and tension acting like a spring working against the initial compression.

A major part of the evolution is dominated by a lognormal distribution as seen in Figure 2.8. However, model V1 does not show any oscillations. It settles into a quasiequilibrium between gravitational and magnetic forces and evolves rather slowly compared to model V4. While Figure 2.9 shows that the power law is prominent only at higher column densities ( $\log \tilde{\Sigma} \geq 0.8$ ) in model V4, for model V1 the power law is not only steep but extends all the way to much lower values of column density as shown in Figure 2.11. The value of  $\alpha$  is relatively high in the  $\log(\tilde{\Sigma} f(\tilde{\Sigma}))$  vs  $\log \tilde{\Sigma}$  plot. Another obvious distinction between the two PDFs is the spread of the distribution indicated by the values of the fit parameters  $\sigma$  and  $\sigma_0$ . The fiducial model has a much broader distribution ( $\sigma = 0.39$ ) compared to the model V1 ( $\sigma_0 = 0.06$ ). The difference in the spread of the PDF between the models is a natural imprint of the differing initial velocity perturbation amplitude  $v_a$ . The supersonic turbulent initial condition for model V4 results in a

Table 2.2: Fit parameters for the MLP distribution to the column density PDF for models with different initial conditions.

Model	$\alpha$	$\mu_0$	$\sigma_0$
V1	4.3	0.40	0.06
K1	4.0	0.37	0.09
B3	1.7	-0.25	0.37
B4	1.8	-0.55	0.17
B8	2.1	0.06	0.14

wider spread of the distribution compared to model V1.

### 2.2.3 Comparison of PDFs

Figure 2.12 is a composite plot that shows the column density PDFs of simulated molecular clouds with four different initial conditions. The vertical axis is the normalized frequency  $\Delta N' = \Delta N / (N_{\text{total}} \ln(10))$  with the data binned with a uniform spacing of  $\Delta \log \tilde{\Sigma}$ . The horizontal axes are  $\log \tilde{\Sigma}$  on the top and number column density  $N_{\text{H}_2}$  in  $\text{cm}^{-2}$  at the bottom, where  $N_{\text{H}_2} = \tilde{\Sigma} N_0$ . The column density PDF for clouds with supercritical mass-to-flux ratio (red and black histogram) is mostly power law above  $\sim 10^{21} \text{ cm}^{-2}$ . In contrast, models with strong magnetic field show different characteristics. The column density PDF of the subcritical model V4 (blue histogram) is predominantly lognormal with a power-law tail above  $\approx 9 \times 10^{21} \text{ cm}^{-2}$ . Furthermore, for model V1 the column density PDF is primarily a power law (no lognormal body) like the supercritical cases but with a much steeper slope. We summarize the fit parameters of the MLP function for all models (except V4) in Table 2.2.

## 2.3 Discussion

What role does a strong magnetic field play in shaping the column density PDFs and controlling star formation? Many theorists (Kritsuk et al., 2011; Federrath & Klessen, 2013) assert that an increasing magnetic field strength acts as an extra cushion against turbulent compression but



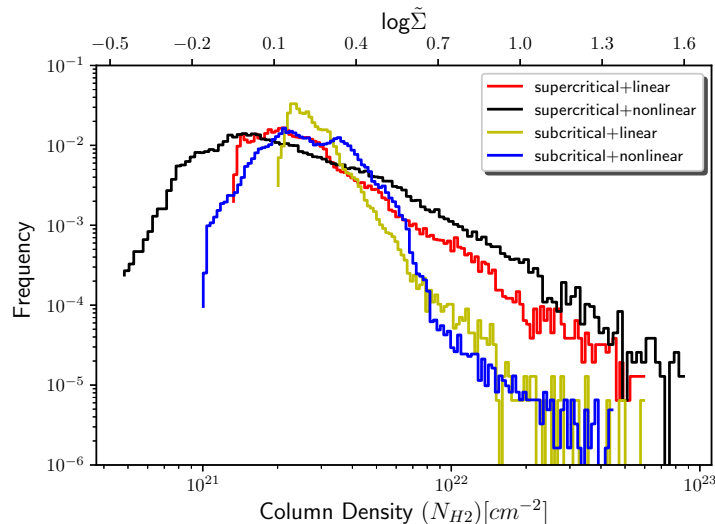


Figure 2.12: The column density PDFs of simulated models of molecular cloud with different initial conditions. The red and the black histogram are the supercritical model B8 and B3 with linear and nonlinear perturbation respectively. The yellow and the blue histogram are both subcritical clouds with linear (model V1) and nonlinear perturbation (model V4) respectively. The vertical axis is the normalized frequency  $\Delta N' = \Delta N / (N_{\text{total}} \ln(10))$  with the data binned with a uniform spacing of  $\Delta \log \tilde{\Sigma} = 0.018$ . Blue histogram is the high resolution (512,512,40) version of model V4.

has no definite influence on the power-law slope of the PDFs. Some indicate a weak steepening of the power-law tail with increasing magnetic field strength (Collins et al., 2012). Our models explore a larger dynamic range of magnetic field strength and instead demonstrate a clear trend where subcritical models (strong magnetic field) with linear perturbations show minimum star formation and have a steep power-law tail with index  $\alpha \approx 4$ . This broadly agrees with recent observational results from Herschel and Planck (Lombardi et al., 2015; Alves et al., 2017), which show that quiescent clouds with reduced star formation have similar power-law features. Our results contradict the paradigm that clouds with little star formation have a lognormal PDF.

Furthermore, it is often debated whether a lognormal PDF is a direct imprint of supersonic turbulence alone, with column density PDFs becoming wider with increasing Mach number (Collins et al., 2012; Federrath & Klessen, 2013) and narrower with increasing magnetic field strength (Molina et al., 2012). However, only our fiducial model V4 (with both strong magnetic field and supersonic turbulence) mimics the results of these simulations (of magnetized clouds

with driven turbulence) where the PDF is predominantly lognormal with a power law at the high density end. The column density map of this model (Figure 2.5) is highly filamentary and oscillating due to the interplay between the magnetic and ram pressures of the large-scale flow, as described analytically by Auddy et al. (2016). The presence of a strong magnetic field acts like a physical spring against the turbulent compression, and causes a sequence of oscillations. This minimizes the decay of turbulence as most of the energy stays on the large scale for an extended time (resembling driven turbulence) resulting in a nearly lognormal PDF until gravitationally-driven ambipolar diffusion takes over. In all other models, the column density PDF develops a power law with a peak and turnover at lower values. These PDFs should not be classified as lognormal just because they have a peak. Indeed observations often show a pure power-law PDF for both star forming and diffuse clouds (Lombardi et al., 2014, 2015; Alves et al., 2017). One possible explanation (Ward et al., 2014) is that as the cloud evolves, the underlying lognormal shape may be lost. Our results strongly indicate that magnetic support in unison with turbulence and gravity play a crucial role in shaping the different observed PDFs.

A physical interpretation of these results requires understanding the fragmentation process in magnetically supported clouds. For example, in the model of Basu & Mouschovias (1994), the gravitational contraction of supercritical cores embedded in a subcritical envelope occurs in a very nonhomologous manner. The ultimately self-similar evolution results in supercritical cores having a central near uniform-column density surrounded by a radial power-law profile proportional to  $r^{-1}$  (Basu (1997); and see Equation A.1). This is the same as for hydrodynamic self-similar collapse (Larson, 1969; Shu, 1977; Hunter, 1977). However the convergence to this solution occurs only at innermost radii, while an intermediate region makes the transition from a magnetically supported envelope. Thus, the majority of the core area has a shallower column density profile, and at the boundary the profile of  $\Sigma$  is proportional to  $r^{-0.7}$  (see Figure 1 in Basu (1997)). As shown in Appendix (A.1), the radial column density profile with a power-law  $\Sigma \propto r^{-1}$  as in Equation (A.8) corresponds to a PDF  $\Sigma f(\Sigma) \propto \Sigma^{-2}$  but a profile  $\Sigma \propto r^{-0.5}$  for example will correspond to a PDF  $\Sigma f(\Sigma) \propto \Sigma^{-4}$  (Equation (A.9)). The delay in reaching the

self-similar collapse in the magnetically supported cloud, as opposed to a non-magnetically-supported cloud is the critical factor that makes the PDF steeper for a magnetically supported cloud. This is consistent with our high-resolution fiducial model V4, which develops a power-law tail with index  $\alpha = 2.4$  in the high column density end ( $\log \tilde{\Sigma} \geq 0.8$ ) as shown in Figure 2.9. The column density PDFs of our simulated models B3 and B8 with supercritical mass-to-flux ratio have a power-law tail with MLP fit parameter  $\alpha = 1.7$  and  $\alpha = 2.2$  respectively. This is also a direct imprint of the radial power-law profile ( $\Sigma \propto r^{-1}$ ) within the core. In contrast, the column density PDFs of the models V1 and K1 is much steeper with indices  $\alpha = 4.3$  and  $\alpha = 4.0$ , respectively. In both these models with initially small amplitude perturbations, the turbulent energy is confined to small scales, causing primarily local collapse due to gravitational contraction driven by ambipolar diffusion (see Figures 2.6 and 2.7). There is a slow transition towards a gravitationally collapsing supercritical inner core from an ambient magnetically dominated regions. Most of the gas is in a transition zone in which the radial column density profile is significantly shallower than  $\Sigma \propto r^{-1}$ , in fact closer to  $\Sigma \propto r^{-0.5}$ . These subcritical models can be directly identified with observations of Polaris and Pipe (Lombardi et al., 2015), which exhibit steeper power law with indices  $\alpha = 3.9$  and  $\alpha = 3.0$ , respectively.

## 2.4 Conclusion

We have presented a unified model of column density PDFs that accounts for lognormal plus power law PDFs in one limit and peaked power laws with different indices in other limits. We employed fully three-dimensional magnetohydrodynamical simulations with either supercritical or subcritical mass-to-flux ratio, and including ambipolar diffusion. We also studied different amplitudes and spectra of initially-supplied turbulence that is allowed to decay freely. Some of our key findings, including a comparison of clouds with strong and weak magnetic fields, are listed below.

- The column density PDFs for clouds with supercritical mass-to-flux ( $\beta_0 > 1$ ) ratio have

a power law with indices  $\alpha = 1.7$  and  $\alpha = 2.2$  for nonlinear and linear turbulence, respectively. These power laws develop quickly both in time as well as in column density evolution, so that the PDFs are like a pure power law except at the lowest values.

- Clouds with subcritical mass-to-flux ratio and linear perturbations (model V1) have a PDF that is a steep power law with index  $\alpha = 4.3$ . Similarly, for the subcritical model K1 with nonlinear white noise spectrum  $v_k^2 \propto k^0$ , the PDF is also steep with index  $\alpha = 4.0$ . The steep slope of these subcritical models (V1 and K1) is indicative of the process that magnetic support restricts the rate of core and star formation in these clouds. This is consistent with the fact that clouds with steeper slopes ( $\alpha = 3.9$  and  $\alpha = 3.0$ ), like Polaris and Pipe, respectively (Lombardi et al., 2015), have minimum star formation activity.
- The fitting of the column density PDF of supercritical clouds or subcritical clouds with linear perturbations is best done by a modified lognormal power law (MLP) function (Basu et al., 2015). The MLP is a pure lognormal in one limit and pure power law in another, depending on the values of its three parameters. The value of the parameter  $\alpha$  represents the slope of the power-law profile of all models studied here. The parameter  $\alpha$  has a typical variation of 10% – 20% depending on the different realizations of the initial perturbation and fitting routines.
- Only in the case of a subcritical (strong magnetic field) model V4 with nonlinear (supersonic) perturbations with turbulent spectrum  $v_k^2 \propto k^{-4}$  does the column density PDF retain a lognormal shape for the major part of its evolutionary phase as it oscillates due to the action of the magnetic field and turbulence. Eventually, the PDF develops a power-law tail due to gravitationally driven ambipolar diffusion, where the neutrals drift past the field lines and create subregions of supercritical pockets. In these subregions the PDF has an index  $\alpha \simeq 2$ , similar to supercritical clouds.
- A nonlinear velocity perturbation with turbulent spectrum  $v_k^2 \propto k^{-4}$  causes a much wider spread of the column density PDF in both supercritical and subcritical clouds compared

to clouds with linear perturbations. Furthermore, the strength of the strong velocity perturbation shortens the core formation time (Kudoh & Basu, 2011).

## **Acknowledgements**

We thank Deepakshi Madaan for fruitful discussions, and the anonymous referee for constructive comments. Computations were carried out using facilities of the Shared Hierarchical Academic Research Network (SHARCNET) and the Center for Computational Astrophysics, National Astronomical Observatory of Japan. SB is supported by a Discovery Grant from NSERC.

## Bibliography

Alves, J., Lombardi, M., & Lada, C. J. 2014, *A&A*, 565, A18

—. 2017, *A&A*, 606, L2

Alves, J. F., Lada, C. J., & Lada, E. A. 2001, *Nature*, 409, 159

Auddy, S., Basu, S., & Kudoh, T. 2016, *ApJ*, 831, 46

Bacmann, A., André, P., Puget, J.-L., et al. 2000, *A&A*, 361, 555

Ballesteros-Paredes, J., Vázquez-Semadeni, E., Gazol, A., et al. 2011, *MNRAS*, 416, 1436

Basu, S. 1997, *ApJ*, 485, 240

Basu, S., Ciolek, G. E., Dapp, W. B., & Wurster, J. 2009, *New A*, 14, 483

Basu, S., Gil, M., & Auddy, S. 2015, *MNRAS*, 449, 2413

Basu, S., & Mouschovias, T. C. 1994, *ApJ*, 432, 720

Ciolek, G. E., & Basu, S. 2006, *ApJ*, 652, 442

Clauset, A., Shalizi, C. R., & Newman, M. E. J. 2009, *SIAM Review*, 51, 661

Collins, D. C., Kritsuk, A. G., Padoan, P., et al. 2012, *ApJ*, 750, 13

Crutcher, R. M. 2012, *ARA&A*, 50, 29

Federrath, C., & Klessen, R. S. 2012, *ApJ*, 761, 156

—. 2013, *ApJ*, 763, 51

Federrath, C., Klessen, R. S., & Schmidt, W. 2008, *ApJ*, 688, L79

Hennebelle, P., & Chabrier, G. 2008, *ApJ*, 684, 395

—. 2011, *ApJ*, 743, L29

Hunter, C. 1977, *ApJ*, 218, 834

Johnson, N. L., Kotz, S., & Balakrishnan, N. 2002, *Continuous multivariate distributions, volume 1, models and applications*, Vol. 59 (New York: John Wiley & Sons)

Kainulainen, J., Beuther, H., Henning, T., & Plume, R. 2009, *A&A*, 508, L35

Könyves, V., André, P., Men'shchikov, A., et al. 2015, *A&A*, 584, A91

Kritsuk, A. G., Norman, M. L., & Wagner, R. 2011, *ApJ*, 727, L20

Kudoh, T., & Basu, S. 2003, *ApJ*, 595, 842

—. 2006, *ApJ*, 642, 270

—. 2008, *ApJ*, 679, L97

—. 2011, *ApJ*, 728, 123

—. 2014, *ApJ*, 794, 127

Kudoh, T., Basu, S., Ogata, Y., & Yabe, T. 2007, *MNRAS*, 380, 499

Langer, W. D. 1978, *ApJ*, 225, 95

Larson, R. B. 1969, *MNRAS*, 145, 271

Lombardi, M., Alves, J., & Lada, C. J. 2015, *A&A*, 576, L1

Lombardi, M., Bouy, H., Alves, J., & Lada, C. J. 2014, *A&A*, 566, A45

Mestel, L., & Spitzer, Jr., L. 1956, *MNRAS*, 116, 503

Molina, F. Z., Glover, S. C. O., Federrath, C., & Klessen, R. S. 2012, *MNRAS*, 423, 2680

Mouschovias, T. C., Ciolek, G. E., & Morton, S. A. 2011, *MNRAS*, 415, 1751

Mouschovias, T. C., & Spitzer, Jr., L. 1976, *ApJ*, 210, 326

- Nakamura, F., & Li, Z.-Y. 2005, *ApJ*, 631, 411
- Nakano, T., & Nakamura, T. 1978, *PASJ*, 30, 671
- Padoan, P., Jones, B. J. T., & Nordlund, Å. P. 1997, *ApJ*, 474, 730
- Padoan, P., & Nordlund, Å. 1999, *ApJ*, 526, 279
- . 2002, *ApJ*, 576, 870
- . 2011, *ApJ*, 730, 40
- Passot, T., & Vázquez-Semadeni, E. 1998, *Phys. Rev. E*, 58, 4501
- Pokhrel, R., Gutermuth, R., Ali, B., et al. 2016, *MNRAS*, 461, 22
- Scalo, J., Vázquez-Semadeni, E., Chappell, D., & Passot, T. 1998, *ApJ*, 504, 835
- Shu, F. H. 1977, *ApJ*, 214, 488
- Spitzer, Jr., L. 1942, *ApJ*, 95, 329
- Strittmatter, P. A. 1966, *MNRAS*, 132, 359
- Tafalla, M., Myers, P. C., Caselli, P., Walmsley, C. M., & Comito, C. 2002, *ApJ*, 569, 815
- Tassis, K., Christie, D. A., Urban, A., et al. 2010, *MNRAS*, 408, 1089
- Tomisaka, K., Ikeuchi, S., & Nakamura, T. 1988, *ApJ*, 335, 239
- Vazquez-Semadeni, E. 1994, *ApJ*, 423, 681
- Ward, R. L., Wadsley, J., & Sills, A. 2014, *MNRAS*, 445, 1575
- Ward-Thompson, D., Motte, F., & Andre, P. 1999, *MNRAS*, 305, 143



## Chapter 3

# A Magnetic Ribbon Model for Star-Forming Filaments

The *Herschel Space Observatory* has revealed a wide-ranging network of elongated (filamentary) structures in molecular clouds (e.g., André et al., 2010; Men'shchikov et al., 2010). Even though filamentary structures in molecular clouds were already well established (e.g., Schneider & Elmegreen, 1979), the Herschel continuum maps of dust emission at 70-500  $\mu\text{m}$  have achieved unprecedented sensitivity and revealed a deeper network of filaments, in both star-forming and non-star-forming molecular clouds. This implies that the filamentary network is an imprint of initial conditions, likely turbulence, rather than the result of pure gravitational instability. Furthermore, the prestellar cores and protostars, when present, are preferentially found along massive filaments.

Much interpretation of the filaments has been based on the assumption that they are isothermal cylinders. This simplifies their analysis as their observed shape is then independent of most viewing angles and one can rely on established theoretical results about the equilibrium or collapse of infinite cylinders. André et al. (2010) interpreted the observations in terms of the critical line mass of an isothermal cylinder  $m_{1,\text{crit}} = 2 c_s^2/G$ , where  $c_s$  is the isothermal sound speed. For a mass per unit length  $m > m_{1,\text{crit}}$ , a cylinder undergoes indefinite collapse as long as

the gas is isothermal, and for  $m < m_{1,\text{crit}}$  it can settle into an equilibrium structure, although still unstable to clumping along its length into Jeans length sized fragments (Larson, 1985). André et al. (2010) argue that star formation is initiated when  $m > m_{1,\text{crit}}$ .

A challenge to the view of filaments as cylinders is the magnetic field alignment inferred from polarized emission. Palmeirim et al. (2013) find that large scale magnetic fields are aligned perpendicular to the long axis of the massive star-forming filaments (see also Planck Collaboration et al., 2016). This makes a circular symmetry of a cylinder about the long axis unlikely unless the magnetic field strength is dynamically insignificant. A more natural configuration is a magnetic ribbon, a triaxial object that is flattened along the direction of the large-scale magnetic field with its shortest dimension in that direction. In the lateral direction to the magnetic field, elongated structures can form due to turbulence and gravity. Indeed, simulations of turbulence accelerated star formation in a strongly magnetic medium (Li & Nakamura, 2004; Nakamura & Li, 2005; Kudoh & Basu, 2008; Basu et al., 2009; Kudoh & Basu, 2011) show the formation of ribbon-like structure in a layer that is flattened along the magnetic field direction. Magnetic ribbons have recently been investigated theoretically by Tomisaka (2014) and Hanawa & Tomisaka (2015). They study magnetohydrostatic equilibria of ribbons that arise from a parent filament of radius  $R_0$ , which is a free parameter in the problem. They find that a critical line-mass-to-flux ratio exists for collapse, in analogy to the critical mass-to-flux ratio for axisymmetric three-dimensional objects (Mouschovias & Spitzer, 1976).

A further challenge to filaments modeled as isothermal cylinders comes from the dust emission measurement of the FWHM of the mean column density profile relative to the axis of a filament (Arzoumanian et al., 2011). For example, figure 7 of Arzoumanian et al. (2011) shows that the FWHM values for 90 filamentary structures in low mass star forming regions cluster around a mean of  $\sim 0.1$  pc with some scatter over two orders of magnitude range of mean column density<sup>1</sup>. However, Ostriker (1964) showed that the central half-mass radius of an equilibrium isothermal cylinder is  $a \propto c_s / \sqrt{G\rho_c}$ , essentially the Jeans length, where  $\rho_c$  is the

---

<sup>1</sup>Molecular line emission studies of the Taurus region show wider mean thicknesses  $\sim 0.4$  pc for filaments in velocity-integrated emission and  $\sim 0.2$  pc for filaments in individual velocity channels (Panopoulou et al., 2014)

central density. The projected column density of such a circularly symmetric configuration has a central flat region of size  $a$  and column density  $\Sigma_c = 2\rho_c a$  (see Dapp & Basu, 2009), so that we can also write  $a \propto c_s^2/(G\Sigma_c)$ . Therefore, the approximate observed relation  $a \simeq \text{constant}$  is unlike the expected  $a \propto \Sigma_c^{-1}$ . However, the observed set of values of the FWHM radii also intersect the line of Jeans length at the median log column density, which implies that the Jeans length may not be wholly unrelated to them.

In this paper, we explore the consequences of a magnetic ribbon model for molecular cloud filaments for the measured relation between apparent width and the observed column density. We argue that this is a more natural model for filaments and is based on the interplay between turbulence, strong magnetic fields, and gravitationally-driven ambipolar diffusion, rather than pure gravity and thermal pressure. We extend the analytic model of Kudoh & Basu (2014) for the formation of magnetic ribbons that is based on numerical simulations. We derive a lateral width of a magnetic ribbon and use it to calculate a synthetic observed relation between apparent width in projection versus observed column density.

## 3.1 Semi-Analytic Model

### 3.1.1 Background

Dynamically important magnetic fields, corresponding to mass-to-flux ratios that range from subcritical to mildly supercritical, will lead to flattening along the magnetic field direction, and subsequent evolution will be primarily perpendicular to the magnetic field (Fiedler & Mouschovias, 1993; Nakamura & Li, 2008). Even highly turbulent three-dimensional simulations (Kim & Basu, 2013) show that the turbulence is eventually dominated by motions perpendicular to the ambient magnetic field. Observations of some filaments (e.g., Palmeirim et al., 2013) that show a large-scale magnetic field along the short dimension of the filament also support the idea of flattening along the field. In this paper, we adopt the scenario of turbulent compression acting primarily perpendicular to the magnetic field direction in an initially

subcritical molecular cloud. This leads to the paradigm of turbulence accelerated star formation, in which star formation occurs with globally low efficiency and in turbulent compressed regions. These regions oscillate about an approximate force-balanced state until ambipolar diffusion creates supercritical pockets that collapse to form stars. We explore the consequences of this scenario by extending a semi-analytic model of Kudoh & Basu (2014) that is based on numerical simulations.

### 3.1.2 Ribbon Width

We consider local pressure balance of a compressed region in a subcritical cloud and neglect thermal pressure in comparison to magnetic pressure and the ram pressure of the flow. We assume that the cloud is stratified in the  $z$ -direction, with compression happening primarily in the  $x$ - $y$  plane. Here we simplify the analysis of the compression by limiting it to one direction, the  $x$ -axis (Fig. 3.1), as done by Kudoh & Basu (2014). The initial magnetic field strength is  $B_0$  and the field strength increases upon compression until the magnetic pressure within the compressed ribbon balances the external ram pressure and magnetic pressure. Hence the compression ends (and oscillations may ensue) when

$$H \frac{B^2}{8\pi} = H_0 \left( \rho_0 v_{t0}^2 + \frac{B_0^2}{8\pi} \right), \quad (3.1)$$

where  $v_{t0}$  is the nonlinear flow speed. Assuming that the gas has adequate time to settle into hydrostatic equilibrium along the  $z$ -direction, the half thickness of the cloud is

$$H = \frac{c_s}{\sqrt{2\pi G\rho}} \quad (3.2)$$

(Spitzer, 1942). Now if the ambipolar diffusion time is longer than the compression time (Kudoh & Basu, 2014), flux freezing is valid during compression, i.e.,

$$\frac{B}{\Sigma} = \frac{B_0}{\Sigma_0}. \quad (3.3)$$

For the surface density  $\Sigma = 2\rho H$ , equation (3.3) can be rewritten as

$$\frac{B}{\rho^{\frac{1}{2}}} = \frac{B_0}{\rho_0^{\frac{1}{2}}}. \quad (3.4)$$

Using equation (3.2) and equation (3.4) in equation (3.1) and with some simplifications we get

$$\left(\frac{\rho}{\rho_0}\right)^{1/2} = 2\left(\frac{v_{t0}}{v_{A0}}\right)^2 + 1, \quad (3.5)$$

where  $v_{A0}^2 = B_0^2/(4\pi\rho_0)$  is the square of the initial Alfvén speed of the cloud. The consequence of such compression results in the formation of magnetic ribbons of width  $L$  and thickness  $2H$ , as they are flattened along the direction of magnetic field (see Fig. 3.1). For conservation of mass per unit length in the ribbon during the compression of the cloud

$$\rho_0 L_0 H_0 = \rho L H, \quad (3.6)$$

where  $L_0$  is the initial width (along the  $x$ -axis) and  $2H_0$  is the initial thickness of the cloud in the vertical direction ( $z$ -axis). Using equation (3.2), we can simplify the above equation to

$$\left(\frac{\rho}{\rho_0}\right)^{1/2} = \frac{L_0}{L}. \quad (3.7)$$

By using equation (3.7) in equation (3.5), we can express the final width of the filament as

$$L = L_0 \left[ 2\left(\frac{v_{t0}}{v_{A0}}\right)^2 + 1 \right]^{-1}. \quad (3.8)$$

Analysis of Zeeman measurements of the magnetic field in molecular clouds presented by Crutcher (1999) shows that the turbulent line width is comparable to the Alfvén speed (Basu, 2000). If we make the plausible estimate that the flow speed is comparable to the Alfvén speed,

i.e.,  $v_{t0} \simeq v_{A0}$ , the filament width becomes

$$L \simeq L_0/3. \quad (3.9)$$

The result illustrates the fact that the final width of a filament is *independent* of the density of the medium. Instead it is a fraction of the initial length scale  $L_0$  of the compressed region.

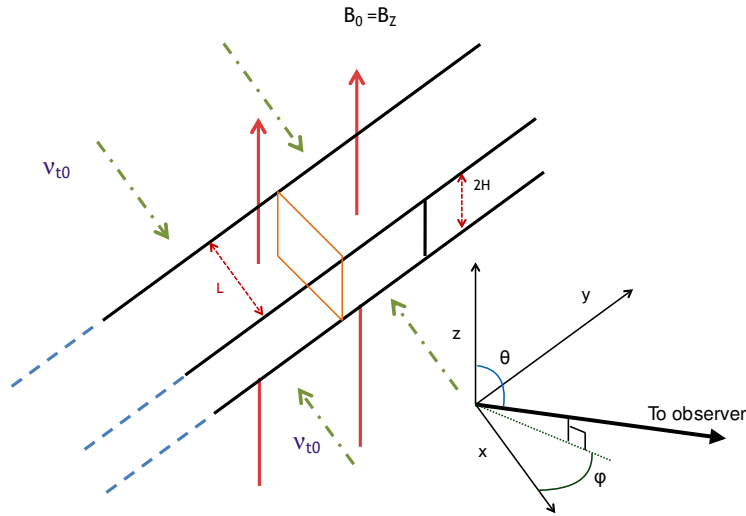


Figure 3.1: The formation of a magnetic ribbon as the molecular cloud contracts under the influence of the “ram pressure” and the perpendicular magnetic field. The thick black arrow points to an observer located at a random orientation in the sky.

### 3.1.3 Initial Compression Scale

In the above theory, the final ribbon width  $L$  is independent of its density, but does depend on the initial compression scale  $L_0$  associated with turbulence. The origin and physics of  $L$  is then quite different than that of the Jeans length. What is  $L_0$  then? In the turbulent scenario that we adopt in this study, it would be associated with the dominant mode in the turbulent flow field in a molecular cloud. At this point, no first principles theory exists to calculate  $L_0$  as the preferred mode of an instability that leads to molecular cloud turbulence. Hence, we take guidance from observations to make an empirical estimate for  $L_0$ .

### Estimate from column density map

The column density maps used by Arzoumanian et al. (2011) to determine the mean filament width can also be used to estimate a mean spacing between filaments, which we identify with  $L_0$  in our model. Figure 3b of Arzoumanian et al. (2011) identifies 27 filaments in a dust emission map of the cloud IC 5146. We use this same map to make an approximate measurement of  $L_0$ . For each of the 27 filaments, we identify a center along the length (spine) of the filament. Then for each filament we measure the distance to the nearest center point of another filament. We obtain a set of 20 unique distance measurements (eliminating double counting in cases where two filaments are mutually each other's nearest neighbor). We ignore effects of an inclination angle  $i$  in this analysis, which could mean that the measured distances are less than the actual distances by a factor  $\sin i$ . Our measured filament spacings (which we equate with  $L_0$ ) have a minimum value 0.5 pc, a maximum value 2.2 pc, a median value 0.9 pc, and a mean value 1.0 pc.

### Estimate from star formation timescale

Another way to constrain  $L_0$  is through the star formation timescale in molecular clouds. Since this number is widely accepted to be in the range 1-3 Myr (Palla & Stahler, 2000, 2002; Hartmann, 2001), and star formation is often coordinated along a filament over this timescale, we can place an upper limit (again empirically) on the compression timescale  $t_0$  of a few Myr. Therefore the initial length scale that can trigger a compression can be written as

$$L_0 \simeq v_{t0} t_0 \simeq v_{A0} t_0, \quad (3.10)$$

where  $t_0$  is as above and again using the Alfvénic nature of turbulence. This further simplifies to

$$L_0 \simeq \frac{B_0}{\sqrt{4\pi\rho_0}} t_0 = \frac{\sqrt{2}}{\mu_0} c_s t_0, \quad (3.11)$$

where we have used pressure balance along the magnetic field,  $\pi G \Sigma_0^2 / 2 = \rho_0 c_s^2$  and the normalized mass-to-flux ratio  $\mu_0 = \Sigma_0 (2\pi \sqrt{G}) / B_0$ . If we consider the initial cloud to be mildly subcritical, i.e.,  $\mu_0 \approx 0.5$ , and a sound speed  $c_s = 0.2 \text{ km s}^{-1} \approx 0.2 \text{ pc Myr}^{-1}$ , then  $t_0 \approx 1 - 3 \text{ Myr}$  leads to  $L_0 \approx 1 \text{ pc}$ .

## 3.2 Results

The simple arguments of the previous section show that the length scale at which the ribbon formation is initiated is of the order of a parsec. Our semi-analytic model then implies that the final width of the ribbon given by equation (3.9) is  $\sim 0.3 \text{ pc}$ . However, the shortest dimension is flattened along the direction of the magnetic field and has a thickness  $2H$  that *does* depend on the column density. Therefore, the observed shape will depend on the viewing angle. Below we calculate the observed width for a particular viewing angle and then calculate a synthetic plot of observed ribbon width versus observed column density for a collection of random viewing angles. Our objective is to gain insight into the form of the observed correlation, and how it compares with the standard Jeans length scaling and with the observational results presented by Arzoumanian et al. (2011). The value of  $L_0$  can be considered a free parameter and physically may vary from one cloud to another and have a distribution of values within a single cloud. While we do not advocate a specific individual value for  $L_0$ , we use the empirical estimate that it should be  $\sim 1 \text{ pc}$  to determine the shape and approximate quantitative values of an observed correlation.

### 3.2.1 Observed Width

Let the normal to the filament, along the  $z$ -axis, be inclined at an angle  $\theta$  to the observer as shown in Fig. 3.2. For a ribbon-like filament of intrinsic width  $L$  and half thickness  $H$  the



projected width  $L_{\text{obs}}$  as seen by the observer is

$$L_{\text{obs}} = L \cos \theta + 2H \sin \theta. \quad (3.12)$$

If the ribbon is viewed face on, i.e.,  $\theta = 0^\circ$ , the observed width is just the intrinsic width  $L$ . When viewed side on i.e.,  $\theta = 90^\circ$  the observed width is the thickness  $2H$  of the ribbon along the  $z$  axis. For any other intermediate angles one sees the projection in the  $y$ - $z$  plane i.e., equation (3.12), as shown in Fig. 3.2.

From our analysis we have already shown in equation (3.9) that the intrinsic width  $L$  is a fraction of the initial compression length scale  $L_0$ .

The thickness  $2H$  of the magnetic ribbon is evaluated using the hydrostatic equilibrium, equation (3.2), along the direction of the magnetic field (i.e., perpendicular to the filament width). For column density  $\Sigma = 2\rho H$ , the half-thickness of the clouds is estimated to be

$$H = \frac{c_s^2}{\pi G \Sigma}. \quad (3.13)$$

For a ribbon of any particular column density  $\Sigma$  we can estimate the corresponding half-thickness  $H$ , which is essentially the Jeans scale, using equation (3.13). For example,  $H = 0.16$  pc for  $c_s = 0.2 \text{ km s}^{-1}$  and  $N \equiv \Sigma/m = 10^{21} \text{ cm}^{-2}$  in which  $m = 2.3 m_{\text{H}}$ .

### 3.2.2 Observed Column Density

The observed column density  $\Sigma_{\text{obs}}$  will be different from the intrinsic column density  $\Sigma$  depending on the angle at which the ribbon is being viewed. If the observer is situated at angle other than  $\theta = \phi = 0^\circ$  (as shown in Fig. 3.1), the length along the line of sight changes thus affecting the observed column density. In the following section we will analyze the variation of  $\Sigma_{\text{obs}}$  with the viewing angles  $\theta$  and  $\phi$ . We neglect the variation of  $\rho$  within the ribbon.

**Case 1** ( $0^\circ \leq \theta \leq \theta_{\text{crit}}$ )

For the beam incident on the face of the ribbon at an angle  $0^\circ \leq \theta \leq \theta_{\text{crit}}$  and  $\phi = 0^\circ$ , (refer to Fig. 3.2a,) the observed column density is

$$\Sigma_{\text{obs}} = 2\rho H \sec \theta. \quad (3.14)$$

Since the intrinsic column density  $\Sigma = 2\rho H$ , we get

$$\Sigma_{\text{obs}} = \Sigma \sec \theta. \quad (3.15)$$

Thus only for  $\theta = 0^\circ$ , i.e., when the ribbon is viewed face on,  $\Sigma_{\text{obs}} = \Sigma$ . For  $0^\circ < \theta \leq \theta_{\text{crit}}$ ,  $\Sigma_{\text{obs}} > \Sigma$ .

**Case 2** ( $\theta = \theta_{\text{crit}}$ )

For the beam entering at a critical angle  $\theta_{\text{crit}}$  and  $\phi = 0^\circ$  (Fig. 3.2b), the observed column density is

$$\Sigma_{\text{obs}} = 2\rho H \sec \theta_{\text{crit}} = \rho L \csc \theta_{\text{crit}}. \quad (3.16)$$

Rearranging the above equation, we find that

$$\theta_{\text{crit}} = \tan^{-1} \frac{L}{2H}. \quad (3.17)$$

The critical angle  $\theta_{\text{crit}}$  separates the two sets of angles that have separate expressions for  $\Sigma_{\text{obs}}$ .

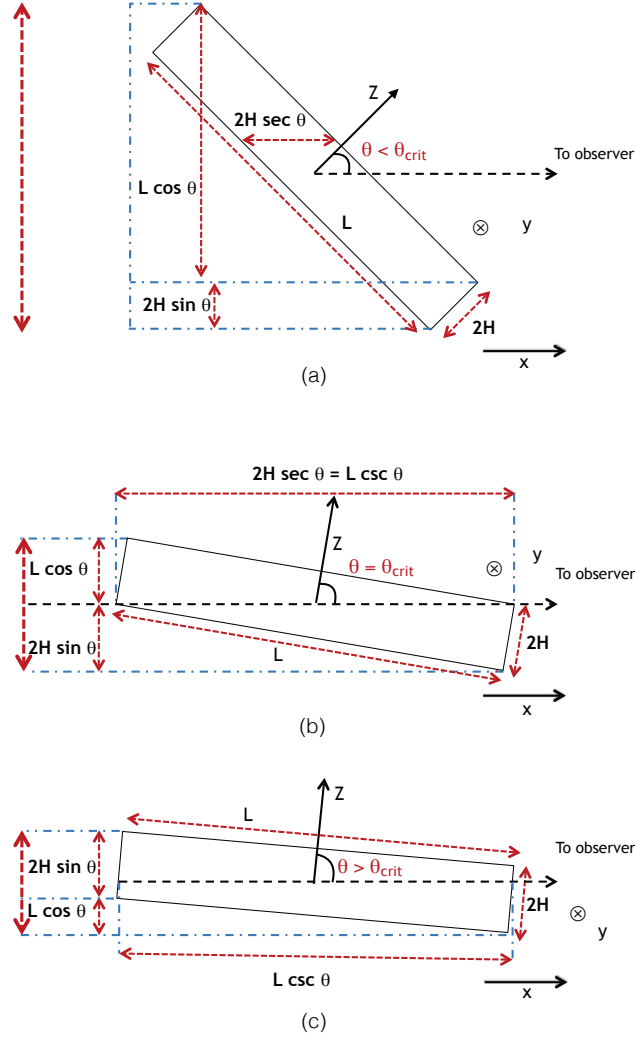


Figure 3.2: Different orientations of the magnetic ribbon with respect to the observer. Top panel: case 1 ( $0^\circ \leq \theta \leq \theta_{\text{crit}}$ ). Middle panel: case 2 ( $\theta = \theta_{\text{crit}}$ ) when the ribbon is observed at a critical angle as shown. Bottom panel: case 3 ( $\theta_{\text{crit}} \leq \theta \leq 90^\circ$ ).

### Case 3 ( $\theta_{\text{crit}} \leq \theta \leq 90^\circ$ )

For the beam entering through the shorter dimension of the ribbon (see Fig. 3.2c) at an angle  $\theta_{\text{crit}} \leq \theta \leq 90^\circ$  and  $\phi = 0^\circ$ , the observed column density is

$$\Sigma_{\text{obs}} = \rho L \csc \theta. \quad (3.18)$$

Using equation (3.2), and  $\Sigma = 2\rho H$ , we get

$$\Sigma_{\text{obs}} = \frac{\Sigma L}{2H \sin \theta} = \frac{\pi G \Sigma^2 L}{2c_s^2 \sin \theta}. \quad (3.19)$$

For  $\theta = 90^\circ$ , i.e., when the ribbon is viewed side on,  $\Sigma_{\text{obs}} = \Sigma \frac{L}{2H}$ . For  $\theta_{\text{crit}} < \theta \leq 90^\circ$ ,  $\Sigma_{\text{obs}} > \Sigma$  if  $L > 2H$ , i.e., when the ribbon width is greater than the thickness of the ribbon, the observed column density is greater than the actual column density.

#### Case 4 ( $\phi \neq 0^\circ$ )

Furthermore, different angular orientation of the magnetic ribbons in the  $x$ - $y$  plane will also alter the observed column density. If the long axis ( $y$ ) of the ribbon is not perpendicular the line of sight (see Fig. 3.1), i.e.,  $\phi \neq 0^\circ$  the observed column density will further increase. For any random orientation in the  $x$ - $y$  plane, the modified column density is

$$\Sigma_{\text{obs}} = \Sigma \sec \theta \sec \phi, \quad 0^\circ \leq \theta \leq \theta_{\text{crit}}, \quad (3.20)$$

$$\Sigma_{\text{obs}} = \frac{\pi G \Sigma^2 L}{2c_s^2 \sin \theta} \sec \phi, \quad \theta_{\text{crit}} \leq \theta \leq 90^\circ. \quad (3.21)$$

However, different orientations in the  $x$ - $y$  plane do not affect the observed ribbon width. The resultant projection of the ribbon width on the  $y$ - $z$  plane is independent of the azimuthal angle  $\phi$ .

### 3.2.3 Observed Correlation

Since the observations of Arzoumanian et al. (2011) reveal a relatively flat relation between observed width and column density, it is instructive to use our model to make a synthetic map of these quantities. For simplicity we consider  $\phi = 0$  in this analysis. We take a sample of 100 ribbons with number column density distributed uniformly in the range  $10^{21} \text{ cm}^{-2} \leq N \leq 10^{23} \text{ cm}^{-2}$ . Furthermore we take viewing angles randomly chosen in the range  $0^\circ \leq \theta \leq 90^\circ$ . Each pair of values  $(N, \theta)$  yields a pair of values  $(N_{\text{obs}}, L_{\text{obs}})$  represented as blue dots in Fig.

3.3. We obtain  $L_{\text{obs}}$  using equation (3.12) and  $\Sigma_{\text{obs}}$  using equation (3.15) or equation (3.19) for  $\theta \leq \theta_{\text{crit}}$  or  $\theta > \theta_{\text{crit}}$ , respectively. The black dashed line in Fig. 3.3 is the locus of points obtained by taking 100 randomly chosen values of  $\theta$  for each value of  $N$  and calculating the mean values of  $L_{\text{obs}}$  and  $N_{\text{obs}}$ . This line is similar to the result of taking equation (3.12) and inserting the mean values of  $\cos \theta$  and  $\sin \theta$ , which are both equal to  $2/\pi$ , and replacing  $\Sigma$  with the mean value of  $\Sigma_{\text{obs}}$ . However, the mean value of  $\Sigma_{\text{obs}}$  across all angles is not exactly equal to  $\Sigma$ . Both the set of individual synthetic data points shown in blue dots as well as the average relation in the black dashed line show a relatively flat relation over two orders of magnitude variation in  $N_{\text{obs}}$ . Fig. 3.3 also shows the analytic relation for two limiting cases. The black dotted line corresponds to the face on view ( $\theta = 0^\circ$ ) where  $L_{\text{obs}} = L = 0.3$  pc and is independent of the column density. The blue dot-dashed line corresponds to  $\theta = 90^\circ$  where  $L_{\text{obs}} = 2c_s^2/(\pi G \Sigma)$ , essentially the Jeans length.

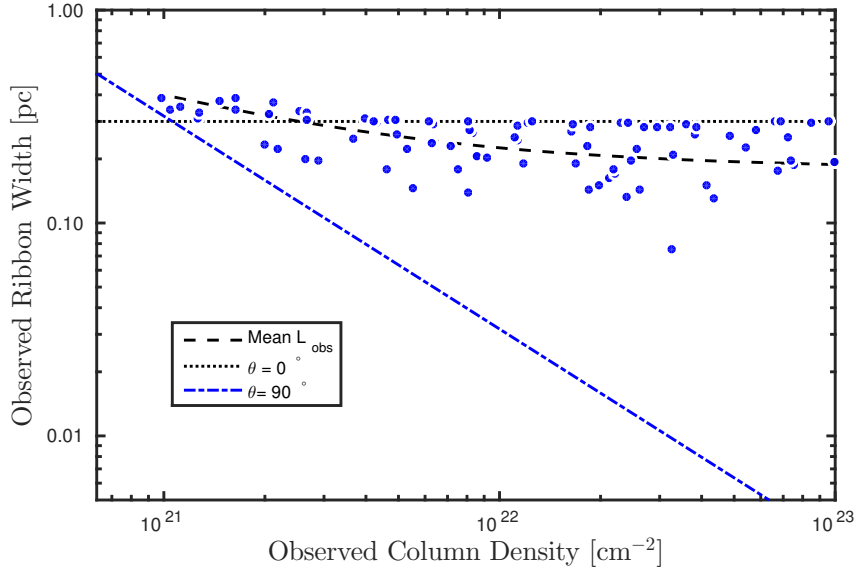


Figure 3.3: Apparent ribbon width  $L_{\text{obs}}$  versus observed column density  $N_{\text{obs}}$ . Each blue dot corresponds to a magnetic ribbon with intrinsic column density  $N$  and observing angle  $\theta$ , chosen as described in Sec. 3.2.3. The black dashed line is the mean ribbon width for the entire range of values of  $N_{\text{obs}}$ . The black dotted line is the width when the ribbon is viewed at  $\theta = 0^\circ$ . The blue dot-dashed line is the width for the side on view i.e.,  $\theta = 90^\circ$ .

### 3.3 Conclusion

We have presented a minimum hypothesis model for the width of a filament in a molecular cloud in which magnetic fields and magnetohydrodynamic turbulence are initially dominant. A turbulent compression leads to a magnetic ribbon whose thickness is set by the standoff between ram pressure and magnetic pressure region. Gravitationally-driven ambipolar diffusion then leads to runaway collapse of the densest regions in the ribbon, where the mass-to-flux ratio has become supercritical. This process has been demonstrated in published simulations of trans-Alfvénic turbulence in a cloud with an initial subcritical mass-to-flux ratio (e.g., Nakamura & Li, 2005; Kudoh & Basu, 2011). We have extended the semi-analytic model of Kudoh & Basu (2014) to estimate their lateral (perpendicular to magnetic field and ribbon long axis) width. This quantity is independent of the density of the ribbon. This lateral width can also be used to estimate the parent filament radius  $R_0$  in the theoretical magnetic ribbon model of Tomisaka (2014). In our model, the thickness parallel to the magnetic field is essentially the Jeans scale and does depend on density. Hence, we calculate a distribution of apparent widths seen in projection assuming a random set of viewing angles. The resulting distribution of apparent widths versus apparent column density is relatively flat (unlike expectations based on the Jeans length) over the range  $10^{21} \text{ cm}^{-2} - 10^{23} \text{ cm}^{-2}$ , in rough agreement with the observations of Arzoumanian et al. (2011). Other models have been introduced to explain the apparent near-uniform width of observed filaments. Fischera & Martin (2012) introduce an external pressure to an isothermal cylinder and find that the FWHM versus column density is a peaked function and approximately flat in the regime where  $m_1$  is well below  $m_{1,\text{crit}}$  and the external pressure is comparable to the central pressure. However, filaments with  $m_1 > m_{1,\text{crit}}$  would be in a time-dependent state of dynamical collapse. Hennebelle & André (2013) develop a model of a cylindrical self-gravitating filament that is accreting at a prescribed rate. A near-uniform radius is derived based on assumption of a steady-state balance between energy input from accretion and dissipation of energy by ion-neutral friction at the filament radius scale. Heitsch (2013) also develops a model of accretion at the free-fall rate onto a filament with  $m_1 < m_{1,\text{crit}}$

and uses various prescribed forms of internal structure to find that the FWHM has a peaked dependence on column density. A series of simulation papers (Smith et al., 2014; Kirk et al., 2015; Federrath, 2016) use hydrodynamic or MHD simulations (with supercritical mass-to-flux ratio) and analyze filament widths at particular snapshots in time. Although their filament widths cluster at  $\sim 0.1$  pc with some scatter, there is a mild to strong density dependence of the widths, and the filaments are single time snapshots in a situation of continuing collapse. Federrath (2016) suggests that  $\sim 0.1$  pc is special since the linewidth-size relation of Larson (1981) would lead to subsonic turbulence below that scale, but it is not clear if his simulations satisfy this scaling internally. We believe that the magnetic ribbon model provides an alternative simplified interpretation that accounts for turbulence and strong magnetic fields. We have developed a method to estimate the width of a magnetic ribbon based on the characteristic scale and amplitude of MHD turbulence. Such ribbons can have a line mass that exceeds the hydrodynamic limit  $2c_s^2/G$  and still be in a dynamically oscillating quasi-equilibrium state. However, gravity still leads to star formation in the dense interior through rapid ambipolar diffusion.

## Acknowledgements

We thank the anonymous referee for comments that improved the discussion in this paper. This work was supported by a Discovery Grant from NSERC.

## Bibliography

André, P., Men'shchikov, A., Bontemps, S., et al. 2010, *A&A*, 518, L102

Arzoumanian, D., André, P., Didelon, P., et al. 2011, *A&A*, 529, L6

Basu, S. 2000, *ApJ*, 540, L103

Basu, S., Ciolek, G. E., Dapp, W. B., & Wurster, J. 2009, *New A*, 14, 483

Crutcher, R. M. 1999, *ApJ*, 520, 706

Dapp, W. B., & Basu, S. 2009, *MNRAS*, 395, 1092

Federrath, C. 2016, *MNRAS*, 457, 375

Fiedler, R. A., & Mouschovias, T. C. 1993, *ApJ*, 415, 680

Fischera, J., & Martin, P. G. 2012, *A&A*, 542, A77

Hanawa, T., & Tomisaka, K. 2015, *ApJ*, 801, 11

Hartmann, L. 2001, *AJ*, 121, 1030

Heitsch, F. 2013, *ApJ*, 769, 115

Hennebelle, P., & André, P. 2013, *A&A*, 560, A68

Kim, C.-G., & Basu, S. 2013, *ApJ*, 778, 88

Kirk, H., Klassen, M., Pudritz, R., & Pillsworth, S. 2015, *ApJ*, 802, 75

Kudoh, T., & Basu, S. 2008, *ApJ*, 679, L97

—. 2011, *ApJ*, 728, 123

—. 2014, *ApJ*, 794, 127

Larson, R. B. 1981, *MNRAS*, 194, 809



—. 1985, MNRAS, 214, 379

Li, Z.-Y., & Nakamura, F. 2004, ApJ, 609, L83

Men'shchikov, A., André, P., Didelon, P., et al. 2010, A&A, 518, L103

Mouschovias, T. C., & Spitzer, Jr., L. 1976, ApJ, 210, 326

Nakamura, F., & Li, Z.-Y. 2005, ApJ, 631, 411

—. 2008, ApJ, 687, 354

Ostriker, J. 1964, ApJ, 140, 1056

Palla, F., & Stahler, S. W. 2000, ApJ, 540, 255

—. 2002, ApJ, 581, 1194

Palmeirim, P., André, P., Kirk, J., et al. 2013, A&A, 550, A38

Panopoulou, G. V., Tassis, K., Goldsmith, P. F., & Heyer, M. H. 2014, MNRAS, 444, 2507

Planck Collaboration, Ade, P. A. R., Aghanim, N., et al. 2016, A&A, 586, A138

Schneider, S., & Elmegreen, B. G. 1979, ApJS, 41, 87

Smith, R. J., Glover, S. C. O., & Klessen, R. S. 2014, MNRAS, 445, 2900

Spitzer, Jr., L. 1942, ApJ, 95, 329

Tomisaka, K. 2014, ApJ, 785, 24

# Chapter 4

## Magnetic Field Structure of Dense Cores using Spectroscopic Methods

### 4.1 Introduction

Stars form in dense cores embedded within interstellar molecular clouds (Lada et al., 1993; Williams et al., 2000; André et al., 2009). Dense cores are well studied observationally from molecular spectral line emission (Myers & Benson, 1983; Benson & Myers, 1989; Jijina et al., 1999), infrared absorption (Teixeira et al., 2005; Lada et al., 2007; Machaieie et al., 2017) and submillimeter dust emission (Ward-Thompson et al., 1994; Kirk et al., 2005; Marsh et al., 2016).

Cores form in multiple ways due to fragmentation of over-dense regions (typically filaments and sheets (Basu et al., 2009)) within turbulent magnetized clouds. Depending on the ambient initial conditions they can form either as a result of spontaneous gravitational contraction (Jeans instability Jeans (1929); Larson (1985, 2003)) or by rapid fragmentation due to preexisting turbulence (Padoan et al., 1997; Klessen, 2001; Gammie et al., 2003). The other classical scenario is the formation of cores in magnetically supported clouds due to quasistatic ambipolar diffusion i.e., gravitationally induced drift of the neutral species with respect to ions (Mestel

& Spitzer, 1956; Mouschovias, 1979; Shu et al., 1987)). However, a more recent view is that both supersonic turbulence and gravitationally driven ambipolar diffusion are significant in the process of core formation (e.g., Nakamura & Li (2005); Kudoh & Basu (2011, 2014); Chen & Ostriker (2014); Auddy et al. (2018)).

To get a vivid picture we investigate the kinematics of some of the dense cores in Ophiuchus. Dense cores are the seeds for star formation and often have nonthermal contributions to linewidth that are small compared to the thermal values (Rydbeck et al., 1977; Myers, 1983; Caselli et al., 2002). These observations imply a transition from a primarily nonthermal linewidth in low density molecular cloud envelopes to a nearly thermal linewidth within dense cores. This is termed as “a transition to velocity coherence” (Goodman et al., 1998). A sharp transition between the coherent core and the dense turbulent gas surrounding the B5 region in Perseus was found using  $\text{NH}_3$  observations from the Green Bank Telescope (GBT) by Pineda et al. (2010). An important question is whether a transition from magnetic support of low density regions to gravitational collapse of dense regions is physically related to the transition to coherence. Furthermore, how is the magnetic field strength affecting the nonthermal linewidth in the low density region, and is this related to the velocity transition? If so, can one estimate the magnetic field strength and its radial variation across a dense core using such observations?

Accurate measurement of the magnetic field is one of the challenges of observational astrophysics. Several methods exist that probe the magnetic field in the interstellar medium, such as Zeeman detection (e.g., Crutcher (1999)), dust polarization (Hoang & Lazarian, 2008) and Faraday rotation (Wolleben & Reich, 2004). While each method has its own limitations (Crutcher, 2012), sensitive observations of dust polarization often provide a good characterization of the plane-of-sky magnetic field. According to the dust alignment theory (Andersson et al., 2015), the elongated interstellar dust grains tend to align with their minor axis parallel to the magnetic field. Dust polarization observations from thermal emission or extinction of background star light provide a unique way to probe the magnetic field morphology in the ISM,

including collapsing cores in molecular clouds. However, in addition to getting the field morphology, there are various methods to estimate the magnetic field strength. One of the popular technique is the Chandrasekhar-Fermi (CF) method (Davis & Greenstein, 1951; Chandrasekhar & Fermi, 1953) that estimates the field strength using measurements of the field dispersion (about the mean field direction), gas density, and one-dimensional nonthermal velocity dispersion. Dust polarization, however, can be weak in the centers of dense cores where the dust grains are well shielded from the radiative torques necessary to move the grains into alignment with the magnetic field (e.g., see Lazarian & Hoang (2007)). Accurate detection of magnetic field strength and morphology is key to resolving the long standing debate about whether magnetic support (Mouschovias, 1991) or turbulent motions (Padoan & Nordlund, 1999) dominate, or if both processes are crucial in regulating star formation in molecular clouds (Nakamura & Li, 2005; Kudoh & Basu, 2011; Vazquez-Semadeni et al., 2011).

In this paper we present new  $\text{NH}_3$  observations of multiple cores in the L1688 region in the Ophiuchus molecular cloud. Most of the cores show a sharp transition to coherence with a nearly subsonic nonthermal velocity dispersion in the inner region. Here we propose a new “Core Field Structure” (CFS) method of estimating the amplitude of magnetic field fluctuations. It incorporates detailed maps from the Green Bank Ammonia Survey (GAS) of the nonthermal linewidth profiles across a core. We use this method to estimate the magnetic field profile of some of the dense cores in the Ophiuchus molecular cloud. The paper is organized in the following manner. The observations of the gas kinematics and the column density are reported in Section 2. In Section 3 we introduce the new CFS model and the inferred magnetic field profile. In Section 4 we discuss the limitations of the model. We highlight some of the important conclusions in Section 5.

## 4.2 Observations

The first data release paper from the GBT survey (Friesen et al., 2017) included detailed  $\text{NH}_3$  maps of the gas kinematics (velocity dispersion,  $\sigma_v$  and gas kinetic temperature,  $T_K$ ) of four regions in the Gould Belt: B18 in Taurus, NGC 1333 in Perseus, L1688 in Ophiuchus, and Orion A North in Orion. The emission from the  $\text{NH}_3$  ( $J, K$ ) = (1, 1) and (2, 2) inversion lines in the L1688 region of the Ophiuchus cores were obtained using the 100 m Green Bank Telescope. The observations were done using in-band frequency switching with a frequency throw of 4.11 MHz, using the GBT K-band (upper) receiver and the GBT spectrometer at the front and back end, respectively. L1688 is located centrally in the Ophiuchus molecular cloud. It is a concentrated dense hub (with numerous dense gas cores) spanning approximately 1 – 2 pc in radius with a mass of  $2 \times 10^3 M_\odot$  (Loren, 1989). L1688 has over 300 young stellar objects (Wilking et al., 2008) and contains regions of high visual extinction, with  $A_V \sim 50 - 100$  mag (e.g., Wilking & Lada (1983)). The mean gas number density of L1688 is approximately a few  $\times 10^3 \text{cm}^{-3}$ . Submillimeter continuum emission from dust shows that the star formation efficiency of the dense gas cores is  $\approx 14\%$  (Jørgensen et al., 2008).

### 4.2.1 Velocity Dispersion

Figure 6 in Friesen et al. (2017) shows the integrated intensity map of the  $\text{NH}_3(1, 1)$  line for the L1688 region in Ophiuchus. The ammonia map of L1688 in Ophiuchus includes four prominent isolated starless cores (including H-MM1) lying on the outskirts of the cloud, plus more than a dozen local linewidth minima in the main cloud (mainly in the south-eastern part in regions called Oph-C, E, and F). Many of these minima correspond to roundish starless cores that can be identified on the SCUBA-2 850 micron dust continuum map. The velocity dispersions and the kinetic temperatures are calculated from the averaged  $\text{NH}_3(1, 1)$  and  $\text{NH}_3(2, 2)$  spectra. We have averaged the spectra in concentric annuli to follow the change of nonthermal velocity dispersion as a function of the distance from the core center. Figure 4.1 shows radially

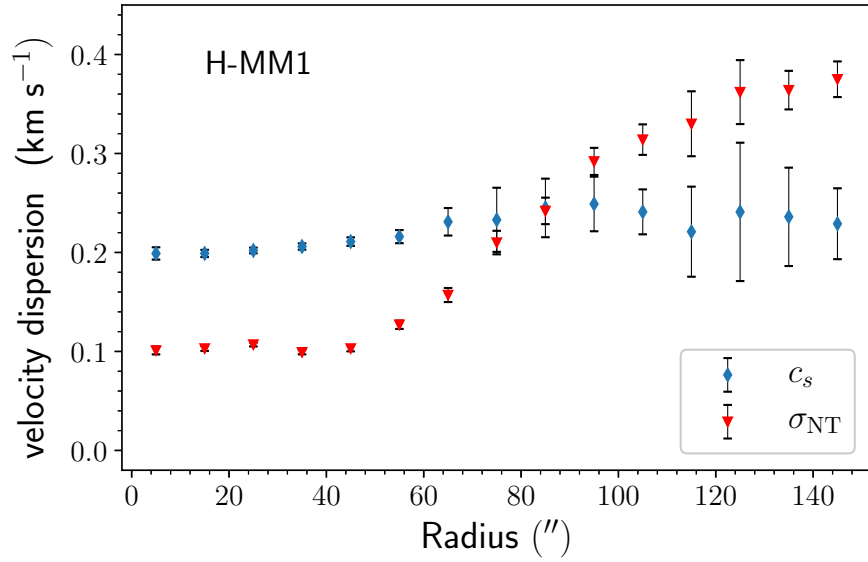


Figure 4.1: Velocity dispersion profiles of the H-MM1 calculated using the  $\text{NH}_3(1,1)$  and  $\text{NH}_3(2,2)$  spectral line cubes from the GAS survey of the L1688 region of Ophiuchus (Friesen et al., 2017). Here  $c_s$  and  $\sigma_{NT}$  are calculated from annularly averaged spectra, by first aligning the spectra in velocity with the help of the  $v_{\text{LSR}}$  map. The transonic radius (where  $c_s = \sigma_{NT}$ ) of H-MM1 can be identified as  $r_0 \approx 86''$  (0.05 pc at the 120 pc distance of Ophiuchus).

averaged thermal and nonthermal velocity dispersions in HMM-1. It shows a clear transition point at radius  $\approx 86''$ , where  $c_s = \sigma_{NT}$ . We identify this radius as the transonic radius,  $r_c$ , and consider it to be the core boundary. The nonthermal velocity dispersion is  $\approx 0.5c_s$  inside the core, and it increases steeply to  $\approx 2c_s$  across the core boundary. We use the same prescription to map the thermal and nonthermal velocity dispersion of other selected cores in L1688. Figure 4.2 shows the annularly averaged thermal and nonthermal velocity dispersions of all the other selected cores in L1688. We have selected only those cores that have a distinct delineation between thermal/nonthermal line-widths ( $c_s = \sigma_{NT}$ ) at a transonic radius  $r_c$  with the nonthermal dispersion becoming subthermal towards the center of the core. Outside the transonic radius for some cores (for example Oph-CN and Oph-Fe) the nonthermal dispersion is comparable to the sound speed. In Table 4.1 we give the measure of the transonic  $r_c$  radius and the corresponding velocity dispersion  $(\sigma_{NT})_c$  at  $r_c$ . The values of  $r_c$  and  $(\sigma_{NT})_c$  are obtained by interpolating the thermal and nonthermal data points and finding their intersection. In this paper, while we

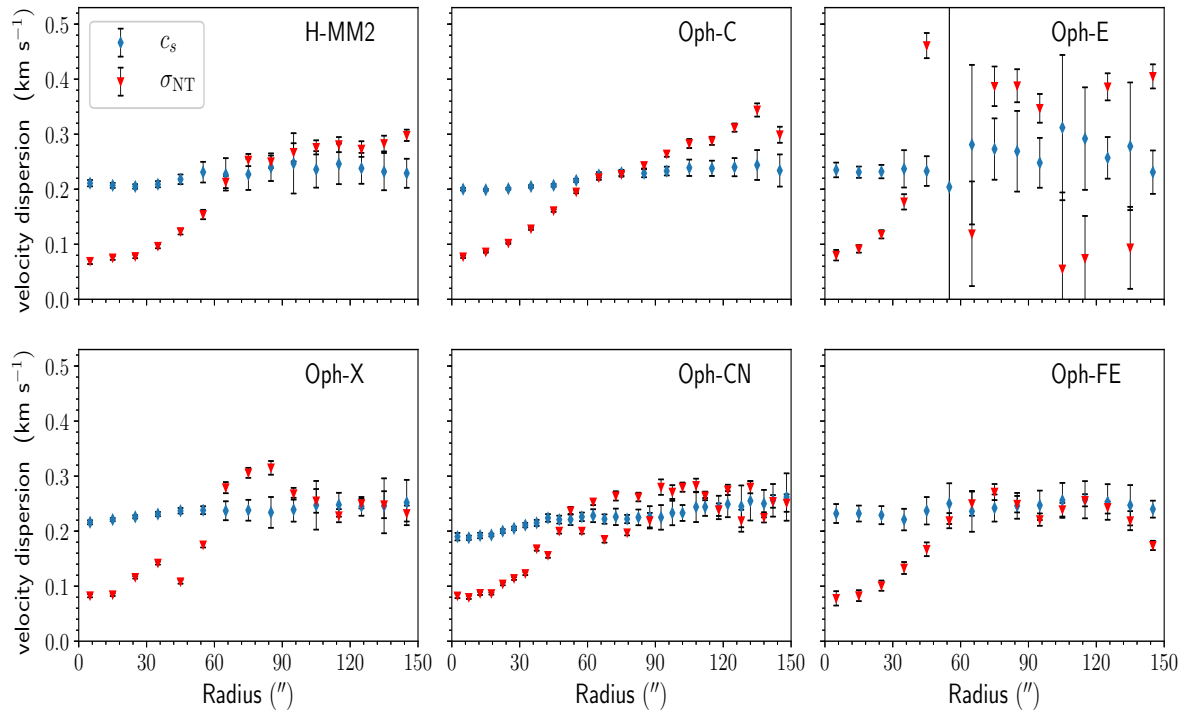


Figure 4.2: Velocity dispersion profiles of some selected cores in Ophiuchus calculated using the  $\text{NH}_3(1, 1)$  and  $\text{NH}_3(2, 2)$  spectral line cubes from the GAS survey of the L1688 region of Ophiuchus (Friesen et al., 2017). Here  $c_s$  and  $\sigma_{\text{NT}}$  are calculated from annularly averaged spectra, by first aligning the spectra in velocity with the help of the  $v_{\text{LSR}}$  map.

present the results from our analysis of seven different cores in L1688, we focus our discussion on H-MM1.

## 4.2.2 Column Density and Density Model

Figure 4.3 shows the circularly averaged  $850 \mu\text{m}$  intensity profiles of seven cores in L1688 derived from the SCUBA-2 maps (see Figure 1 in Pattle et al. (2015)). In order to characterize each observed column density profile, we adopt an idealized Plummer model of a spherical core (Arzoumanian et al., 2011) with radial density

$$\rho(r) = \frac{\rho_0}{\left[1 + (r/r_0^2)\right]^{p/2}}, \quad (4.1)$$

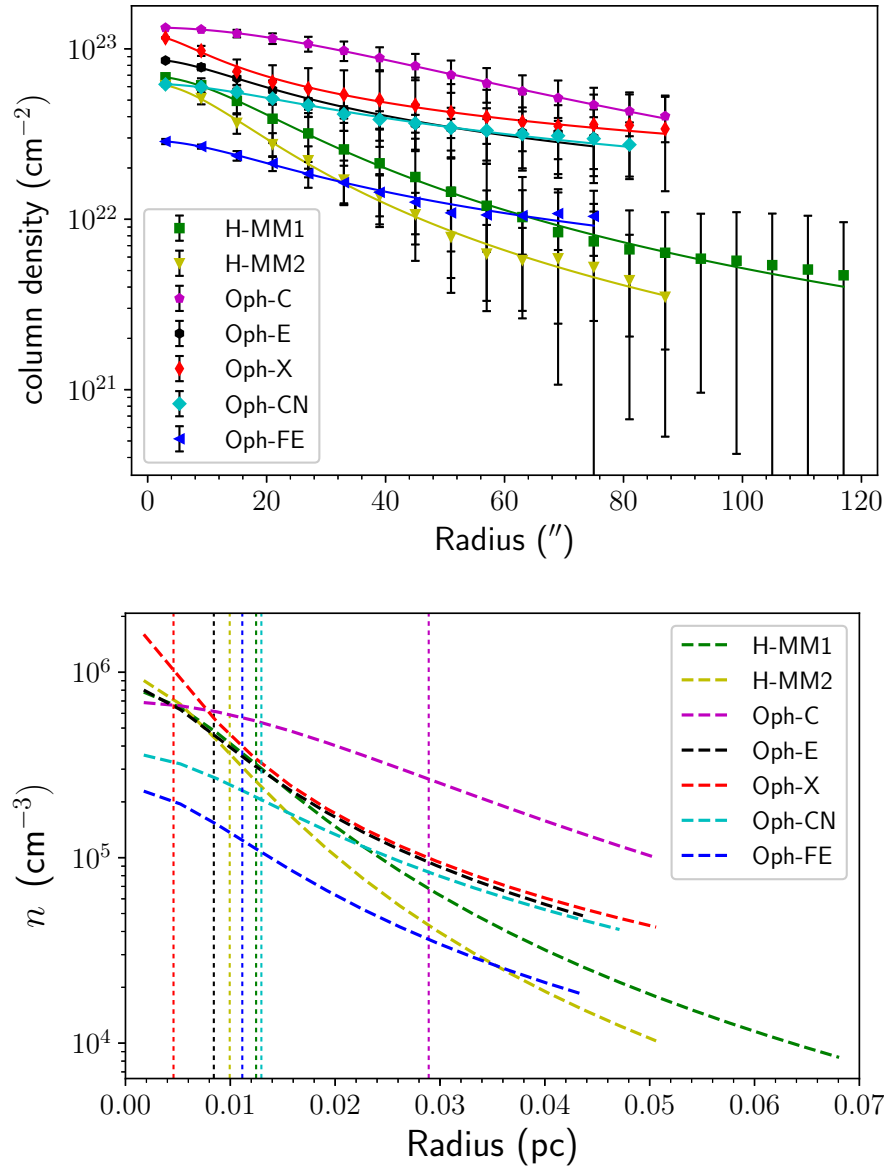


Figure 4.3: Top: Submillimeter intensities as functions of radial distance from the center of cores in Ophiuchus. The colored markers with error bars indicate averages over concentric annuli and their standard deviations. These are obtained from SCUBA-2 maps at  $850 \mu\text{m}$  published by Pattle et al. (2015). The solid curves are fits to the data using the Plummer model Equation (4.1). Bottom: The density profiles as functions of radial distance from the center of cores in L1688. Here we plot  $n(r)$  using the fit parameters (see Table 4.1). The vertical dotted lines mark the extent of the central flat region  $r_0$ .



Table 4.1: The Plummer fit parameters are  $n_0$ ,  $r_0$ , and  $p/2$ ,  $r_c$  is the transonic radius and  $(\sigma_{\text{NT}})_c$  is the velocity dispersion at  $r_c$ . The final column gives an estimate of the mass of each core.

Core	$r_c$ ( $10^{-2}$ pc)	$(\sigma_{\text{NT}})_c$ ( $\text{km s}^{-1}$ )	$n_0$ ( $10^5 \text{ cm}^{-3}$ )	$r_0$ ( $10^{-2}$ pc)	$p/2$	Mass ( $M_\odot$ )
H-MM1	5.0	0.25	$8.0 \pm 3.0$	$1.0 \pm 0.4$	$1.3 \pm 0.2$	$1.7 \pm 0.8$
H-MM2	3.9	0.23	$9.0 \pm 2.0$	$1.0 \pm 0.2$	$1.4 \pm 0.2$	$0.9 \pm 0.3$
Oph-C	4.5	0.23	$7.0 \pm 3.0$	$3.0 \pm 1.0$	$1.4 \pm 0.5$	$5.1 \pm 2.1$
Oph-E	2.2	0.24	$8.0 \pm 3.0$	$0.8 \pm 0.3$	$0.9 \pm 0.1$	$0.6 \pm 0.2$
Oph-X	3.5	0.24	$18.0 \pm 8.0$	$0.5 \pm 0.2$	$0.8 \pm 0.1$	$1.5 \pm 0.7$
Oph-CN	2.9	0.22	$4.0 \pm 1.0$	$1.0 \pm 0.5$	$0.8 \pm 0.1$	$0.7 \pm 0.2$
Oph-FE	3.6	0.23	$2.0 \pm 0.9$	$1.0 \pm 0.4$	$0.9 \pm 0.2$	$0.5 \pm 0.2$

where the parameter  $r_0$  is the characteristic radius of the flat inner region of the density profile,  $\rho_0 = \mu m_{\text{H}} n_0$  is the density at the center of the core and  $p$  is the power-law index. The column density profile for such a sphere of radius  $r$  can be modeled as

$$\Sigma_p(r) = A_p \frac{\rho_0 r_0}{[1 + (r/r_0)^2]^{\frac{p-1}{2}}}, \quad (4.2)$$

where  $\Sigma = \mu m_{\text{H}} N_{\text{H}_2}$  is the observed column density,  $N_{\text{H}_2}$  is the number column density,  $m_{\text{H}}$  and  $\mu = 2.33$  are the mass of hydrogen atom and the mean molecular mass, respectively, and

$$A_p = \frac{1}{\cos i} \int_{-\infty}^{\infty} \frac{du}{(1 + u^2)^{p/2}} \quad (4.3)$$

is a constant. We fit the model profile to the SCUBA-2  $850 \mu\text{m}$  data after they are averaged over concentric circular annuli. For fitting the model to the observational data,  $r_0$ ,  $n_0$  (number density at the center), and  $p$  are treated as free parameters. The left panel in Figure 4.3 is the Plummer fit to the averaged submillimeter intensities of the concentric annuli of selected cores (with clearest delineation between thermal/nonthermal motions) in L1688 region in Ophiuchus. The results from the fit are summarized in Table 4.1. On the right panel of Figure 4.3 we plot the density profile of all the cores (using Equation (4.1)). For most of the cores there is a noticeable central flat region of nearly constant density and then a gradual power-law decrease radially outward. The index  $p/2$  is different for each model and varies in the range

$0.78 < p/2 \leq 1.38$ . An estimate of the mass of each core (which is modeled as a sphere) is also given in Table 4.1. The mass is calculated by integrating the density profile upto the core radius (transcritical radius). We run several iterations where the density fit parameters are drawn randomly from respective normal Gaussian distributions with a standard deviation equal to the error range of each parameter. Additionally, for each core we assume a spread of 10% for the transcritical radius  $r_c$  to incorporate the uncertainty (which on average is  $\approx 10\%$ ) in the thermal and nonthermal linewidths. The obtained mass distribution is skewed. The process is repeated 100 times and the uncertainty is calculated from the mean of  $S / \sqrt{(2 \ln 2)}$ , where  $S$  is the semi-interquartile range, for each distribution.

### 4.3 Model

We introduce our new “Core Field Structure (CFS)” method that characterizes the magnetic field profile of dense cores using the high resolution  $\text{NH}_3$  gas kinematics data from the GBT and the  $850 \mu\text{m}$  intensity profile from the SCUBA-2 map. The theory is motivated on the premise that magnetic field lines are effectively frozen-in to the gas, as can be the case for supercritical core contraction. The field lines are pinched towards the center of the core due to gravitational contraction. Furthermore, Alfvénic fluctuations are assumed to dominate the nonthermal component of the velocity dispersion. In the following subsection; we discuss the details of the theory and provide justifications. We apply it to the seven well known cores of Ophiuchus in order to estimate their magnetic field strength profile. Additionally, our model yields the mean magnetic field fluctuations  $\delta B$  and mass-to-flux ratio profile of each of the observed cores.

### 4.3.1 Core Field Structure

Our first assumption is that the field strength follows a power-law approximation. The magnetic field  $B(r)$  within the core radius  $r_c$  can be written in terms of the observed values as

$$B(r)/B(r_c) = [\rho(r)/\rho(r_c)]^\kappa, \quad (4.4)$$

where  $1/2 \leq \kappa \leq 2/3$  (Crutcher, 2012) is a power-law index. Here  $B(r_c)$  is the field strength at the transcritical radius. The gas density approaches a near uniform value outside  $r_c$ . Thus, we do not extend the power-law approximation beyond the core radius. We assume that the core is in a kind of pressure (thermal, magnetic and /or turbulent) equilibrium with the external medium as in Bonnor-Ebert sphere. Equation (4.4) incorporates various relations obtained from theoretical and numerical models of magnetic cores. Mestel (1966) showed that  $\kappa = 2/3$  in the limit of weak magnetic field and spherical isotropic contraction (which can occur if thermal support nearly balances gravity). Theoretically,  $B \propto \rho^{2/3}$  in Mestel (1966) relates the mean field and the mean density within a given radius. In Equation (4.4) we generalize the idea with the approximation that  $B \propto \rho^{2/3}$  can also be applied for local magnetic field  $B$  and local density  $\rho(r)$  at any particular radius. However, in the limit of gravitational contraction mediated by a strong magnetic field Mouschovias (1976a) showed that  $\kappa$  is closer to  $1/2$ . Both the above models do not include nonlinear turbulence within the core, which is consistent with our observations within the transcritical radius. Finally, we know that even in the limit of very strong magnetic field (subcritical mass-to-flux ratio) models of the ambient molecular cloud (Fiedler & Mouschovias, 1993), ambipolar diffusion leads to the formation of supercritical cores within which  $\kappa = 1/2$ . We are only applying Equation (4.4) within the transcritical radius, within which local self-gravity is presumed to be dominant.

To model the nonthermal motions we assume Alfvénic fluctuations. The Alfvénic fluctuations obey

$$\frac{\sigma_{\text{NT}}}{v_A} = \frac{\delta B}{B}, \quad (4.5)$$

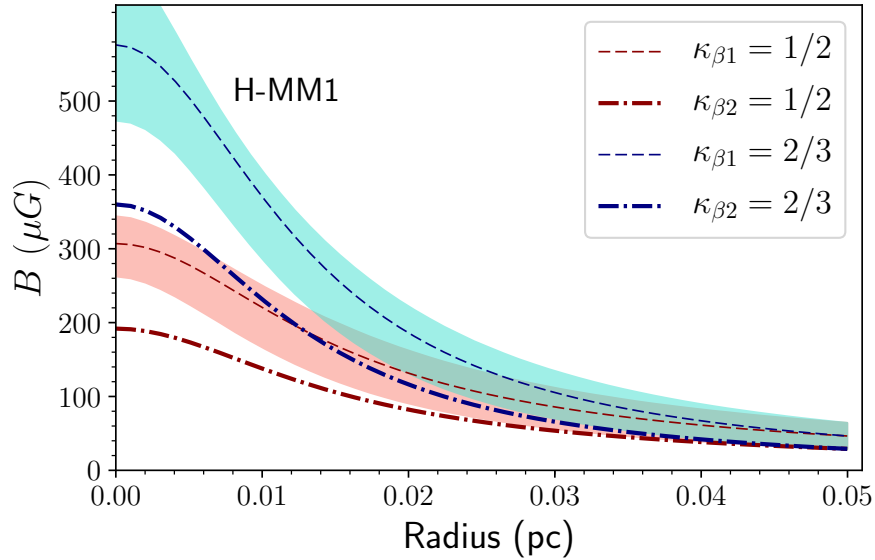


Figure 4.4: The plane-of-sky magnetic field profile of H-MM1 obtained from the CFS method using the observed linewidths and density. The red and the blue dashed lines are the magnetic field  $B$  for  $\kappa = 1/2$  and  $\kappa = 2/3$ , respectively for the choice of  $\beta_1 = 0.5$ . The shaded region encloses the first and the third quartile of the distribution obtained using a Monte Carlo analysis. The dot-dashed red and blue lines are the magnetic field  $B$  for  $\kappa = 1/2$  and  $\kappa = 2/3$ , respectively, for  $\beta_2 = 0.8$ .

where  $v_A \equiv B/(\sqrt{4\pi\rho})$ . This directly leads to

$$\delta B = \sigma_{\text{NT}} \sqrt{4\pi\rho}. \quad (4.6)$$

We also use Equation (4.5) to estimate  $B(r_c)$  for use in Equation (4.4) by estimating a value of relative field fluctuation  $\beta \equiv \delta B/B$  at  $r = r_c$ .

Kudoh & Basu (2003) showed in a model with turbulent driving that  $\beta$  is restricted to  $\lesssim 1$  as highly nonlinear Alfvénic waves quickly steepen and drain energy to shocks and acoustic motions, and that their model cloud evolved to a state in which  $\sigma_{\text{NT}} \approx 0.5v_A$ . Based on the Kudoh & Basu (2003) simulations we pick a range  $0.5 \leq \beta \leq 0.8$  at the inner boundary ( $r = r_c$ ) of the turbulent region. For simplicity we demonstrate only the two limiting values  $\beta_1 = 0.5$  and  $\beta_2 = 0.8$ . The CFS model then gives estimates of the magnetic field profiles (using Equation 4.4) of the dense cores in Ophiuchus. Furthermore, it yields the variation of  $\delta B/B$  and the

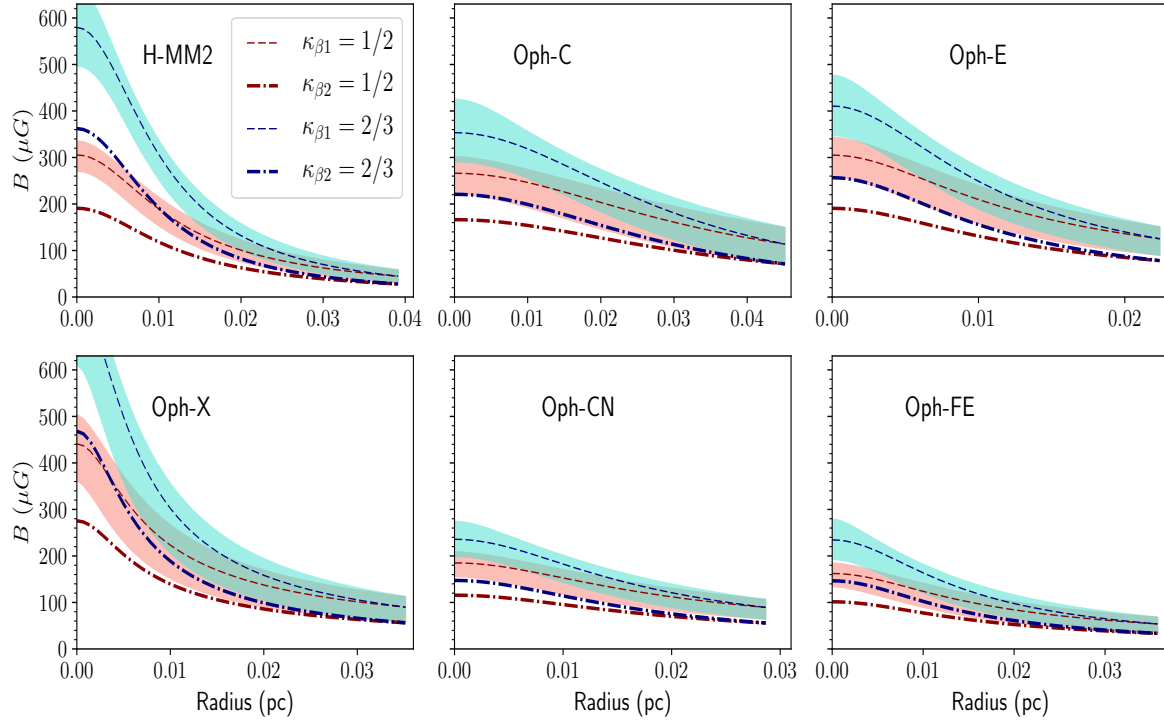


Figure 4.5: The plane-of-sky magnetic field profile of six different cores (names on the upper left corner) obtained from the CFS method using the observed linewidths and density. The red and the blue dashed lines are the magnetic field  $B$  for  $\kappa = 1/2$  and  $\kappa = 2/3$ , respectively, for the choice of  $\beta_1 = 0.5$ . The shaded region encloses the first and the third quartile of the distribution obtained using Monte Carlo analysis. The dot-dashed red and blue lines are the magnetic field  $B$  for  $\kappa = 1/2$  and  $\kappa = 2/3$  respectively, for  $\beta_2 = 0.8$ . The magnetic field increases radially inward and the ascent is steeper for  $\kappa = 2/3$ .

normalized mass-flux ratio within each core profile. We discuss some of the predicted core properties in the next subsection.

### 4.3.2 Core Properties

Figure 4.4 shows the plane-of-sky magnetic field profile of H-MM1 obtained using the CFS method. The magnetic field  $B$  increases radially inward and the ascent is steeper for  $\kappa = 2/3$ . For example, the  $B$  value at  $r = 0.01$  pc for  $\kappa = 2/3$  is  $\simeq 68\%$  greater than that for  $\kappa = 1/2$ . Similarly, we estimate the magnetic field strength profile of all the other cores using the power-law model. Figure 4.5 shows the field profile as a function of radial distance from the center. Similar to H-MM1, the field strength at a radius of 0.01 pc from the center is greater for  $\kappa = 2/3$

compared to  $\kappa = 1/2$ , with a maximum increase of 61% in H-MM2 and a minimum increase of 19% in Oph-E. Furthermore, the general increase of the field strength towards the core center can be associated with the pinching of the field lines due to flux-freezing. The power-law relation  $B \propto \rho^\kappa$  for  $\kappa = 1/2$  or  $2/3$  captures different geometries, for example  $\kappa = 2/3$  is consistent with a spherical core but  $\kappa = 1/2$  is not. Nevertheless, for simplicity we consider cores to be nearly spheres even for  $\kappa = 1/2$ .

We use a Monte Carlo analysis, where we run several iterations to evaluate the magnetic field strength using Equation (4.4). The parameters (for example  $r_0$ ,  $\rho_0$ , and  $p/2$ ) are randomly picked from a Gaussian distribution with standard deviation equal to the error range of each parameter (see Table (4.1)). Additionally, we assume a variation of 10% for the values of  $(\sigma_{\text{NT}})_c$  and  $r_c$  to incorporate the uncertainty (on average  $\approx 10\%$ ) in the thermal and nonthermal linewidths. The shaded region in both the plots encloses the first and the third quartile of the distribution of magnetic field strength. The dotted curve is the actual model value for  $\beta_1 = 0.5$ . We repeat a similar analysis for the six other cores in Ophiuchus. There is a significant dip in the field strength of  $\approx 38\%$  (as indicated by the dot-dashed lines) for a larger assumed value of field fluctuation (i.e.,  $\beta_2 = 0.8$ ) at the transonic radius  $r_c$ . Although there is a systematic dependence of the field strength on the choice of  $\beta$ , the overall shape of the magnetic field profile remains the same.

Figure 4.6 shows the fluctuations of the mean magnetic field  $\delta B$  (Equation (4.6)) and  $\delta B/B$  mapped across the H-MM1 core using the observed nonthermal velocity dispersion data, density, and the modeled magnetic field. The  $\delta B$  measurements are done on a much finer scale (spatially) due to the high resolution  $\text{NH}_3$  map. The inferred variation of  $\delta B/B$  shows a trend very similar to the nonthermal velocity fluctuations. It increases outward as it approaches the transcritical radius. Inside the core  $\delta B/B$  decreases to a relatively constant value of  $\approx 0.1$ . The  $\delta B/B$  profile essentially captures the Alfvénic fluctuations across H-MM1. Figure 4.7 shows  $\delta B$  and  $\delta B/B$  for the other cores in Ophiuchus. They all exhibit a very similar trend as H-MM1. In Figure 4.8 we give estimates of the kinetic, gravitational potential and magnetic energies for

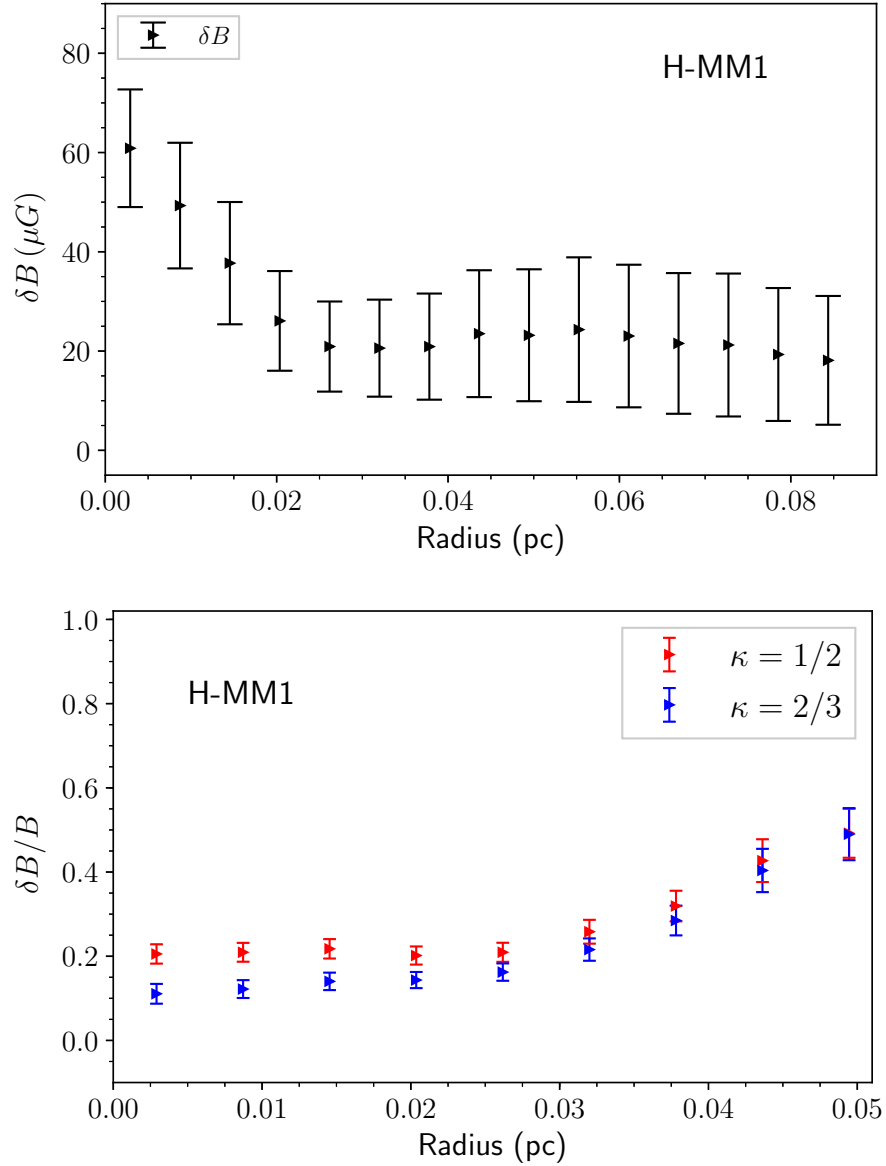


Figure 4.6: Top: The magnetic field fluctuation  $\delta B$  in H-MM1 versus radius. Bottom: The variation of  $\delta B/B$  for  $\kappa = 1/2$  (red) and  $\kappa = 2/3$  (blue), respectively. The error bars in both cases are obtained using standard propagation of one sigma error and Monte Carlo analysis.

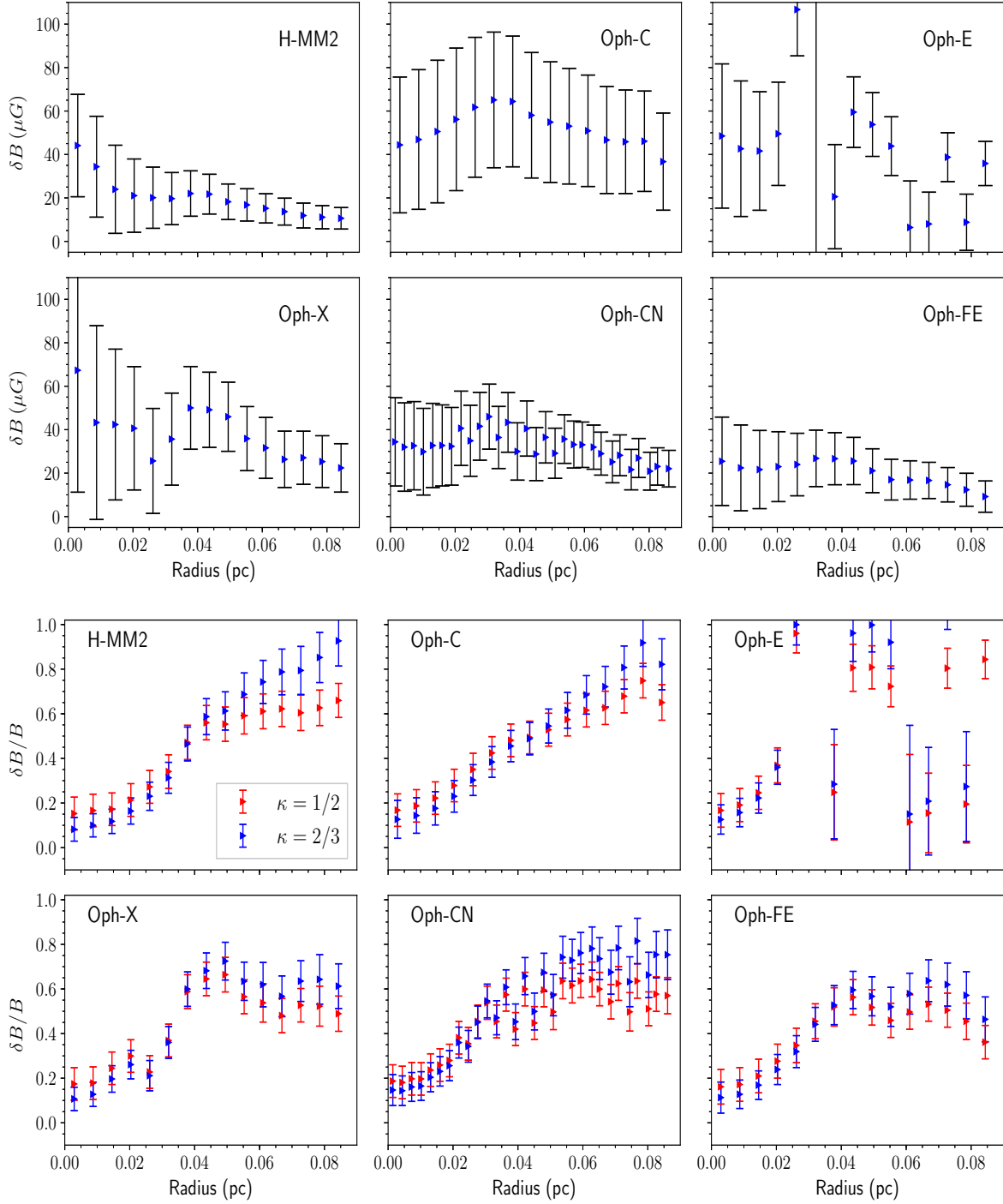


Figure 4.7: Top two panels: The variation of  $\delta B$  across the six cores in Ophiuchus. Bottom two panels: The red and the blue lines show the variation of  $\delta B/B$  for  $\kappa = 1/2$  and  $\kappa = 2/3$ , respectively. The error bars in both the cases are obtained using a standard propagation of one sigma error and Monte Carlo analysis.



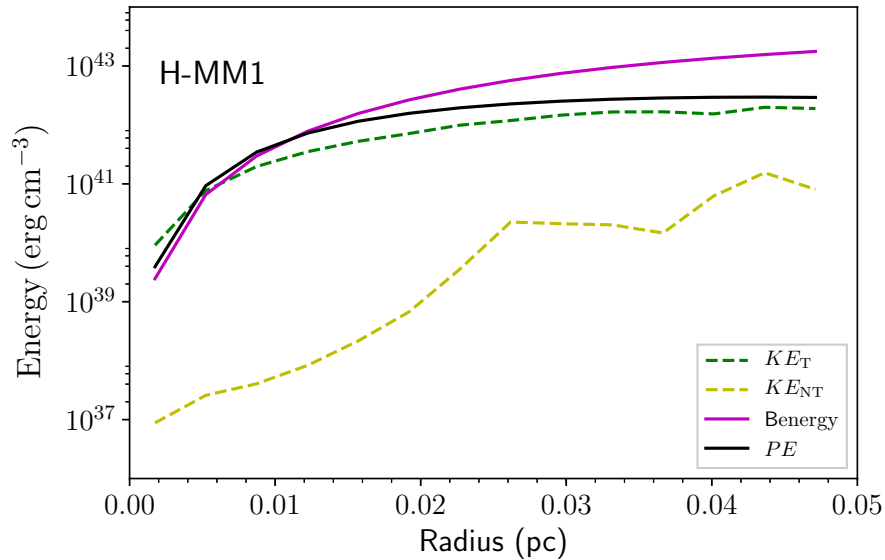


Figure 4.8: The different energy estimates of H-MM1 as a function of radius. For calculating the mass at each radius, the cores are approximated as concentric spheres. The kinetic, potential, and the magnetic energy all have comparable strengths. The magnitude of the nonthermal kinetic energy is much lower, consistent with the low values of non-thermal linewidth inside the core.

H-MM1. The energy magnitudes (except the nonthermal kinetic energy) are comparable all the way from the center to the edge of the core.

### 4.3.3 The mass-to-flux ratio

In this section, we estimate the normalized mass-to-flux ratio  $\mu \equiv M/\Phi/(M/\Phi)_{\text{crit}}$ , where  $(M/\Phi)_{\text{crit}} = (2\pi\sqrt{G})^{-1}$ , of the seven cores studied in this paper, assuming a spherically symmetric density profile. The relative strength of gravity and the magnetic field is measured by the mass-to-flux ratio  $M/\Phi$ . For  $M/\Phi > (M/\Phi)_{\text{crit}}$ , the cloud is supercritical and is prone to collapse. However, for  $M/\Phi < (M/\Phi)_{\text{crit}}$  the cloud is subcritical and cannot collapse as long as magnetic flux freezing applies. Here we consider a simple case where the magnetic field lines are assumed to be vertically threading a spherical dense core in the plane of the sky. We calculate the enclosed mass within cylindrical tubes of constant magnetic field lines as a function of radius from the center in the horizontal midplane of the core. We integrate the volume

density  $\rho(r)$  given in Equation (4.1) with  $p/2 = 1$  along the magnetic field lines to get the corresponding column density as

$$\Sigma(x) = \frac{2r_0^2\rho_0}{\sqrt{(x^2 + r_0^2)}} \arctan\left(\frac{\sqrt{r_c - x^2}}{\sqrt{r_0 + x^2}}\right), \quad (4.7)$$

where  $x$  is the offset from the center in the midplane (see Dapp & Basu (2009) for an analogous calculation). We estimate the mass by integrating the column density from the center to a given radius  $r$  as

$$M(r) = 2\pi \int_0^r x\Sigma(x)dx. \quad (4.8)$$

Inserting Equation (4.7) in Equation (4.8) and integrating, we find

$$M(r) = 4\pi\rho_0r_0^2 \left[ r_c - r_0 \arctan \frac{r_c}{r_0} - \sqrt{r_c^2 - r^2} \right. \\ \left. + \sqrt{r_0^2 - r^2} \arctan\left(\frac{\sqrt{r_c - r^2}}{\sqrt{r_0 + r^2}}\right) \right]. \quad (4.9)$$

The corresponding magnetic flux

$$\Phi(r) = 2\pi \int_0^r B r dr \quad (4.10)$$

is estimated using Equation (4.4) and Equation (4.1) to yield

$$\Phi(r) = 2\pi B_c r_0^2 \left(\frac{n_0}{n_c}\right)^\kappa \left[ \frac{(1 + (r/r_0)^2)^{(1-\kappa)}}{2 - 2\kappa} - \frac{1}{2 - 2\kappa} \right]. \quad (4.11)$$

For the more general case where  $p/2 \neq 1$ , we use numerical integration to estimate the mass and the flux of a given core.

Furthermore, the magnetic field lines are not purely vertical. For a near-flux-frozen con-

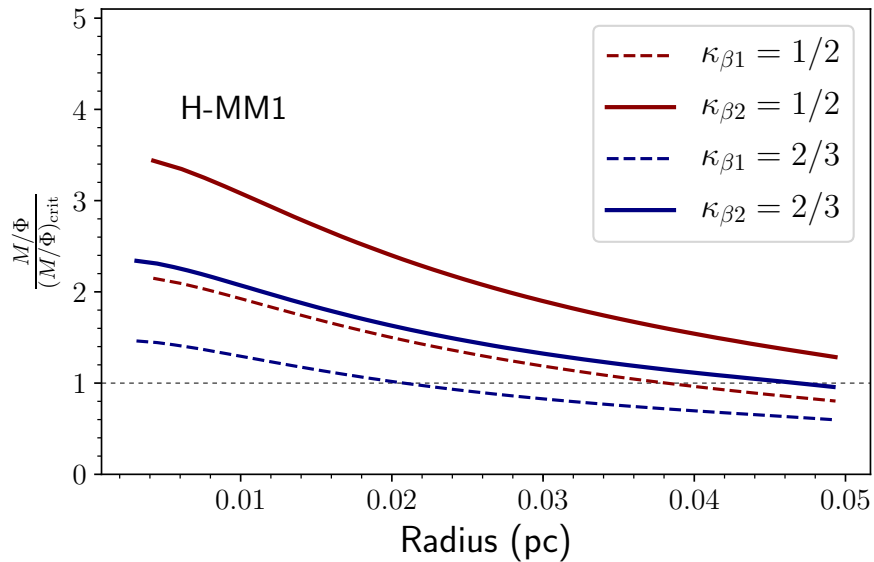


Figure 4.9: The normalized mass-to-flux ratio  $\mu \equiv M/\Phi/(M/\Phi)_{\text{crit}}$  of H-MM1 as a function of radial distance from the center. The dashed and the solid lines are for  $\beta_1 = 0.5$  and  $\beta_2 = 0.8$  respectively. The core is mostly supercritical with  $\mu > 1$  (depending on the value of  $\beta$ ) and is decreasing outward. The dotted horizontal line indicates the critical mass-to-flux ratio.

dition, the field lines are pinched toward the central region of the dense core and resemble an hourglass morphology (Girart et al., 2006; Stephens et al., 2013). We can essentially model such three-dimensional flux lines threading a sphere using the power-law magnetic field model (Myers et al., 2018). Each field line is a contour of constant enclosed flux (see Mouschovias (1976b)). For simplicity, we confine our model to a two-dimensional plane (with  $y = 0$ ). The density profile normalized to  $\rho_c$  gives,

$$\frac{\rho(r)}{\rho_c} = \frac{\rho_0/\rho_c}{[1 + (x/r_0)^2 + (z/r_0)^2]^{p/2}}. \quad (4.12)$$

We further assume that the magnetic field is a power-law of gas density ( $B \propto \rho^\kappa$ ) in both the  $x$ - and  $z$ -directions. In principle, we can estimate the flux  $\Phi$  through a cylinder of infinitesimal thickness in the  $z$ - direction and any radius (say  $\xi = x/r_0$ ) at a particular height above the midplane (using Equations (4.4) and (4.10) as

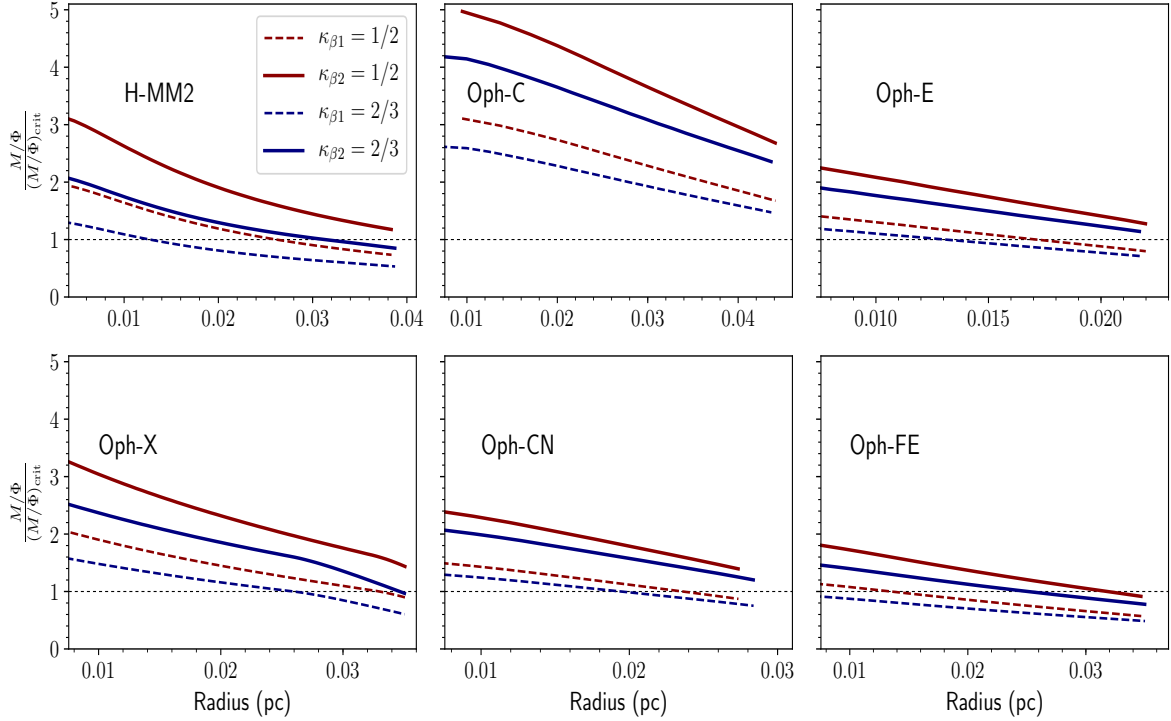


Figure 4.10: The normalized mass-to-flux ratio  $\mu \equiv M/\Phi/(M/\Phi)_{\text{crit}}$  as a function of radial distance from the center for the remaining six cores in our sample. The dashed and the solid lines are for  $\beta_1 = 0.5$  and  $\beta_2 = 0.8$  respectively. The core is mostly supercritical with  $\mu > 1$  (depending on the value of  $\beta$ ) and is decreasing outward. The dotted horizontal line indicates the critical mass-to-flux ratio.

$$\Phi = 2\pi r_0^2 B(r_c) \int_0^\xi \left[ \frac{\rho_0/\rho_c}{[1 + \xi'^2 + (z/r_0)^2]^{p/2}} \right]^k \xi' d\xi'. \quad (4.13)$$

Here we make the approximation that, within each thin segment, the vertical ( $z$ ) component of  $\mathbf{B} = B_x \hat{x} + B_z \hat{z}$ , is equal to the net magnetic field strength  $B$  i.e.,  $B_z \cong B(x, z)$ . This is an improvement over purely vertical field lines (where  $B$  changes only radially in the midplane), as  $B(x, z)$  varies along both  $x - z$  direction. An analytic solution to the above equation is only possible for the case where  $p/2 = 1$ . We solve the above integral numerically and draw contours of constant flux lines. To estimate the enclosed mass through each of the flux tubes within the core (which is assumed to be spherical) we break the tubes into thin disks. The mass

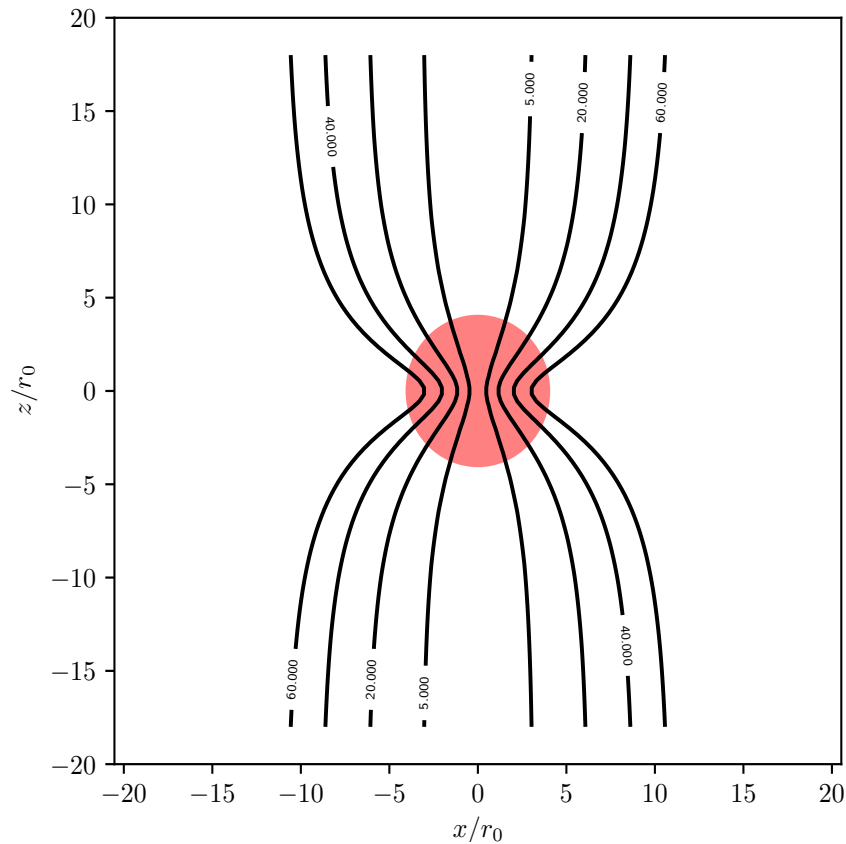


Figure 4.11: An illustration of the magnetic flux contours in H-MM1 for the power-law model with  $\kappa = 2/3$ . The core parameters for H-MM1 ( $n_0$ ,  $r_0$ ,  $r_c$ ) are taken from Table 4.1. The peak density  $\rho_c$  is chosen to be 300 times the background. The marked flux lines are normalized to a background value  $\Phi_0 = 2\pi r_0^2 B_u$  (refer to the text for details). The  $x$ - and  $z$ - axes are in the units of  $r_0 = 0.012$  pc. The circle at the center represents the H-MM1 core of radius  $r_c = 0.05$  pc in the units of  $r_0$ .

of each disk is then added to estimate the total enclosed mass within the tube. Figure 4.9 shows the mass-to-flux ratio of H-MM1 as a function of radial distance from the center. As evident for both  $\kappa = 1/2$  and  $2/3$ , the mass-to-flux ratio ( $\mu$ ) is supercritical at the center and declines towards the core edge. However, the mass-to-flux ratio is quite sensitive to the choice of  $\beta$ . Figure 4.9 shows that for a greater value of  $\beta$  the mass-to-flux estimate increases and the entire core is supercritical. Figure 4.10 shows the profile of the mass-to-flux ratio for the six other cores studied in this paper. Most cores (namely H-MM2, Oph-E, Oph-X and Oph-CN) show a similar decline of the mass-to-flux ratio towards the transcritical radius. Oph-C is supercritical all the way to the core boundary for both the  $\beta$  values. Oph-FE is close to the critical limit.

As an example of the flux tubes we demonstrate the case of H-MM1, where we plot in Figure 4.11 the flux contours for the power-law model with index  $\kappa = 2/3$ . To represent the field lines we introduce a background field strength ( $B_u$ ) and background density  $\rho_u$ . The flux  $\Phi$  is estimated using the Equation (4.10) but with the modified density expression normalized to background density  $\rho_u$ :

$$\frac{\rho(r)}{\rho_u} = 1 + \frac{\rho_0/\rho_u}{[1 + (x/r_0)^2 + (z/r_0)^2]^{p/2}}. \quad (4.14)$$

Here the background density  $\rho_u$  is added to the core density  $\rho(r)$ . The flux lines in Figure 4.11 are normalized to  $\Phi_0 = 2\pi r_0^2 B_u$  for value  $\rho_0/\rho_u = 300$ . It should be noted that the mass-to-flux estimates are not strongly dependent on the background values, which are far less than the density in the vicinity of the transonic radius.

## 4.4 Discussion

We introduce the CFS method, a new technique to estimate the magnetic field strength profile of a dense core. This method is built on a similar premise as the CF method, where the nonthermal velocity fluctuations are assumed to be Alfvénic. The use of  $\delta B/B = \sigma_{NT}/v_A$  is essentially common to both the methods. In the CFS method we measure  $\delta B = \sigma_{NT}(4\pi\rho)^{1/2}$ , unlike the CF method that estimates  $\delta B/B$  using the dispersion ( $\delta\theta$ ) in direction of the polarization vectors. Although similar to the CF technique, the CFS method has a major advantage in that it estimates a field strength profile. The CF method for a core gives only a core-average field strength estimate based on average density, average velocity dispersion and average polarization angle dispersion. We have a much finer scale knowledge of nonthermal velocity dispersion and density, so we can get a much better estimate of field structure in a core based on our choice of  $\delta B/B$  at the transcritical radius. However the CFS method does not model the transition zone where there is a sudden drop of the nonthermal linewidth. The sharp decrease of the linewidth can be a consequence of damping of the Alfvén waves due to reflection or dissipation across

a density gradient (Pinto et al., 2012). Or it could be due to the drop in the ionization fraction at the transcritical radius leading to ambipolar diffusion damping of Alfvén waves. Thus it is possible that the non-ideal MHD effects may become relevant within the core. In the Appendix, we consider the effect of ambipolar diffusion on wave propagation within the core. Equation (B.7) gives a modified version of the Alfvénic theory, which incorporates the correction term (a dimensionless parameter  $\xi = (\tau_{\text{ni}} v_A k)$ ) due to ambipolar diffusion. For conditions appropriate to a dense core, Equation (B.11) shows that  $\xi \ll 1$ . This implies that the use of the flux-freezing relation, Equation 4.5, is approximately valid within the core. Furthermore, even though the Alfvén waves are damped within the core, their wavelengths  $\lambda$  are long enough (i.e.,  $\lambda > \lambda_{\text{cr}} = \pi v_A \tau_{\text{ni}}$ ) that they can propagate and be responsible for the observed nonthermal linewidths.

The primary source of uncertainty in the CFS model is the value of  $\beta$ . As seen previously, the magnetic field strength varies by  $\approx 38\%$  when the value of  $\beta$  changes from 0.5 to 0.8. Although results from turbulent simulations (for example Kudoh & Basu (2003)) do constrain the value of  $\beta$  to be  $< 1$ , there is still a spread in the choice of  $\beta$ . The other possible way is to derive a value for  $\beta$  for each core that have a critical mass-to-flux ratio at the transcritical radius. This will give a  $\beta$  value for all cores close to 0.6, with the distribution having a mean and standard deviation 0.57 and 0.16 respectively. Either ways the core boundary is consistent with the core having an approximately critical mass-to-flux ratio. Another way to think of it is that turbulent and magnetic energy are in equipartition in the envelope while gravitational energy is in equipartition with the magnetic and thermal energy in the core. Nevertheless, value of  $\beta$  although slightly higher is still roughly of the same order of magnitude as  $\beta \equiv \delta\theta = 0.12$  radians measured by Kandori et al. (2017) for the starless core Fest 1-457.

Secondly, modeling the cores as approximate spheres adds to the uncertainties in the magnetic field and the  $M/\Phi$  estimate. Particularly,  $\kappa = 1/2$  in the  $B \propto \rho^\kappa$  relation corresponds to flattening along the field lines. Thus, cores are most likely to resemble a spheroid flattened in the direction of the magnetic field. Furthermore,  $\kappa = 2/3$  (which theoretically models the

weak field case with spherical isotropic collapse) overestimates the field strength inside the core compared to the model with  $\kappa = 1/2$ .

This method introduces a new tool to study the spatial profile of magnetic fields in cores with high resolution  $\text{NH}_3$  line maps. We can possibly generalize the CFS method to study magnetic fields on other well observed  $\text{NH}_3$  cores in Ophiuchus and Taurus using the already published GAS data. Furthermore, the recent paper by Myers et al. (2018) on modeling the magnetic polarization patterns has the potential to predict the polarization observations of dense cores. This will complement the results of the CFS method. A map of the magnetic field strength profile along with the field morphology will serve a great deal in understanding the role of magnetic field in star formation.

## 4.5 Conclusions

The important results from the above study are summarized as follows

- All the observed cores in the L1688 region of the Ophiuchus molecular cloud show a sharp decrease in their nonthermal linewidth as they become subthermal towards the center of the core. Furthermore, in the outer part of H-MM1, H-MM2, Oph-C, and Oph-E there is a substantial increase of  $\sigma_{\text{NT}}$  compared to  $c_s$ .
- The CFS method makes an estimate of  $B(r)$ , the plane-of-sky magnetic field strength as a function of radius. It incorporates spatially resolved observations of the nonthermal velocity dispersion  $\sigma_{\text{NT}}$ , and the gas density measurements in a relatively circular dense core.
- The CFS method yields an estimate of the profile of the magnetic field fluctuations  $\delta B$  and the relative field fluctuation  $\delta B/B$  inside the core.
- We find that the condition  $\delta B/B \leq 1$  at the edge of the core (where  $\sigma_{\text{NT}} = c_s$ ) is consistent with a normalized mass-to-flux ratio  $\mu \gtrsim 1$  inside the core.



- We map the mass-to-flux ratio of cores in Ophiuchus using the CFS method. The mass-to-flux ratio is decreasing radially outward from the center of the core.

## **Acknowledgements**

We thank Sarah Sadavoy, Ian Stephens, Riway Pokhrel, Mike Dunham and Tyler Bourke for fruitful discussions. SB is supported by a Discovery Grant from NSERC.

## Bibliography

- Andersson, B.-G., Lazarian, A., & Vaillancourt, J. E. 2015, *ARA&A*, 53, 501
- André, P., Basu, S., & Inutsuka, S. 2009, *The formation and evolution of prestellar cores*, ed. G. Chabrier (Cambridge University Press), 254
- Arzoumanian, D., André, P., Didelon, P., et al. 2011, *A&A*, 529, L6
- Auddy, S., Basu, S., & Kudoh, T. 2018, *MNRAS*, 474, 400
- Basu, S., Ciolek, G. E., & Wurster, J. 2009, *New A*, 14, 221
- Benson, P. J., & Myers, P. C. 1989, *ApJS*, 71, 89
- Caselli, P., Benson, P. J., Myers, P. C., & Tafalla, M. 2002, *ApJ*, 572, 238
- Chandrasekhar, S., & Fermi, E. 1953, *ApJ*, 118, 113
- Chen, C.-Y., & Ostriker, E. C. 2014, *ApJ*, 785, 69
- Crutcher, R. M. 1999, *ApJ*, 520, 706
- . 2012, *ARA&A*, 50, 29
- Dapp, W. B., & Basu, S. 2009, *MNRAS*, 395, 1092
- Davis, Jr., L., & Greenstein, J. L. 1951, *ApJ*, 114, 206
- Fiedler, R. A., & Mouschovias, T. C. 1993, *ApJ*, 415, 680
- Friesen, R. K., Pineda, J. E., Rosolowsky, E., et al. 2017, *ApJ*, 843, 63
- Gammie, C. F., Lin, Y.-T., Stone, J. M., & Ostriker, E. C. 2003, *ApJ*, 592, 203
- Girart, J. M., Rao, R., & Marrone, D. P. 2006, *Science*, 313, 812
- Goodman, A. A., Barranco, J. A., Wilner, D. J., & Heyer, M. H. 1998, *ApJ*, 504, 223

- Hoang, T., & Lazarian, A. 2008, MNRAS, 388, 117
- Jeans, J. H. 1929, The universe around us.
- Jijina, J., Myers, P. C., & Adams, F. C. 1999, ApJS, 125, 161
- Jørgensen, J. K., Johnstone, D., Kirk, H., et al. 2008, ApJ, 683, 822
- Kandori, R., Tamura, M., Tomisaka, K., et al. 2017, ApJ, 848, 110
- Kirk, J. M., Ward-Thompson, D., & André, P. 2005, MNRAS, 360, 1506
- Klessen, R. S. 2001, ApJ, 556, 837
- Kudoh, T., & Basu, S. 2003, ApJ, 595, 842
- . 2011, ApJ, 728, 123
- . 2014, ApJ, 794, 127
- Lada, C. J., Alves, J. F., & Lombardi, M. 2007, Protostars and Planets V, p.3
- Lada, E. A., Strom, K. M., & Myers, P. C. 1993, in Protostars and Planets III, ed. E. H. Levy & J. I. Lunine, 245
- Larson, R. B. 1985, MNRAS, 214, 379
- . 2003, Reports on Progress in Physics, 66, 1651
- Lazarian, A., & Hoang, T. 2007, MNRAS, 378, 910
- Loren, R. B. 1989, ApJ, 338, 902
- Machaieie, D. A., Vilas-Boas, J. W., Wuensche, C. A., et al. 2017, ApJ, 836, 19
- Marsh, K. A., Kirk, J. M., André, P., et al. 2016, MNRAS, 459, 342
- Mestel, L. 1966, MNRAS, 133, 265

- Mestel, L., & Spitzer, Jr., L. 1956, MNRAS, 116, 503
- Mouschovias, T. C. 1976a, ApJ, 207, 141
- . 1976b, ApJ, 206, 753
- . 1979, ApJ, 228, 475
- Mouschovias, T. C. 1991, in NATO Advanced Science Institutes (ASI) Series C, Vol. 342,  
NATO Advanced Science Institutes (ASI) Series C, ed. C. J. Lada & N. D. Kylafis, 61
- Myers, P. C. 1983, ApJ, 270, 105
- Myers, P. C., Basu, S., & Auddy, S. 2018, ApJ
- Myers, P. C., & Benson, P. J. 1983, ApJ, 266, 309
- Nakamura, F., & Li, Z.-Y. 2005, ApJ, 631, 411
- Padoan, P., & Nordlund, Å. 1999, ApJ, 526, 279
- Padoan, P., Nordlund, A., & Jones, B. J. T. 1997, MNRAS, 288, 145
- Pattle, K., Ward-Thompson, D., Kirk, J. M., et al. 2015, MNRAS, 450, 1094
- Pineda, J. E., Goodman, A. A., Arce, H. G., et al. 2010, ApJ, 712, L116
- Pinto, C., Verdini, A., Galli, D., & Velli, M. 2012, A&A, 544, A66
- Rydbeck, O. E. H., Sume, A., Hjalmarson, A., et al. 1977, ApJ, 215, L35
- Shu, F. H., Adams, F. C., & Lizano, S. 1987, ARA&A, 25, 23
- Stephens, I. W., Looney, L. W., Kwon, W., et al. 2013, ApJ, 769, L15
- Teixeira, P. S., Lada, C. J., & Alves, J. F. 2005, ApJ, 629, 276
- Vazquez-Semadeni, E., Banerjee, R., Gomez, G. C., et al. 2011, MNRAS, 414, 2511

Ward-Thompson, D., Scott, P. F., Hills, R. E., & Andre, P. 1994, MNRAS, 268, 276

Wilking, B. A., Gagné, M., & Allen, L. E. 2008, Star Formation in the  $\rho$  Ophiuchi Molecular Cloud, ed. B. Reipurth, 351

Wilking, B. A., & Lada, C. J. 1983, ApJ, 274, 698

Williams, J. P., Blitz, L., & McKee, C. F. 2000, Protostars and Planets IV, p.97

Wolleben, M., & Reich, W. 2004, A&A, 427, 537

# Chapter 5

## Summary

In this Thesis, we have highlighted the importance of the magnetic field on the star formation process. The fragmentation of molecular clouds is a complex phenomenon (although driven by gravity) and is strongly affected by magnetic fields and turbulence. This Thesis in its entirety has linked the structural and observational signatures to theoretical predictions of magnetically driven star formation models. Some of the important results from the different chapters are compiled in the following section.

### Chapter 2

- The column density PDF of clouds with supercritical mass-to-flux ratio (weak magnetic fields), with either linear perturbations or nonlinear turbulence, quickly develop a power-law tail with slope  $\alpha = -2$ . After the initial compression by the turbulence, gravity dominates the collapse mechanism.
- Clouds with subcritical mass-to-flux (strong magnetic fields) ratio and weak turbulence also proceed directly to a power-law PDF, but with a much steeper index  $\alpha = -4$ . The magnetic support prevents rapid collapse, until gravitationally driven ambipolar diffusion takes over.

- Subcritical clouds (strong magnetic fields) with turbulent initial condition do retain a lognormal shape for a major part of the cloud evolution, and only develop a distinct power-law tail with index  $\alpha = -2$ , when dense cores form due to gravitationally driven ambipolar diffusion.

### Chapter 3

- A natural model of ribbons (or filaments) is based on the interplay between turbulence, strong magnetic fields, and gravitationally driven ambipolar diffusion, rather than pure gravity and thermal pressure.
- A turbulent compression leads to a magnetic ribbon for which the thickness is set by the standoff between ram pressure and the magnetic pressure. Gravitationally driven ambipolar diffusion then leads to runaway collapse of the densest regions in the ribbon, where the mass-to-flux ratio has become supercritical.

### Chapter 4

- The Core Field Structure (CFS) method estimates the plane-of-sky magnetic field strength profile and magnetic field fluctuation (as a function of radius) of dense cores using gas kinematics.
- The sharp decrease of the linewidth can be a consequence of damping of the Alfvén waves due to reflection or dissipation across a density gradient. Or it could be due to the drop in the ionization fraction at the transcritical radius leading to ambipolar diffusion damping of Alfvén waves.
- The results indicate that mass-to-flux ratio in the H-MM1 dense core in L1688 region of the Ophiuchus molecular cloud is decreasing radially outward. We find that the condition  $\delta B/B \leq 1$  at the edge of the core (where  $\sigma_{\text{NT}} = c_s$ ) is consistent with a normalized mass-to-flux ratio  $\mu \gtrsim 1$  inside the core.

Our results provide substantial evidence that indicates that “turbulence-enhanced ambipolar diffusion” could indeed be controlling the star formation process. In this scenario, the gas settles along the field lines to have an overall sheet-like orientation. Subsequently, gravitational instability can lead to fragmentation of clouds with supercritical mass-to-flux ratio. If the cloud is subcritical (magnetically supported), fragmentation can still ensue due to turbulence enhanced gravitationally-driven ambipolar diffusion.

A complete understanding of the role of magnetic fields in the fragmentation of large-scale molecular clouds still requires more observational constraints and comparison with theoretical models. Future work will involve using a much higher resolution computational approaches (for example three-dimensional MHD codes like *Athena*) coupled with multi-wavelength observations (with telescopes like Herschel, SOFIA, and ALMA) to get a three-dimensional picture of the magnetic fields in a star-forming region. These can go a long way in determining how the molecular clouds were formed, in particular, whether the magnetic field is a dominant effect in channeling the gas into the clouds, or whether it is passively swept up by large-scale gas flows. Understanding the connection between the the molecular cloud structure with its formation mechanism is key in explaining the process of star formation. For example a magnetically channelled flow will lead to a sheet like cloud perpendicular to the mean magnetic field. Alternatively, a supernova shell can sweep up a flattened gas cloud with a magnetic field primarily in the plane of the sheet. Future work will involve investigating a much wider range of initial conditions, particularly the magnetic field strength, field orientation, and turbulent flow speed. Modeling the earliest phases will require the ability to simulate subcritical clouds with ambipolar diffusion, since the progenitors of molecular clouds are the interstellar HI clouds that are generally observed to have a subcritical mass-to-flux ratio (Heiles & Troland, 2005). More importantly the relation between magnetic-field strength ( $B$ ) and gas density ( $\rho$ ) for collapsing interstellar clouds and fragments (or cores) is crucial in observationally quantifying the dynamical importance of magnetic fields in the evolution of molecular clouds and star formation. The relative importance of magnetic fields or turbulence will have a signifi-



cant effect on how a prestellar core will collapse. This will require new simulations that can probe stronger magnetic field limits of initial conditions as well the non-ideal MHD effects like ambipolar diffusion.

The theory of star formation has evolved over the last few decades. Our understanding has improved immensely thanks to the emergence of powerful computers and better telescopes. Today we have the power to run “realistic” simulations that can better model the interstellar medium. We have the potential to probe much deeper into space than previously imagined. We are living in exciting times for research in numerical astrophysics. It might soon be possible to have one self-consistent simulation that can explain most observations and give us a complete understanding of the process of star formation

## **Bibliography**

Heiles, C., & Troland, T. H. 2005, *ApJ*, 624, 773

# Appendix A

## Analytic Model of the PDF

Molecular clouds contain many cores that can be approximately described as isothermal spheres. There are several analytic column density profiles to fit prestellar cores. One model to fit such cores is the Bonnor-Ebert sphere (Ebert, 1955; Bonnor, 1956). This model assumes isothermal gas spheres bounded by external pressure and a hydrostatic equilibrium of gravity and thermal pressure. Dapp & Basu (2009) proposed a new three-parameter analytic formula to fit the column density profiles of prestellar cores. This model does not assume the cloud to be in equilibrium and can fit the dynamical states of the nonequilibrium collapse solutions (Larson, 1969) as well. Fischera (2014) discusses the PDF of the mass surface density of molecular clouds. The column density PDF of the molecular clouds show two distinct features, involving a broad distribution around the peak and a power-law tail at the high end. The first aspect can be attributed to the turbulence of the cloud, while the tail develops because of the gravitationally condensed structures. These condensed structures are modelled as spheres or cylinders with a truncated radial density. Fischera (2014) provided an analytic model of the PDF of the condensed structures, by either considering them as spheres or cylinders with a truncated radial profile. He concluded that the asymptotic behaviour of the logarithmic PDF ( $\Sigma P(\Sigma)$ ) in the limit of high column density has a power-law index  $\alpha = (p + 1)/(p - 1)$  for spheres or  $\alpha = p/(p - 1) - 1$  for cylinders, where  $p$  is the power-law index of the column density profile

of the condensed structures.

For clouds with a preferred direction of magnetic field the cloud is flattened along the direction of the magnetic field and settles in to a hydrostatic equilibrium (Dapp & Basu, 2009). In our simulation, the magnetic field is oriented along the  $z$ -axis, resulting in a collapsing core resembling a disk as it is flattened along the magnetic field.

## A.1 Disk Geometry

The generic face-on column density profile for disk shaped flattened core is

$$\Sigma(r) = \frac{\Sigma_c}{\sqrt{(1+(r/a)^p)}} \quad r \leq R, \quad (\text{A.1})$$

$$= 0, \quad r > R, \quad (\text{A.2})$$

where  $p$  is the power-law index for the column density profile. The gravitational contraction of the cores lead to the formation of supercritical pockets of near uniform column density regions surrounded by a power-law profile. The index  $p$  achieves the value 2 just outside the uniform region  $a$ , but transitions to  $\sim 1.5$  at the boundary of the supercritical cores (Basu & Mouschovias, 1995; Basu, 1997). Assuming vertical hydrostatic equilibrium, the volume density is proportional to the square of the column density (Spitzer, 1942) so that

$$c_s^2 \rho = \frac{\pi}{2} G \Sigma^2, \quad (\text{A.3})$$

and the corresponding density is given as

$$\rho(r) = \frac{\pi G}{2c_s^2} \frac{\Sigma_c^2}{1 + (r/a)^p}. \quad (\text{A.4})$$

One can model the molecular cloud as an ensemble of condensed disks. The column density PDF is then

$$P(\Sigma) = \frac{dN'}{d\Sigma} = -P(r) \left( \frac{d\Sigma}{dr} \right)^{-1}, \quad (\text{A.5})$$

where  $dN' = dN/N_{\text{total}}$ . Let  $r/a$  be the normalized impact radius where  $a = kc_s/(\sqrt{G\rho_c})$  is the size of the flat region.  $P(r)dr$  is the probability to measure the column density at a impact radius of  $r$ . Using equation A.1 we get

$$\frac{d\Sigma}{dr} = -\frac{\Sigma_c p (r/a)^{p-1}}{2a (1 + (r/a)^p)^{3/2}}. \quad (\text{A.6})$$

On substituting Equation A.6 in Equation A.5 and using  $P(r) = 2\pi r/(\pi R^2)$  we establish the PDF as

$$P(\Sigma) = \frac{4}{c^2 \Sigma_c p} \left[ \left( \frac{\Sigma_c}{\Sigma} \right)^2 - 1 \right]^{(2/p-1)} \left( \frac{\Sigma_c}{\Sigma} \right)^3. \quad (\text{A.7})$$

The power-law index for the column density profile (Equation A.1)  $p = 2$  and  $p = 1$  corresponds to just outside the uniform region and the boundary of the supercritical core respectively. Depending on the region of interest we can estimate the power-law index the column density PDF (using Equation A.7). For  $p = 2$  we get

$$P(\Sigma)_{p=2} = \frac{2 \Sigma_c^2}{c^2 \Sigma^3}. \quad (\text{A.8})$$

In the regions just outside the uniform region,  $P(\Sigma) \propto \Sigma^{-3}$ . For  $p = 1$  we find the column density PDF as

$$P(\Sigma)_{p=1} = \frac{4 \Sigma_c^2 (\Sigma_c^2 - \Sigma^2)}{c^2 \Sigma^5}. \quad (\text{A.9})$$

For  $\Sigma \ll \Sigma_c$ , i.e. corresponding to region well outside the center and closer to the core boundary,  $P(\Sigma) \propto \Sigma^{-5}$ .

## **Bibliography**

Basu, S. 1997, *ApJ*, 485, 240

Basu, S., & Mouschovias, T. C. 1995, *ApJ*, 453, 271

Bonnor, W. B. 1956, *MNRAS*, 116, 351

Dapp, W. B., & Basu, S. 2009, *MNRAS*, 395, 1092

Ebert, R. 1955, *ZAp*, 37, 217

Fischera, J. 2014, *A&A*, 565, A24

Larson, R. B. 1969, *MNRAS*, 145, 271

Spitzer, Jr., L. 1942, *ApJ*, 95, 329

# Appendix B

## Modified Alfvénic theory

### B.1 Dispersion relation

The dispersion relation of Alfvén waves in a partially ionized medium (Pinto et al., 2012) in the long wavelength limit is

$$\omega^2 - k^2 v_A^2 + i\eta_{AD} k^2 \omega = 0. \quad (\text{B.1})$$

Here  $\eta_{AD} = v_A^2 \tau_{ni}$  is the ambipolar diffusion resistivity and  $\tau_{ni} = (\gamma_{ni} \rho_i)^{-1}$  is the mean neutral-ion collision time in terms of the drag coefficient

$$\gamma_{ni} = \frac{\langle \sigma w \rangle_{in}}{1.4 (m_n + m_i)}, \quad (\text{B.2})$$

(Basu & Mouschovias, 1994) and the ion density  $\rho_i$ . In the above equation  $\langle \sigma w \rangle_{in}$  is the average collision rate between the ions of mass  $m_i$  and neutrals of mass  $m_n$ . On rearranging, Equation (B.1) is rewritten as

$$k^2 = \frac{\omega^2}{v_A^2} \left[ \frac{1}{1 + i\tau_{ni}\omega} \right]. \quad (\text{B.3})$$

In the limit  $\tau_{\text{ni}}\omega < 1$ , Equation (B.3) on binomial expansion yields

$$k = \frac{\omega}{v_A} \left(1 - i \frac{1}{2} \tau_{\text{ni}} \omega\right). \quad (\text{B.4})$$

Defining  $\xi = (1/2)\tau_{\text{ni}}\omega$  as a dimensionless parameter, we can represent Equation (B.4) in terms of a magnitude and a phase  $\theta$ :

$$\left| \frac{k}{\omega} \right| = \frac{1}{v_A} \sqrt{1 + \xi^2} |e^{i\theta}|. \quad (\text{B.5})$$

Using Equation (B.4) to replace  $k$  in Equation (17) from Pinto et al. (2012), we derive the relation between the amplitude of fluctuations of the neutral velocity  $u_{\text{n0}}$  to the fluctuation of the magnetic field  $\delta B$ . In the long wavelength limit we get

$$|u_{\text{n0}}| = v_A \frac{|\delta B|}{B} \sqrt{1 + \xi^2}. \quad (\text{B.6})$$

If  $\xi \ll 1$ , then

$$|u_{\text{n0}}| \simeq v_A \frac{|\delta B|}{B} \left[ 1 + \frac{1}{2} \xi^2 \right]. \quad (\text{B.7})$$

This gives a modified version for the Alfvénic theory, which incorporates the correction term due to ambipolar diffusion. Equation (B.7) is equivalent to Equation (??), if we equate  $\sigma_{\text{NT}} = |u_{\text{n0}}|$  and take the limit  $\xi \rightarrow 0$ . Again assuming that  $\xi \ll 1$  (which we will later verify), we apply the standard dispersion relation of ideal Alfvén waves,  $\omega = v_A k$ , and express  $\xi$  in terms of wavenumber  $k$ ;

$$\xi^2 = \left( \frac{\tau_{\text{ni}} v_A k}{2} \right)^2. \quad (\text{B.8})$$

Using Equation (B.2) to replace  $\tau_{\text{ni}}$  in terms of the drag coefficient  $\gamma_{\text{ni}}$  and ion density, we get

$$\xi^2 = \frac{1}{4} \frac{B^2}{4\pi\rho_{\text{n}}} k^2 \left[ 1.4 \frac{m_i + m_n}{\rho_i \langle \sigma w \rangle_{\text{in}}} \right]^2. \quad (\text{B.9})$$



We can estimate the above quantities in Equation (B.8) by specifying appropriate values relevant for dense cores embedded in molecular clouds. For example, if  $B \simeq 30 \mu\text{G}$  and  $\rho_n = m_n n_0$ , where  $n_0 = 10^4 \text{ cm}^{-3}$  is the number density of neutrals and  $m_n = 2.33 \times 1.67 \times 10^{-24} \text{ g}$ , the Alfvén speed  $v_A = 0.4 \text{ km s}^{-1}$ . Furthermore, for  $\langle \sigma w \rangle_{\text{in}} = 1.69 \times 10^{-9} \text{ cm}^{-3} \text{ s}^{-1}$  and  $m_i = 29 \times 1.67 \times 10^{-24} \text{ g}$ , the drag coefficient  $\gamma_{\text{ni}} = 2.3 \times 10^{13} \text{ cm}^3 \text{ g}^{-1} \text{ s}^{-1}$ . The ion density  $\rho_i$  is again determined by the approximate relation

$$\rho_i = m_i K n_0^{1/2} = 1.45 \times 10^{-23} \text{ g cm}^{-3}, \quad (\text{B.10})$$

where  $K = 3 \times 10^{-3} \text{ cm}^{-3}$ . This gives  $\tau_{\text{ni}} = (\gamma_{\text{ni}} \rho_i)^{-1} = 3 \times 10^9 \text{ s}$ . The wavenumber  $k = (2\pi)/\lambda$  of interest will roughly correspond to a wavelength  $\lambda \simeq 0.1 \text{ pc}$  i.e., about equal to the core diameter. This yields

$$\xi = 1.3 \times 10^{-3} \left( \frac{v_A}{0.4 \text{ km s}^{-1}} \right) \left( \frac{\tau_{\text{ni}}}{3 \times 10^9 \text{ s}} \right) \left( \frac{0.1 \text{ pc}}{\lambda} \right), \quad (\text{B.11})$$

such that  $\xi \ll 1$  in a dense core. This is equivalent to the waves having wavelength  $\lambda \gg \lambda_{\text{cr}}$ , where  $\lambda_{\text{cr}} = \pi v_A \tau_{\text{ni}}$ , (see Eq. (15) in Pinto et al. (2012)) is the critical wavelength for wave propagation, i.e., wavelengths shorter than this are critically damped. Thus, the Alfvén waves can still propagate within the core and be responsible for the observed nonthermal linewidths. The condition  $\xi \ll 1$  continues to apply for wavelengths  $\lambda$  significantly smaller than 0.1 pc, as can be seen from Equation (B.11)

**Bibliography**

Basu, S., & Mouschovias, T. C. 1994, ApJ, 432, 720

Pinto, C., Verdini, A., Galli, D., & Velli, M. 2012, A&A, 544, A66

# Curriculum Vitae

## **Sayantana Auddy**

Department of Physics and Astronomy  
1151 Richmond Street  
London, Ontario, Canada  
N6A 3K7

## **Education**

- PhD Candidate, University of Western Ontario, 2014 - current  
Adviser: Prof Shantanu Basu
- Visiting Student Fellow, HarvardSmithsonian Center for Astrophysics, May - Nov, 2017  
Adviser: Dr Philip Myers
- MSc Astronomy, University of Western Ontario, September 2014  
Thesis Topic: A Study of Substellar Mass Limit for Brown Dwarfs : Adviser: Prof Shantanu Basu
- MSc Physics, Indian Institute of Technology (Madras, India), April 2013  
Thesis: Inflation and Cosmological Perturbation Theory : Adviser: Prof L Sriramkumar

## **Talks**

- “The effect of magnetic fields and ambipolar diffusion on the column density PDFs in molecular clouds”. Contributed talk at the Magnetic Field vs Turbulence conference, Taiwan, February 2018
- “The role of magnetic fields on the column density PDFs in molecular clouds”. Talk at the Star Formation Lunch, CEA SACLAY Paris, France, January 2018
- “The role of strong magnetic fields in molecular clouds” and star formation. Talk at the Max Planck Institute for Extraterrestrial Physics, Germany, January 2018
- “The effect of magnetic fields on the column density probability Distribution function in molecular clouds”, at CITA, University of Toronto, Canada, November 2017

- “Column Density PDFs of Molecular Clouds”. Talk at the Star Formation Journal Club at Centre for Astrophysics, Harvard, Cambridge, United States, October 2017
- “A Magnetic Ribbon Model for Star forming Filaments”. Contributed talk at Winter School on Astronomy, Hyderabad, India, February 2017.
- “Analytic Model for The Substellar Mass Limit and Brown Dwarf evolution”. Contributed talk at Astronomy At Taj, Agra, India, February 2016.
- “Evolution of Brown Dwarf” Invited talk at the CPSX research forum at Western, London, Canada, November 2014.
- “Analytic derivation of sub-stellar mass limit for non-zero degeneracy parameter.” Contributed talk at Canadian Association of Physicists, Sudbury, Canada, June 2014.
- “Cosmic Topology”. Contributed Talk at IUCAA Summer School in Astronomy and Astrophysics, Pune, India, June 2012.

## Publications

### *1st Authored Publications*

- (1) Magnetic Field Structure of Dense Cores using Spectroscopic Methods; **Sayantana Auddy**, Philip Myers, Shantanu Basu, et al. submitted in June **2018**
- (2) The Effect of Magnetic Fields and Ambipolar Diffusion on the Column Density Probability Distribution Function in Molecular Clouds; **Sayantana Auddy**, Shantanu Basu, Takahiro Kudoh, **2017**, MNRAS 474-400 (arXiv:1710.05427)
- (3) A Magnetic Ribbon Model for Star Forming Filaments; **Sayantana Auddy**, Shantanu Basu, Takahiro Kudo, **2016**, ApJ 831:46 (6pp). (arXiv:1609.02989)
- (4) Analytic Models of Brown Dwarfs and Substellar Mass Limit; **Sayantana Auddy**, Shantanu Basu and S.R. Valluri, **2016**, Advances in Astronomy, Volume 2016 (2016), Article ID 5743272, 15 pages. (arXiv:1607.04338)

### *Invited Review (refereed)*

- (5) From Molecular Clouds to the IMF: Spatial and Temporal Effects; Shantanu Basu, **Sayantana Auddy**, **2017**, Memorie della Societa Astronomica Italiana (in press) arXiv: 1710.06361

### *Coauthored refereed publications*

- (6) The MLP Distribution: A Modified Lognormal Power-Law Model for the Stellar Initial Mass Function; Shantanu Basu, M. Gil and **Sayantana Auddy**, **2015**, MNRAS 449(3) : 2413-2420

- (7) Vacuum Birefringence, the Photon Anomalous Magnetic Moment and the Neutron Star RX J1856.5-3754; S. R. Valluri, J. W. Mielniczuk, F. Chishtie, D. Lamm, **Sayantana Auddy**, **2017**, MNRAS 472-2398
- (8) Gravitational Wave Background in the Quasi-Steady State Cosmology; J V Narlikar, Sanjeev Dhurandhar, R. G. Vishwakarma, S. R. Valluri, **Sayantana Auddy**, **2015**, MNRAS, 451 : 1390-1395
- (9) “Magnetic Polarization Patterns”; Philip Myers, Shantanu Basu, and **Sayantana Auddy**, submitted in June **2018**

*Conference Proceeding(refereed)*

- (10) Magnetic Ribbons: A Minimum Hypothesis Model for Filaments; **Sayantana Auddy**, Shantanu Basu, Takahiro Kudo, **2017**, to appear in proceedings of SFDE conference, eds. D. Johnstone, T. Hoang, F. Nakamura, Q. Nguyen Luong, and J. Tran Thanh Van.

*Link to ADS:*

[ui.adsabs.harvard.edu/#/public-libraries/rAPk8x0TTjaXOHKLMYtvvw](https://ui.adsabs.harvard.edu/#/public-libraries/rAPk8x0TTjaXOHKLMYtvvw)